Ph. D. DISSERTATION

ORGANIC/METAL INTERFACES FOR HIGH PERFORMANCE ORGANIC DIODES

고성능 유기 다이오드를 위한 유기물/금속 계면 연구

BY

CHAN-MO KANG

FEBRUARY 2014

DEPARTMENT OF ELECTRICAL ENGINEERING AND
COMPUTUER SCIENCE
COLLEGE OF ENGINEERING
SEOUL NATIONAL UNIVERSITY

ORGANIC/METAL INTERFACES FOR HIGH PERFORMANCE ORGANIC DIODES

고성능 유기 다이오드를 위한 유기물/금속 계면 연구

지도교수 이 창 희

이 논문을 공학박사 학위논문으로 제출함

2014 년 2 월

서울대학교 대학원

전기컴퓨터공학부

강 찬 모

강찬모의 박사 학위논문을 인준함

2014 년 2 월

위 원 장 : _____ (인)

부위원장 : _____ (인)

위 원 : _____ (인)

위 원 : _____ (인)

위 원 : _____ (인)

Abstract

ORGANIC/METAL INTERFACES FOR HIGH PERFORMANCE ORGANIC DIODES

CHAN-MO KANG

DEPARTMENT OF ELECTRICAL ENGINEERING AND COMPUTER SCIENCE

COLLEGE OF ENGINEERING

SEOUL NATIONAL UNIVERSITY

Organic electronics have received a great attention for next generation electronics due to lots of advantages such as easy patterning, flexibility, light-weight, and potential of large-area application. In spite of such a lot of advantages, however, there are still many issues that need to be improved such as charge injection, mobility, lifetime, operational stability, reliability, and uniformity. One of the important issues to make high performance diode is to improve charge injection efficiency. In this thesis, we investigate organic/metal interface of the diode to enhance charge injection efficiency and demonstrate high performance organic diodes. Two major methods are used to improve device performance: improved

charge injection by electrical annealing and reduced hole injection barrier by using permanent dipole moment of self-assembled monolayer (SAM).

First, we investigate the effect of electrical annealing on pentacene diode to which electrical annealing has not been applied because it cannot have ionic species. By using molybdenum trioxide (MoO_3) instead of ionic species, electrical annealing can be applied to thermally deposited device which is advantageous for fabricating high performance devices. After electrical annealing, The turn-on voltage is reduced from approximately 1.3 V to 0.2 V and current at 3 V is increased from approximately 0.2 mA to 1 mA without increase of the reverse-bias current. In addition to MoO_3 as a hole injection layer, 1,4,5,8,9,11-hexaazatriphenylene-hexacarbonitrile (HAT-CN) and copper hexadecafluorophthalocyanine (F_{16}CuPc), which have deep highest occupied molecular orbital (HOMO) levels, show electrical annealing effect but poly(3,4-ethylene-dioxythiophene):poly(styrenesulfonate) (PEDOT:PSS), 4,4',4''-tris(N-3-methylphenylamino)triphenylamin (m-MTDATA), and copper phthalocyanine (CuPc) do not affect electrical annealing. the cutoff frequency was increased from 10.5 MHz to 85.7 MHz. There is no improvement of current or reduction of turn-on voltage by using thermal annealing only, indicating that electric field plays an important role for electrical annealing. From the time of flight secondary ion mass spectrometry (ToF-SIMS) and impedance spectra, we conclude that the device performance of the pentacene diode is improved by electrical annealing due to the creation of the pentacene:MoO_3 mixed layer. The mixed layer effectively increases charge injection by reducing small potential barrier which causes the turn-on voltage of current–voltage (*I–V*) characteristics and the RC-component at Au/MoO_3/pentacene interface of impedance spectra. Note that because this uniform and thin pentacene:MoO_3 mixed layer cannot be formed by thermal evaporation, electrical annealing is the best technique to form the uniform,

thin, and gradual pentacene:MoO_3 mixed layer for improving device performance. After electrical annealing, Al penetration into the pentacene layer was also observed. Because Al was deposited on the polycrystalline pentacene, Al spikes are formed at the pentacene grain boundary. These Al spikes can induce a higher electric field, facilitating the penetration of Al. Therefore, the penetrated Al may create rod-like structures that can be modeled as constant phase element (CPE).

Second, we investigated the structure–property relationship of pentacene on gold and SAM-treated gold along the vertical direction. From the photoelectron spectrometer, the work function of gold, thiophenol (TP)-modified gold and pentafluorobenzenethiol (PFBT)-modified gold is measured to be 4.78, 4.67, and 5.02 eV, respectively. PFBT-treated gold effectively lower the injection barrier between the anode and the active layer, the forward-bias current density of the diode with PFBT-treated gold is much higher than that with pristine gold and finally current density of 100 A/cm^2 is obtained at 3 V. In addition, the rectification ratio of the diode is founded to be 7.47 × 10^5 at 1 V, and 1.05 × 10^7 at 2.8 V. The 3-dB frequency, in terms of voltage, of the rectifier which is composed of the diode and a capacitor is obtained to be 1.24 GHz. Finally, V_{out} of 3.8 V at 1 GHz is obtained when input voltage of 10 V is applied. From the X-ray diffraction (XRD), atomic force microscope (AFM), and Raman analysis, pentacene molecules on gold exhibit lying-down orientation and those on PFBT-treated gold exhibit standing-up orientation. These structure differences change the electrical property. The mobility, calculated by space charge limited current (SCLC), of the pentacene film on gold and PFBT-treated gold is measured to be 6.82 × 10^{-4} and 0.114 $cm^2V^{-1}s^{-1}$, respectively. The XRD patterns and vertical scanning electron microscope (SEM) images show that pentacene on gold exhibits the entangled and disordered structure whereas pentacene on PFBT-treated gold exhibits dense and ordered structure. This

poor molecular ordering for pentacene on gold can limit charge transport property, resulting that the mobility of the pentacene film on gold is smaller than that of on PFBT-treated gold.

Keywords: Organic diodes, Organic rectifiers, Electrical annealing, Self-assembled monolayer, Pentacene, RFID, flexible electronics.

Student Number: 2008-20815

Contents

List of Figures

List of Tables

Chapter 1

Introduction

During the past decades, organic electronics have received a great attention for next generation electronics.[1-3] Organic materials have lots of advantage such as easy patterning, flexibility, light-weight, and potential of large-area application. In addition, organic materials are easy to tune their functionality by modifying the molecular design and chemical composition. Moreover, the original property of their flexibility will create new applications which would be impossible using conventional silicon-based inorganic technology. Over the last few decades, remarkable progress has been achieved and some applications have been commercialized. For example, organic light-emitting diodes (OLEDs) have already been utilized in mobile phones, digital cameras, and even in 55-inch full-color TVs as shown in Figure 1.1. In addition, the flexible full-color OLEDs which cannot be make using conventional liquid-crystal displays (LCDs) will also be commercialized soon. Another example is organic photovoltaic cells (OPVs). Recently Kolon

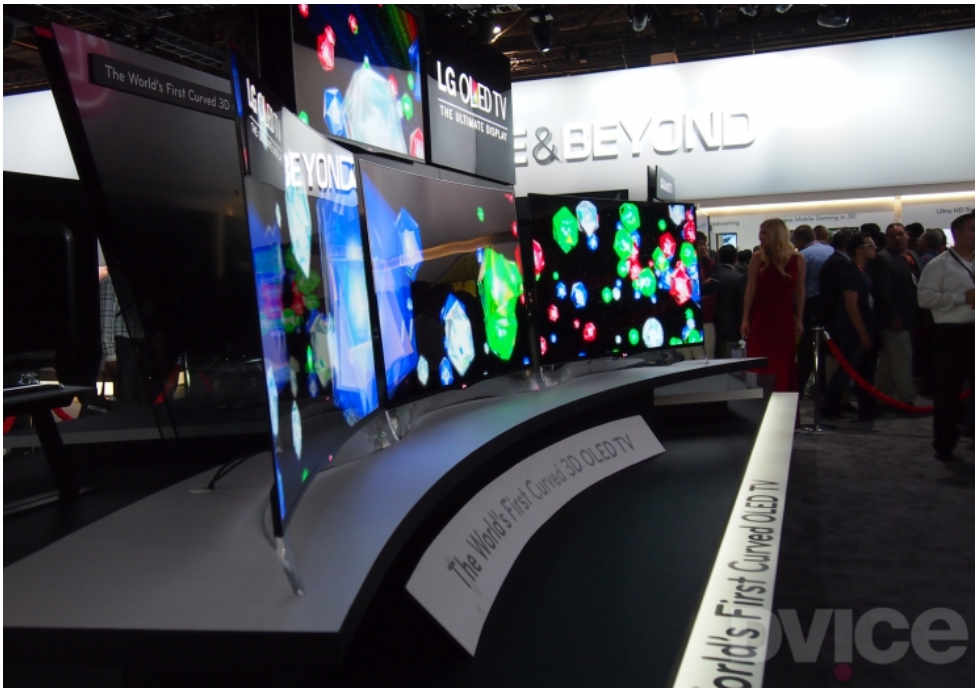

Figure 1.1 The world's first commercialized curved 3D OLED TV (LG display).

industries achieve power conversion efficiency of 11.3% which is suitable to commercialize. For the low-cost electronics, printing technology based on soluble organic materials are expected to serve extreme low-cost radio frequency identification (RFID) tags. In addition to these applications, many efforts to open up new field using organic materials have been tried.

In spite of such a lot of advantages, there are still many issues that need to be improved such as charge injection, mobility, lifetime, operational stability, reliability, and uniformity. Especially, due to low-mobility of organic semiconductors, many researchers have been studied to improve device performance. One of the important issues to make high performance diode is to improve charge injection efficiency. For a p-type semiconductor, even though work function of an anode and HOMO of an organic layer is matched for Ohmic contact, interface dipole is formed at metal/organic interface, limiting charge injection by forming an hole injection

barrier.[4, 5] Six types of possible factors forming interface dipole is summarized by Seki *et al.* as shown in Figure 1.2[6]

The first is charge transfer between the metal and the organic layer with the positive and negative charges separated across the interface as shown in Figure 1.2(a). This phenomenon can occur when the strong acceptor is deposited onto the low work function metal. The second factor is the image effect or the modification of the surface dipole at metal surface as shown in Figure 1.2(b). It is explained to the polarization of the electron cloud attracted by the image charge formed in the metal, which results in the deficiency of electron at the vacuum side that leading to a lowering of the vacuum level (VL). The third factor is the rearrangement of the electron cloud at the metal interface as shown in Figure 1.2(c). The tailing part of the electron cloud is suppressed by repulsion force of the organic layer, leading to lowering of the VL. This mechanism can explain general trend of VL lowering at the metal/organic interfaces. The fourth factor is chemical interaction between the organic and metal layer as shown in Figure 1.2(d). Various chemical interaction results in the rearrangement of the chemical bonds or the formation of new bond, which attributes VL shift. The fifth factor is the possible existence of interfacial states as depicted in Figure 1.2(e). This states act as a buffer layer at the charge exchange between metal and organic layer. Final factor is the permanent dipole as shown in Figure 1.2(f). Polar organic molecules have a permanent dipole moment that can lead to a large interfacial dipole, resulting in VL shift.

Due to the VL shift at the metal/organic interfaces, charge injection barrier can be formed. To reduce this barrier for the high performance organic diode, several methods such as energy level alignment using high work function metals or metal alloys, and inserting buffer layers such as organic materials which has intermediated

energy level, conducting polymers[7], doped-organic layers[8], and transition metal oxides[9] have been developed.

Lee *et al.* introduce another method to reduce injection barrier called electrical annealing which is a method to improve device performance by applying voltage bias for a while after device fabrication.[10] In addition to electrical annealing, the charge injection can be improved by inserting organic materials which have permanent dipole at metal/organic interfaces. The polar organic materials can be treated by employing SAM techniques.[11, 12] These two cases will be discussed in detail below.

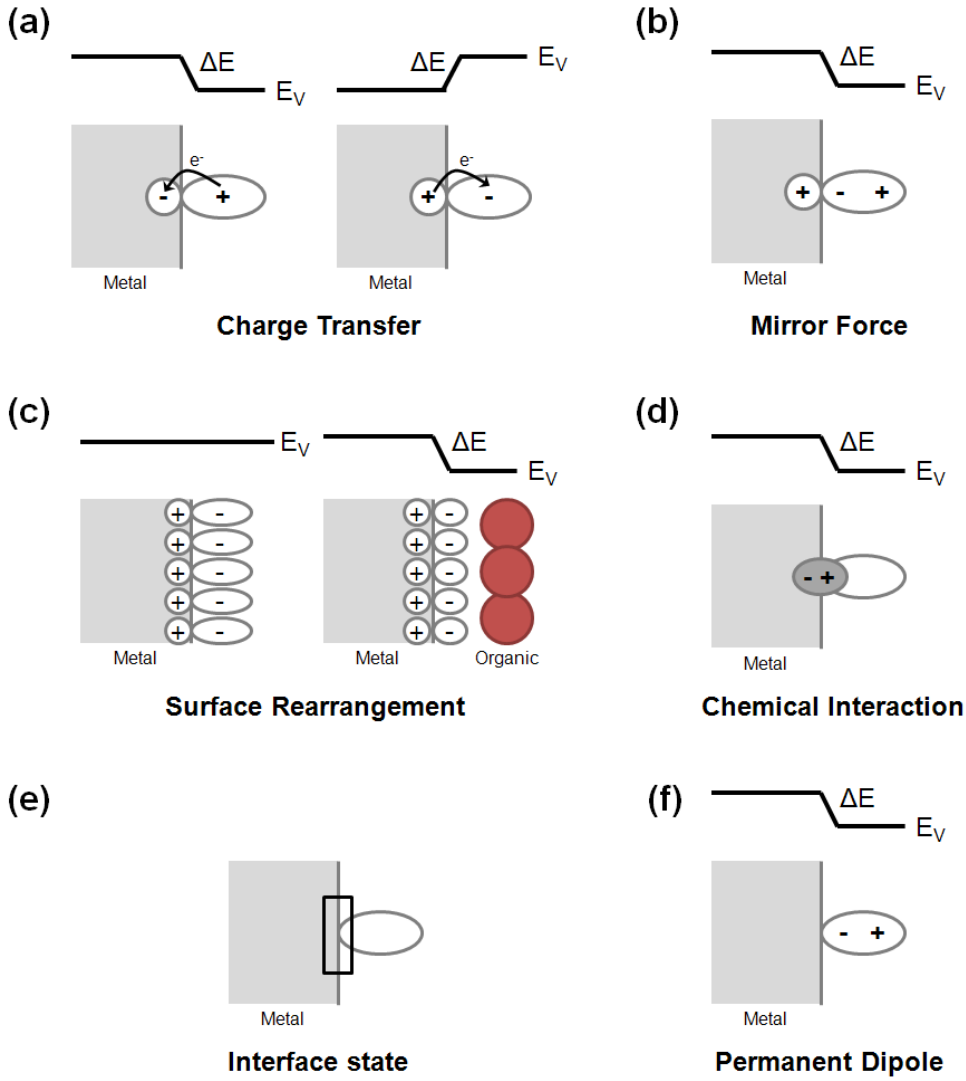

Figure 1.2 Possible factors forming and affecting the interfacial dipole layer. (a) Charge transfer across the interface, (b) Concentration of electrons in the adsorbate leading to positive charging of the vacuum side, (c) Rearrangement of electron cloud at the metal surface, with the reduction of tailing into vacuum, (d) Strong chemical interaction between the surface and the adsorbate leading to the rearrangement of the electronic cloud and also the molecular and surface geometries (both directions of dipoles possible), (e) Existence of interface state serving as a buffer of charge carriers, and (f) Orientation of polar molecules or functional groups.

1.1 Improved Charge Injection by Electrical Annealing

In 2000, Lee *et al.* firstly reported that luminous efficiency of polymer light-emitting diodes (LEDs) can be improved by electrical annealing. They fabricated LEDs using poly(2-methoxy-5-(2'-ethyl-hexyloxy)-1,4-phenylene vinylene) (MEH-PPV) with an Al electrode and then electric field is applied for a while after thermal annealing. With the electrical annealing, onset voltage is dramatically reduced and efficiency is further improved. They suggested that ionic impurities in the polymer film can be oriented along the direction of the electric field, leading to dramatic increase of charge injection.

In 2002, Ma *et al.* reported electrical annealing effect for OLEDs baseed on a conjugate dendrimer doped with 2-(4-biphenylyl)-5-(4-*tert*-bytylphenyl)-1,3,4-oxadiazole (PBD) as a emissive layer.[13] They also obtained that the quantum efficiency of 0.07 % photon/electron and brightness of 2900 cd/m^2 after 1.24 V electrical annealing, which is 6–9 times higher than un-annealed devices. They explained that device improvement after electrical annealing could be due to the charging of traps located near the electrode-emissive layer interface, leading to the ease of charge carrier injection.

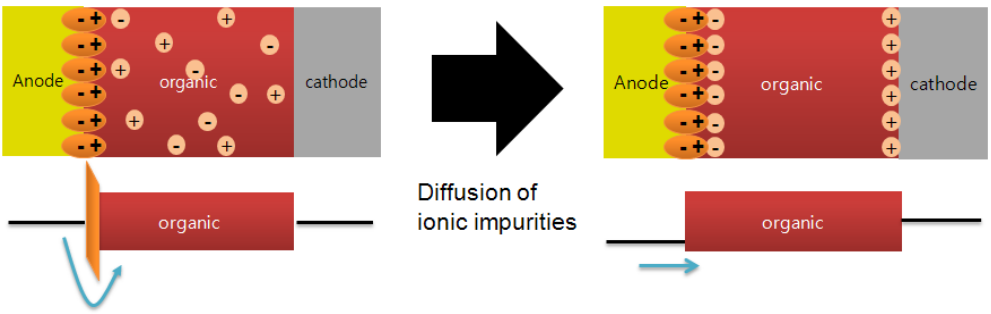

Figure 1.3 Generally explained mechanism of improved charge injection after electrical annealing.

In 2003, Padinger *et al*. reported that the efficiency of poly(3-hexylthiophene) (P3HT) and [6,6]-phenyl C_{61}-butyric acid methyl ester (PCBM) based solar cells can be improved by means of postproduction treatment which applied temperature higher than glass transition temperature (T_g) and voltage higher than open circuit voltage simultaneously.[14] After postproduction treatment, incident photon to collected electron efficiency (IPCE) of around 70 % and power conversion efficiency of around 3.5 % were obtained. They explained that these enhancements are presumed to result parlty from the burning of shunts and an increase of charge carrier mobility.

In 2006, Yim *et al*. reported that overall device performance of fluorescent one-layered OLEDs doped with organic salts can be improved by applying electric and thermal treatment simultaneously.[15] They commented that negative BF_4^- ions are accumulated toward near indium tin oxide (ITO) anode contact, which can assist hole injection and achieve Ohmic contact. In addition, positive Bu_4N^+ ions are accumulated near the Al cathode, which aids the injection of electron from the metal cathode to the organic layer.

In 2008, Li *et al*. reported that organic bulk heterojunction photovoltaic cells based on MEH-PPV and C_{60} composites can be improved by post-thermal treatment under reverse bias.[16] After the device is annealed under the bias of -6 V, the short circuit current and power conversion efficiency is enhanced by a factor of 5 and 5.4, respectively. They explained that external electric field may lead to a modified orientation of polymer chains along the direction of electric field, leading to increase the charge carrier mobility.

In 2009, Sevim *et al*. reported that the performance of polymer LEDs (PLEDs) can be improved by means of post fabrication electric field and heat treatment methods.[17] The PLEDs which have the structure of ITO/PEDOT:PSS/MEH-

PPV/Al were thermally treated at 130 ℃ for 1 hour and then electric field is applied with voltage levels from 0 to -8 V. Electric field treatment after heat treatment lowers the turn-on voltage of PLEDs. The reduced turn-on voltage is due to the orientation of polar molecules, which improves molecular order.

Recently, Park *et al.* presented improved flexible OLEDs having conducting polymer anode on a polyethersulfone (PES) substrates using electrical annealing.[18] They proposed an ionic impurities migration model to explain the improvement after electrical annealing. The PEDOT:PSS anodes contain ionic species which diffuse toward the electrode when the bias is applied. This diffusion induces ionic current flow, leading to form internal electric field which reduces the effective electric field for carrier injection. Consequently, applying electrical annealing can induce the formation of ion-trapped-junction, which results in improved device performance of flexible organic LEDs.

In summary, the origin of electrical annealing has been explained to orientation of polar molecules and diffusion of ionic species in polymer layer. In case of electrical annealing with temperature higher than T_g, the improvement have explained to the orientation of molecules, which leads to increase of mobility and decrease of turn-on voltage. Otherwise, that is electrical annealing only, it has been explained to the diffusion of ionic species toward each electrode, which leads to reduced injection barrier at metal/organic interfaces as shown in Figure 1.3. The ionic species originate from unexpected ionic impurities or dopant that has a polarity in the polymer films. Therefore, this method has only been applied in polymer and solution-processed devices.

1.2 Improved Charge Injection by Self-Assembled Monolayer

SAMs are the methods which attach monolayer of molecules on the surface by chemical bonding. The molecules attached on the surface have anchor group and functional group in the head and tail of the molecules as shown in Figure 1.4. The anchor group should react with the surface to attach the molecules. For example, thiol group (SH) strongly reacts with metal, creating thiolate-metal bond so thiol group is used as the anchor group on the metal surface. Another example of anchor group is trichlorosilane group ($HSiCl_3$) which strongly reacts with SiO_2 surface so it is used on SiO_2 surface. The functional group is selected to the purpose of SAMs. For example, the SAMs of alkyl chains on the SiO_2 surface change surface property from hydrophilic to hydrophobic. In addition, OH^- bonds which act as charge carrier traps on the SiO_2 surface can be effectively removed, improving the device performance. In the same manner, hydroxyl groups (OH) change the surface property to hydrophilic. Due to simple methods, large area applicable, and easy to tune the surface property, SAMs have been widely used to improve device performance.

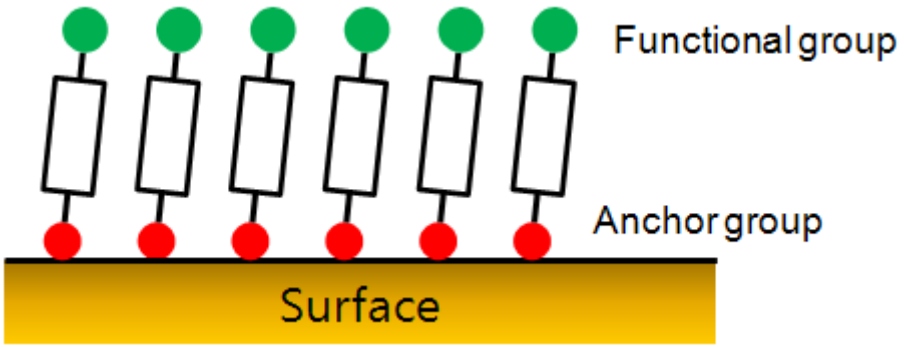

Figure 1.4 Basic structure of SAMs

For the device engineering, SAMs have been investigated to remove charge carrier traps or obtain hydrophobic surface. In addition, SAMs can be used to improve charge injection from a conducting electrode to an organic layer. Due to the different electron affinity of atoms, self-assembled molecules have a permanent dipole moment. Thus, the injection barrier can be reduced using internal electric field induced by a permanent dipole moment of SAMs. In 1996, Campbell *et al.* firstly reported that charge injection can be improved by SAM.[11, 12] They reported that effective work function of silver can be tuned by attaching thiol-terminated SAMs on silver surface. In addition, electron injection from copper to MEH-PPV can also be improved by two conjugated-thiol based SAMs. Since 1996, SAMs have been applied variety of applications in organic electronics such as OLEDs[12, 19-21], OPVs[22, 23], and organic thin-film transistors (OTFTs) [24-26] to improve charge injection. Thiol-based anchor group has been used to attach SAMs on metals. To attach SAMs on oxide based materials such as ITO, SiO_2, HfO_2, and Al_2O_3, trichlorosilane, triethoxysilane, methyl-diethoxysilane, benzoic acid, carboxylic acid, and phosphonic acid, have been used as an anchor group.

1.3 Outline of Thesis

This thesis consists of five chapters including **Introduction** and **Conclusion**. In **Chapter 1**, brief history of organic electronics and importance of study on charge injection is provided. In addition, two major methods, electrical annealing and SAMs which focus on this thesis, to improve charge injection are introduced in detail. In **Chapter 2**, preparation methods of organic diode and characterization methods are described. In addition, the chemical structures of organic materials which used in this thesis are depicted. Basic principles of characterization methods are also included in this chapter. In **Chapter 3**, the improvement of charge injection of pentacene diodes by electrical annealing is investigated. The *I–V* characteristics of pentacene diode with different annealing voltage as function of time are systematically studied. In addition, the electrical annealing effect followed by different hole injection layers (HILs) is investigated. Moreover, ToF-SIMS and impedance are studied to elucidate proper mechanism of electrical annealing in our devices. Finally, some applications of electrical annealing are demonstrated. In **Chapter 4**, the charge improvement of pentacene diode by SAMs is investigated. The change of effective work function of gold is measured by using photoelectron spectrometer. In addition, the morphologies of pentacene on gold and surface-modified gold are studied using AFM, XRD, and Raman spectroscopy. Moreover, mobility of pentacene on gold and surface-modified gold is investigated by means of SCLC of hole-only devices and photo charge extraction by linearly increasing voltage (photo-CELIV) methods. Finally, 1-GHz operating pentacene rectifier is demonstrated. In **Chapter 5**, our studies are summarized and concluding remarks of this thesis are highlighted.

Chapter 2

Experimental Methods

2.1 Materials

2.1.1 Chemical Structures of Organic Materials

Pentacene is well-known organic material having high hole mobility so it is used as an active layer in this thesis. The chemical structure of pentacene is depicted in Figure 2.1. Pentacene was purchased from Tokyo Chemical Industry Co., Ltd.

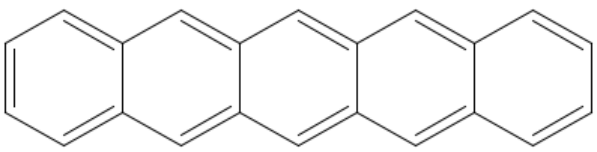

Figure 2.1 The chemical structure of pentacene which is used as an active layer in this thesis

For a HIL between metal/organic interface, MoO_3, CuPc, F_{16}CuPc, m-MTDATA, PEDOT:PSS, and HAT-CN are used, respectively. MoO_3 was purchased from CERAC, inc. and CuPc, F_{16}CuPc, m-MTDATA, and HAT-CN were purchased from Luminescence Technology Corp. The chemical structures of HILs are shown in Figure 2.2. The PEDTO:PSS is purchased from Clevious P (VP AI 4083).

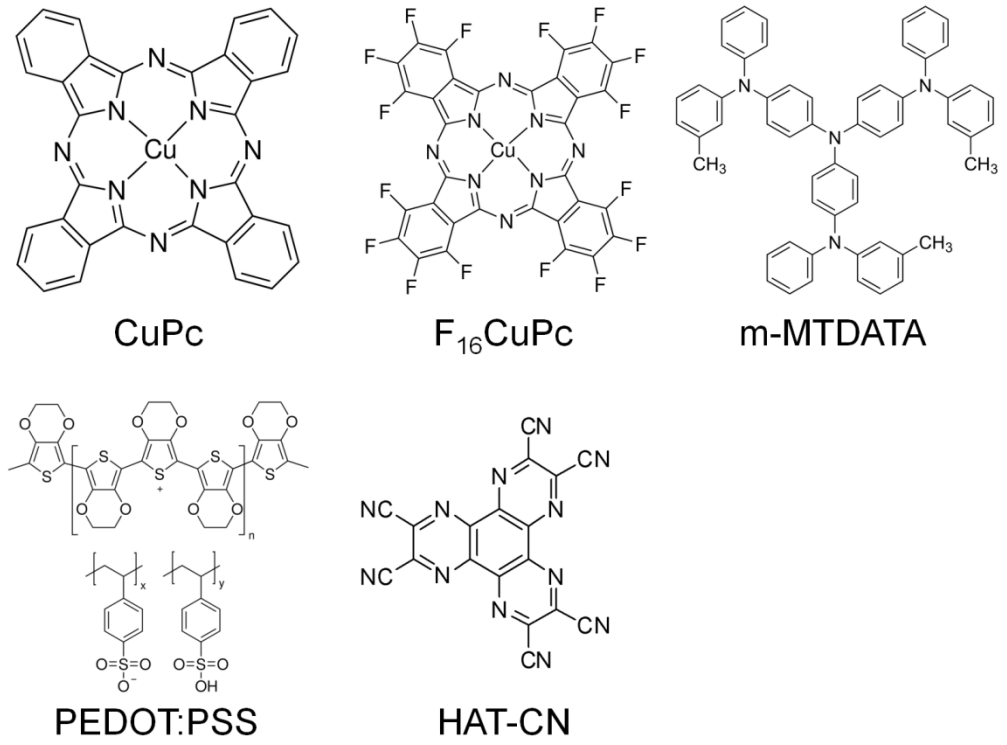

Figure 2.2 Chemical Structures of HILs

For the SAM materials, TP and PFBT are used. Both materials were purchased from Sigma-Aldrich. The chemical structures of SAM molecules are presented in Figure 2.3. All materials were used without further purification.

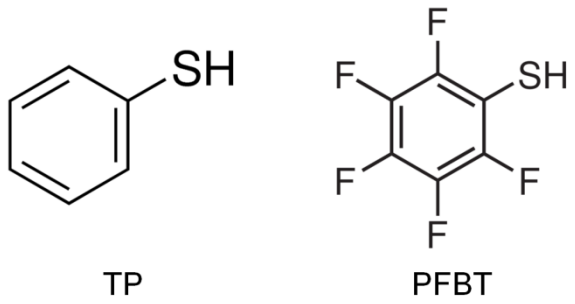

Figure 2.3 Chemical structures of SAM molecules.

2.1.2 Preparation of SAMs Solutions

The 80 μL of TP and PFBT were dissolved in 60 mL of toluene. The concentration of SAM solutions is about 10 mM.

2.2 Device Fabrication Methods

All glass substrates were cleaned in an ultrasonic bath with acetone, isopropyl alcohol, and de-ionized water for 20 minutes in sequence. After that, the substrates were dried at 120 °C in an oven for more than 30 minutes. The deposition rate of pentacene was about 0.3 nm/s in order to prevent shunt. After the diode is fabricated, samples were encapsulated in a Ar-filled glove box using UV-curable sealants. Top and bottom electrodes were formed crossbar geometry with 80 μm x 80 μm areas.

2.2.1 Preparation of Pentacene Diodes for Electrical Annealing

Au (50 nm), MoO_3 (5 nm), pentacene (90 nm), Al (80 nm) were thermally evaporated successively on the substrates under high vacuum conditions (approximately 5×10^{-6} torr). The evaporation rate of Au, MoO_3, pentacene, Al was about 1, 0.5, 3, and 3–5 Å/s, respectively. After the diode is fabricated, voltage is applied to the diode while current is saturated. The device structure and energy band diagram is depicted in Figure 2.4.

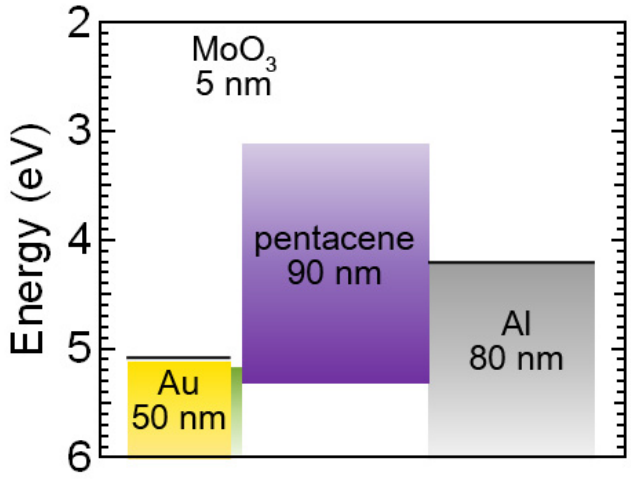

Figure 2.4 Device structure and energy diagram of pentaceme diode for electrical annealing

2.2.2 Preparation of Pentacene Diodes with SAM-treated Gold

The 50-nm-thick gold was thermally deposited on glass substrates under high vacuum conditions. Then, the TP and PFBT were treated on gold under ambient conditions. The substrates were dipped in each SAM solutions for 2 minutes and rinsed with toluene. After that, SAM-modified gold was dried in vacuum condition for 10 minutes at room temperature. Finally, 110-nm-thick pentacene and 100-nm-thick Al was thermally evaporated under high vacuum conditions (3×10^{-6} torr). The proposed device structure is presented in Figure 2.5.

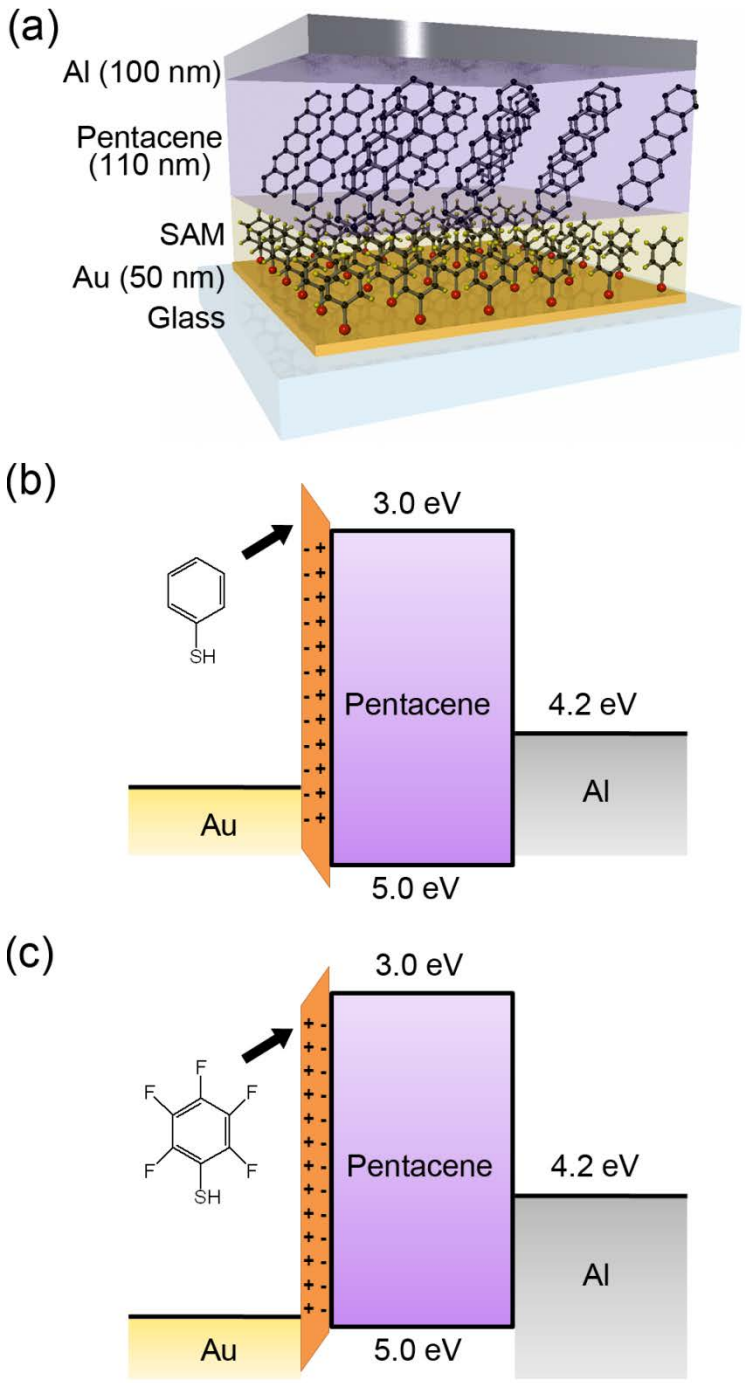

Figure 2.5 (a) The structure of pentacene diodes with surface-modified gold. Energy diagram of pentacene diodes with (b)TP- and (c)PFBT-treated gold.

2.2.3 Measurement Setup of Pentacene Rectifiers

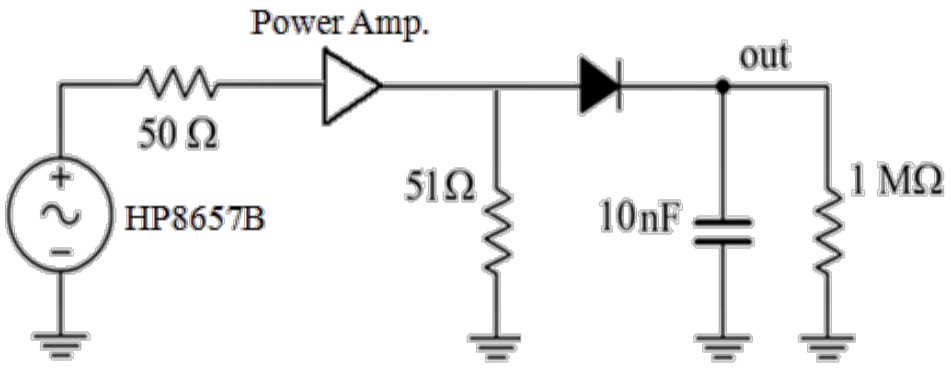

Figure 2.6 The equivalent circuit of a rectifier measurement setup

The equivalent circuit of pentacene rectifier is presented in Figure 2.6. The rectifier is consists of a 1-MΩ resistor and 10-nF capacitor. The diode is firstly connected by plastic circuit board (PCB) with 50 Ω-designed microstrip lines and 10-nF chip capacitor. Then, the rectifier is connected to a signal generator (HP8657B) with power amplifier (Empower RF Systems Inc. BBM1C4AEL) and an oscilloscope (Tektronix TDS5104) using Bayonet Neill-Concelman (BNC) and SubMiniature version A (SMA) cables. Since the input signal is power source, 51-Ω chip resistor on PCB is used to define voltage.

2.3 Device Characterization Methods

2.3.1 Carrier Transport in Organic Semiconductors

When the charge injection barrier between metal/organic interfaces is high, charge carrier is limited by charge injection so current is determined by the metal/organic interfaces. According to the thermionic emission model, the hot carriers which have their kinetic energy more than the energy of charge injection barrier can flow. The current of thermionic emission model can be expressed by

$$I = I_S(\exp\frac{eV}{k_BT} - 1). \tag{2.1}$$

Where the I_S is the saturation current, e is the elementary charge, V is the applied voltage, k_B is Boltzmann constant, and T is the temperature. I_S is expressed as

$$I_S = AA^*T^2\exp(-\frac{\Phi_B}{k_BT}), A^* = \frac{4\pi k_B^2 m^*}{h^3}. \tag{2.2}$$

Where the A is the area of the diodes, A^* is Richardson constant, Φ_B is the Schottky barrier height, m^* is the effective mass, and h is Plank constant. If the potential barrier is very high, carriers cannot be injected beyond the barrier. In this case, charge carriers are injected by tunneling rather than thermionic emission. Fowler–Nordheim proposed carrier transport model by tunneling, which can be expressed as[27]

$$J \propto E^2 \exp(-\frac{\kappa}{E}). \tag{2.3}$$

Where the E is the electric field and κ is the value depending on the potential barrier shape. If the high voltage is applied, the potential shape is approximately considered as a triangle. Then, the κ can be expressed as follows:

$$\kappa = \frac{8\pi\sqrt{2m^*\Phi_B^3}}{3eh}. \tag{2.4}$$

If the injection barrier is small to negligible or metal/organic contact forms Ohmic, then the current is limited by bulk characteristics. At the low voltage, the whole injected charge is ejected through the other metal electrode so there is no charge distribution in the organic semiconductor. In this case, the carrier transport is followed by Ohm's law which can be expressed by

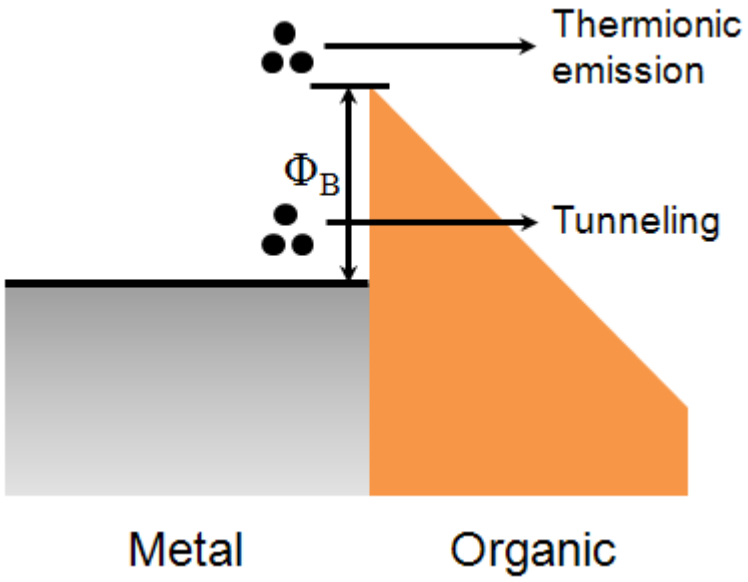

Figure 2.7 Schematic of charge injection at metal/organic interfaces.

$$J = en\mu E\,. \tag{2.5}$$

Where the n is the carrier concentration and μ is the carrier mobility of the organic semiconductor. As the voltage increases, more charge carriers are injected before fully ejected, leading to remaining space charges. This current called as SCLC which also called as Mott–Gurney law. If there is no charge traps, SCLC can be expressed by

$$J = \frac{9}{8}\varepsilon_0\varepsilon_r\mu\frac{V^2}{d^3}\,. \tag{2.6}$$

Where the ε_0 is the vacuum permittivity, ε_r is the relative permittivity, and d is the thickness of the organic semiconductor. If the charge traps exist in the organic semiconductor, the SCLC equation is more complicated. Assuming that the traps are exponentially distributed, the current can be expressed as follows:[28]

$$J \approx e^{1-m}\mu N_C\left(\frac{2m+1}{m+1}\right)^{m+1}\left(\frac{m}{m+1}\frac{\varepsilon_0\varepsilon_r}{N_t}\right)^m\frac{V^{m+1}}{d^{2m+1}}, m = \frac{T_t}{T}\,. \tag{2.7}$$

Where the N_C is the effective density of conduction band states, N_t is the trap density, T_t is the temperature parameter characterizing the trap distribution.

2.3.2 *I–V* characteristics measurement

To measure *I–V* characteristics, the pentacene diodes were mounted onto the cryostat. The *I–V* characteristics were measured by a Keithley 236 source measurement unit.

2.3.3 Frequency Response of Pentacene Rectifiers

The rectifier circuit sets up as shown in Figure 2.6. The rectifiers converts ac source to dc source. When the forward bias is applied, the electron moves via diode and the capacitor is charged. Ideally, in this time voltage is equal to maximum voltage of sinusoidal input voltage. When the reverse bias is applied, the electron cannot move via diode and the voltage is remained. Only small leakage current and power consumption in load resistor will reduce the voltage, which makes ripple voltage in the output voltage. As the frequency increases, the impedance of capacitance in the diode is reduced so charge carrier is leaked via the diode when the reverse bias is applied. Therefore, the output voltage decreases as frequency increases. If the organic diode is followed by trap-free SCLC as expressed in Eq. (2.6) and there is no leakage current at reverse bias, then the maximum frequency response of organic diode can be calculated as follows:[29]

$$f_{msx} = \frac{9\mu}{16\pi d^2 V_{OUT}}\left[(-3V_{OUT}+V_F)\sqrt{V_A^2-(V_{OUT}+V_F)^2}+(V_A^2+2V_{OUT}^2)\arccos(\frac{V_{OUT}+V_F}{V_A})\right] \quad (2.8)$$

Where V_{OUT} is the output voltage of the rectifier, V_F is the transition voltage at which conduction mechanism is converted Ohmic into SCLC, and V_A is the applied voltage. If the transport time in the organic is t_τ, maximum frequency can also be expressed by

$$f_{\max} = \frac{1}{t_\tau} = \frac{\mu(V_A - V_{OUT})}{d^2}. \quad (2.9)$$

Note that these equations can olny show the limitation of frequency. In real cases, frequency response if normally smaller than above equations due to reverse-

bias leakage current of the diode, smaller forward-bias current than theoretically expected, and parasitic capacitance.

If the diode is considered as a single RC component, the transfer function can be expressed by

$$H(\omega) = \frac{V_{OUT}}{V_A} = \frac{1}{1 + j\,\omega/\omega_C}. \tag{2.10}$$

Where ω_C is the cutoff frequency. Therefore, the magnitude of output voltage can be expressed by

$$V_{OUT} = V_A\left|H(\omega)\right| = \frac{V_A}{\sqrt{1+\left(\omega/\omega_C\right)^2}} = \frac{V_A}{\sqrt{1+\left(f/f_C\right)^2}}. \tag{2.11}$$

2.3.4 Mobility Measurements

The mobility is one of the key parameters of organic semiconductors. Thus, a lot of methods such as time-of-flight photoconductivity (TOF-PC),[30] Hall effect,[31] field-effect transistor (FET),[32] dark injection,[33] SCLC,[34] and photo-CELIV[35-37] have been developed to determine mobility of organic semiconductor. Among these methods, TOF-PC and dark injection need to thick layer because transit time for carrier in organic film should be larger than RC time constant of the circuits. In addition, for these two methods, carrier relaxation time should be longer than transit time, which limits measuring range of mobility up to 10^{-2} cm^2/Vs. mobility measuring by FET has wide measuring range but the mobility measured by FET is higher than real value because charges accumulated by gate voltage filled traps. In addition, FET mobility is lateral mobility, which may be different of vertical mobility due to the molecular structure. Likewise, the mobility measured by Hall effect measurement is different from mobility of a real device. Thus, in this study, we focused on SCLC measurement and photo-CELIV techniques.

To measure the mobility by using SCLC, the contact between metal/organic should be Ohmic. By assuming 100 % injection efficiency, mobility can be extracted by Eq (2.6).

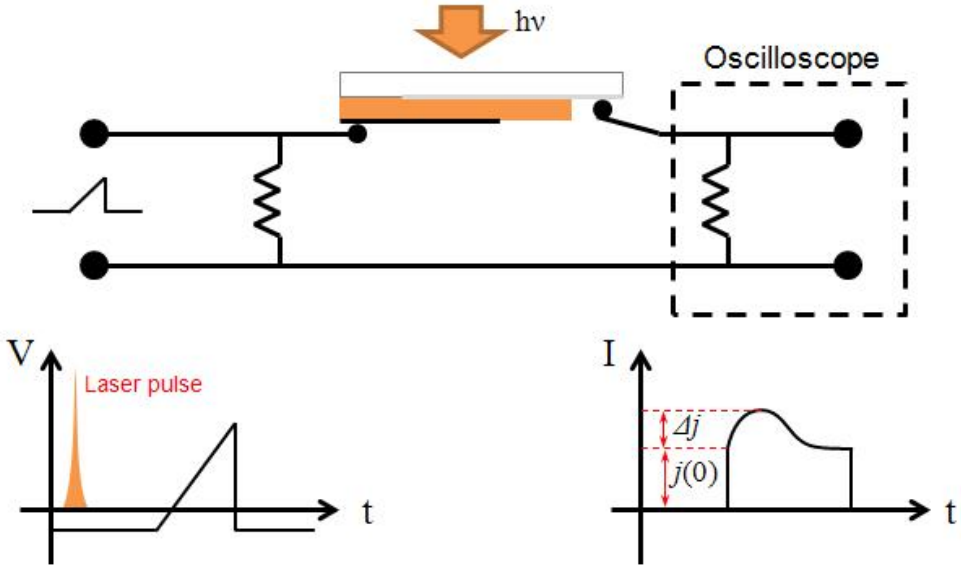

Figure 2.8 The schematic of photo-CELIV measurement setup.

In 2000, Juska *et al.* developed new technique to determine mobility of thin films, which is called as CELIV. To measure mobility by CELIV, charge injection at the metal/organic interface is prohibited. When the linearly increasing voltage is applied, free charge carrier in the thin-film is ejected, making additional current in addition to displacement current by capacitance of the diode. From the peak of the transient current, the mobility can be extracted using this equation.

$$\mu = \frac{2d^2}{3At_{max}^2\left[1+0.36\frac{\Delta j}{j(0)}\right]} \tag{2.12}$$

Where the A is voltage rising speed ($=dV/dt$), t_{max} is the time at the maximum current peak, Δj is the additional current maximum, and $j(0)$ is the displacement current of the capacitor of the thin-film. The Using this equation, mobility can be calculated. However, the organic semiconductors usually have insufficient free

charge carriers so Δj is too small to measure. To excite free carrier in the organic film, laser pulse is illuminated before the voltage is applied, which is called as photo-CELIV. The measurement setup of photo-CELIV is presented in Figure 2.8.

In this study, the Nd-Yag laser was used to illuminate laser pulse to the pentacene samples. Function generator (AFG3101, Tektronix) was used to apply linearly increasing voltage. For making delay between laser pulse and linearly increasing voltage, photodiode signal is used as a trigger of the function generator. The digital oscilloscope (TDS054B, Tektronix) was used with a 50-Ω load resistor.

2.3.5 Impedance Spectroscopy

Impedance spectroscopy is useful technique to study interface and bulk characteristics of the devices. It measured both resistive and reactive components simultaneously as a function of frequency. The impedance spectra are plotted, which is called as Cole-Cole plots that have imaginary part of impedance as a y-axis and real part as an x-axis. Cole-Cole plots of the devices may contain a few of overlapped circles which can be modeled as RC components. Sometimes it presents depressed circles which can be modeled as CPE. CPE is usually appeared in the diffusion-recombination process, real system that has non-homogeneity. For example, porous and rough electrode surfaces can be lead to frequency dispersion of the interface impedance. To model the rough electrode, various equivalent circuit models such as a transmission line, V-shape groove, branched transmission line, and fractal shape have been suggested to explain CPE behavior. In this study, the impedance spectra are measured by Wayne Kerr Electronics 6550B.

2.3.6 ToF-SIMS Measurement

ToF-SIMS is surface analysis using the pulsed ion beam. When incident particles impact on the surface of the sample, charged molecules which are attached at the surface accelerate into a detector by electric field. By analyzing the flight time, mass of molecules can be determined. By measuring ToF-SIMS, the distribution of molecules along the vertical axis can be analyzed. In this study, O_2 ion gun is used for sputtering to get positive secondary ion profiles. The ToF-SIMS depth profiling is measured under ultra-high vacuum (UHV) conditions. The analysis area is 40 μm × 40 μm.

2.3.7 Raman Spectroscopy

Raman spectroscopy is photospectroscopy detecting vibrational, rotational modes in the thin-films. When the monochromatic light is exposed to the samples, electrons in the molecules are excited from ground state and fall into vibrational energy states. Using this different photon energy, the vibrational energy states can be detected. In this study, integrated Raman-AFM system is used with five different wavelength laser sources—457, 488, 514, 633, and 785 nm.

2.3.8 Other Characterization Methods

AFM: To obtain topography of films, XE-100 (Park systems) AFM is used. The films were measured in non-contact mode with Nanosensors^{TM} ppp-NCHR tip (320 kHz, 42 N/m) under ambient condition.

XRD: The crystallinity of pentacene on gold and surface-modified gold was analyzed by XRD. XRD patterns are obtained from New D8 Advance (Bruker).

Energy level measurement: The work function of gold and surface-modified gold is measured by model AC-2 photoelectron spectrometer (RKI Injstruments) under ambient condition.

UV-Visible absorption measurement: The absorption spectra were obtained by means of UV-Vis absorption spectrometer (CARY5000, Agilent). Since the glass substrates absorb UV light itself, all samples were prepared on the quartz substrates.

Chapter 3

Improved Injection Efficiency of Organic Diodes by Electrical Annealing

To date, the electrical annealing method has mainly been applied to solution-processed devices that have ionic species in the polymer film such as polymer light-emitting diode and polymer photovoltaic devices because the electrical annealing effect is originated from diffusion and migration of ionic species toward electrodes. Thus, it has not been applied to thermal-deposited devices which cannot have ionic species in the organic layer. Moreover, the proper mechanism of the electrical annealing has not completely understood. Here, we applied electrical annealing to a pentacene diode with MoO_3 as a HIL and demonstrated organic rectifiers based on this diode. The results show that forward-bias current density of the pentacene diode is dramatically increased without increase of reverse-bias leakage current after electrical annealing which leads to improvement of the cutoff frequency of the

rectifier even though there is no ionic species in the pentacene films. We also investigated to find proper mechanism of electrical annealing effect on the pentacene diode with MoO_3 by means of ToF-SIMS, AFM, and impedance spectroscopy.

3.1 Systematic Investigation into Improved Device Performance of Pentacene Diodes after Electrical Annealing

3.1.1 *I–V* Characteristics of Pentacene Diodes Applying Constant Voltage or Constant Current

The *I–V* characteristics of the pentacene diodes whose structure is depicted in Figure 2.4 with applying constant voltage or constant current were measured as shown in Figure 3.1. Before electrical annealing as shown in the black solid lines of Figure 3.1, the turn-on voltage is approximately 1.3 V and current at 3 V is 0.1–0.2 mA. When the constant voltage or current is applied to the diode, current is increases and turn-on voltage is decreases as applying time increases. After 332 sec for applying 5 V, and 80 sec for applying 6 mA, current is finally saturated. The turn-on voltage is reduced from approximately 1.3 V to 0.2 V and current at 3 V is increased from approximately 0.2 mA to 1 mA. It is note that even though the forward-bias current is dramatically increased, the reverse-bias leakage current is not changed after electrical annealing. In the constant voltage case, the applied power to the diode is increases as time increases so the Joule heat is increases. The mobility of pentacene increases as temperature increases because the conduction mechanism is hopping transport. Whereas, in the constant current case, the applied power to the diode is decreases as time decreases. Thus, current saturation time of constant voltage case is longer than that of constant current case.

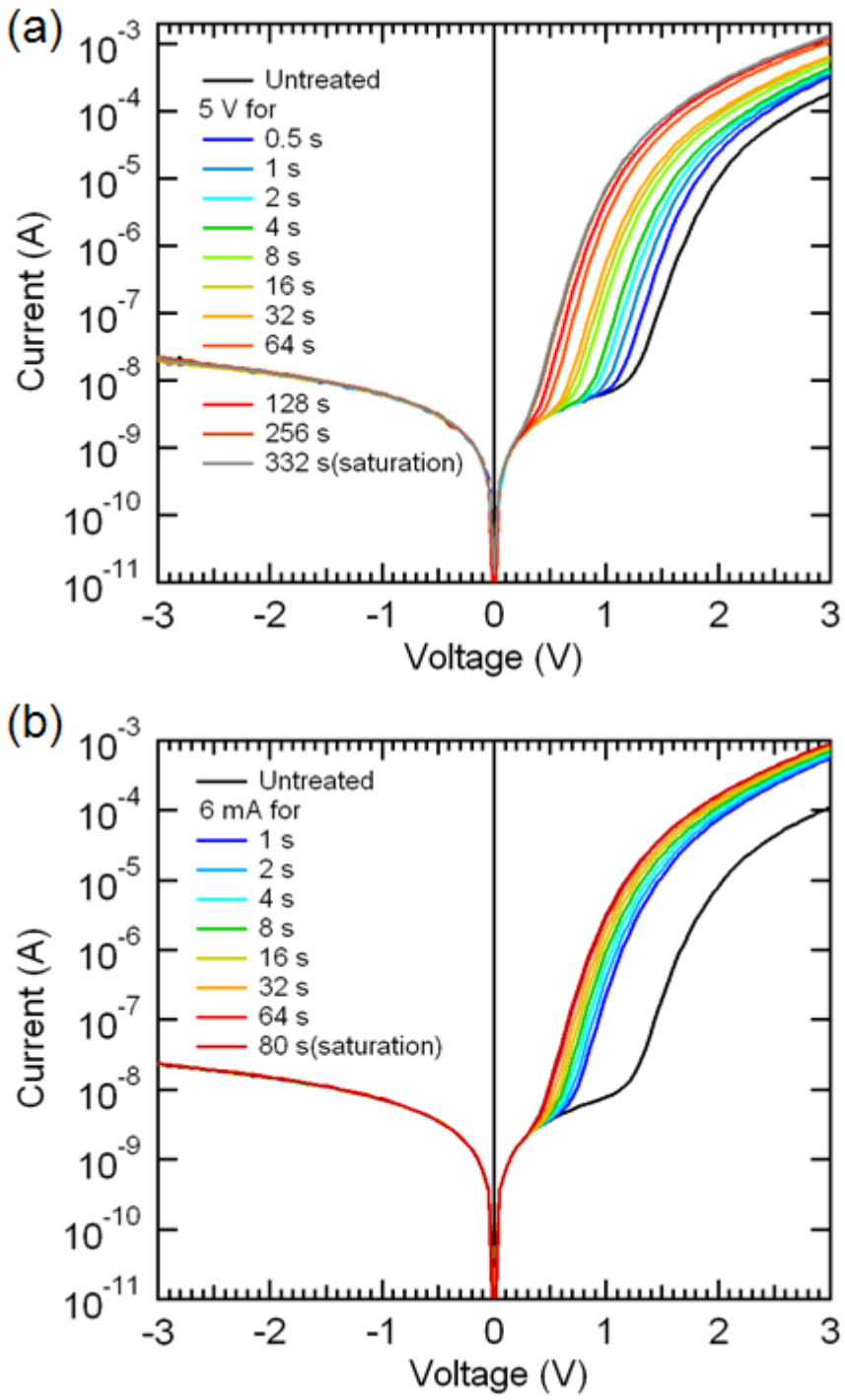

Figure 3.1 *I–V* characteristics of pentacene diodes applying (a) constant voltage or (b) constant current.

3.1.2 Current Characteristics of Pentacene Diodes with Electrical Annealing

Various voltages were applied to pentacene diodes until currents were saturated. Figure 3.2(a) shows change of currents with time while various voltages were applied. While the voltage is applied to the diode, current is continuously increased and finally saturated. Solid lines are fitting lines of exponential saturation model, which can be written as

$$I = I_{sat} - I_0 \exp\frac{t}{\tau}. \tag{3.1}$$

Where I_{sat} is the saturation current, I_0 is the current constant, and τ is the characteristic time of saturation. The extracted I_{sat}, I_0, and τ using above equation are shown in Figure 3.2(b). τ is 203, 23.3, and 6.74 sec. for annealing voltage of 4, 5, and 6 V, respectively. The saturation time is decreased as annealing voltage is increased. In addition, total Joule heat during the electrical annealing process, calculated by integrating applied power with time as follows

$$\begin{aligned} Q &= \int_0^\tau P(t)dt = \int_0^\tau VI(t)dt \\ &= \int_0^\tau V\left[I_{sat} - I_0 \exp\frac{t}{\tau} \right]dt \\ &= VI_{sat}\tau + VI_0\tau(e^{-1} - 1) \end{aligned} \tag{3.2}$$

Where Q is the total Joule heat applied to the diodes during the electrical annealing process. Q is calculated to be 0.927, 0.397, and 0.297 J for the diode with applying voltage of 4, 5 and 6 V, respectively, which is summarized in Table 3.1. If the Joule heat is dominant factor of electrical annealing, improvement of device

performance should depend on total heat. However, the device performance improvement, shown in Figure 3.2(c), increases as applied voltage increases but total Joule heat is decreased as applied voltage increases, indicating that the current increase by electrical annealing is more affected by electric field rather than Joule heat.

Table 3.1 Calculated total Joule heat applied to the pentacene diode during electrical annealing process.

Voltage (V)	τ (s)	Q (J)
4 V	203	0.927
5 V	23.3	0.397
6 V	6.74	0.267

Figure 3.2 (c) shows *I–V* characteristics of pentacene diodes after electrical annealing with various annealing voltage. Before electrical annealing, turn-on voltage of the pentacene diode is about 1.25 V. After electrical annealing, however, turn-on voltage is gradually reduced as applied voltage increases and finally it becomes 0.44 V when voltage of 6 V is applied. Moreover, forward-bias current is increased by 4.4 times at 3 V without change of reverse-bias leakage current, resulting that the rectification ratio is increased from 8.31×10^3 to 3.34×10^4 at 3 V. The turn-on voltage is related to undesirable injection barrier located at Au/MoO_3/pentacene interface so reduced turn-on voltage implies that the injection barrier is reduced. Furthermore, current density of a pentacene diode without a MoO_3 layer is not increased even after electrical annealing, indicating that

improvement of current characteristics is attributed to a change of interface located at Au/MoO_3/pentacene. When applied voltage is higher than 6.5 V, reverse-bias leakage current increases and finally the device breaks down, indicating that a large amount of Joule heat deteriorate the device.[38, 39] Therefore, proper applied power is carefully chosen to maximize the electrical annealing effect.

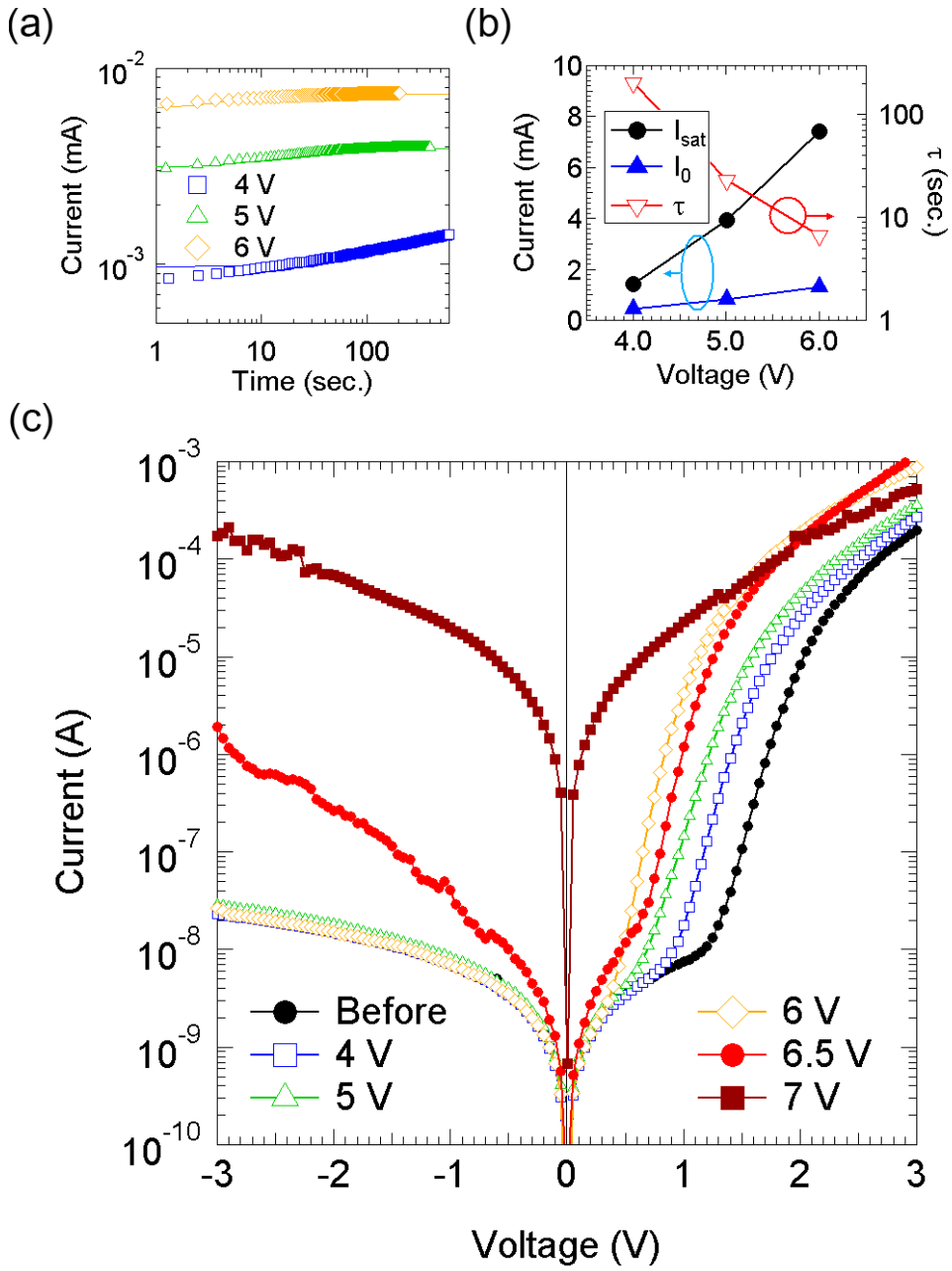

Figure 3.2 (a) Change of current with time while various voltages are applied. (b) Extracted parameters of current with time using exponential saturation model. (c) *I–V* characteristics of pentacene diodes with various annealing voltage.

3.1.3 *I–V* Characteristics of Pentacene Diodes with Various HILs

The *I–V* characteristics of pentacene diode with various HILs are shown in Figure 3.3. For the PEDOT:PSS, UV-ozone was treated on gold surface for 10 min in order to make hydrophilic surface. Then, 40 nm of PEDOT:PSS was spin-coated on gold at 4000 rpm for 60 sec. a 10-nm thick CuPc and m-MTDATA were thermally deposited on gold.

Among these HILs, CuPc and m-MTDATA are well-known HILs for OLEDs. These materials have a moderate HOMO levels so the HOMO level is located at the middle between metal and a hole transporting layer in OLEDs. However, the HOMO level of pentacene is lower than that of CuPc and m-MTDATA so these HILs act as injection barrier. Thus, the forward-bias current of pentacene diodes with CuPc and m-MTDATA is limited by them as shown in Figure 3.3.

Other HILs properly act as HIL. In the PEDOT:PSS case, large reverse-bias leakage current is observed due to high conductivity of PEDOT:PSS. Since the PEDOT:PSS is coated entire glass substrate without patterning, created lateral leakage paths can increase the reverse-bias leakage current. The interesting thing is that the pentacene diode using PEDOT:PSS as a HIL has no effect on the electrical annealing. Even though the PEDOT:PSS has ionic species, they do not diffused by electric field. In the case of PFBT, small turn-on voltage is observed without electrical annealing unlike other HILs. The PFBT has permanent dipole moment so it is considered that this permanent dipole effectively reduces the charge injection barrier. The HAT-CN and F_{16}CuPc shows that the turn-on voltage is reduced and current is increased without any change of reverse-bias leakage current. Unlike other HILs, transition metal oxides such as V_2O_5, WO_3 and MoO_3, HAT-CN, and F_{16}CuPc have deep HOMO and LUMO level. The HOMO levels of MoO_3, HAT-CN, and

F_{16}CuPc are reported as 9.1–9.7,[40-43] 9.9,[44] and 6.1–6.4 eV,[45] and the LUMO of them are reported as 6.2–6.7,[40-43] 6.0,[44] and, 4.6–4.9 eV,[45] respectively. Therefore, the work function of metal and organic layer is matched with LUMO levels of these HILs. This specific characteristic may be the origin of improved device performance by electrical annealing.

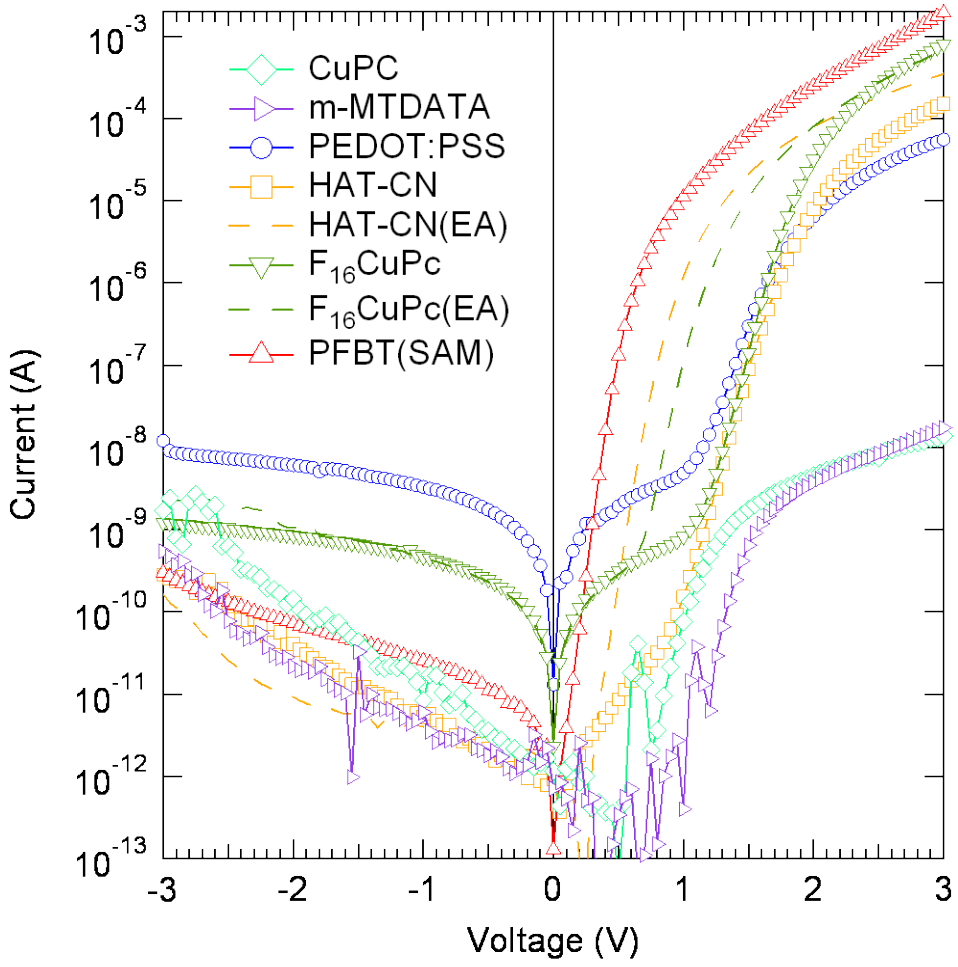

Figure 3.3 *I–V* characteristics of pentacene diodes with various HILs.

3.1.4 Frequency Characteristics of Pentacene Rectifiers

When 10-V sinusoidal voltage is applied to the diodes, frequency characteristics of pentacene rectifiers are shown in Figure 3.4. To avoid ripple voltage, a load capacitor times a load resistor should be much larger than the period of an input signal and also a capacitance of the diode should be much smaller than a load capacitor.[29, 46] A capacitance of the pentacene diode was measured to be 6.5 pF, satisfying above conditions. After electrical annealing, output voltage is increased from 3.70 V to 6.66 V at 14 MHz without ripple voltage. Also, output voltage tends to decrease slowly as frequency increases after electrical annealing. If the diode is considered as a single RC model, the cutoff frequency (f_c) can be obtained by fitting to the experimental data using Eq. (2.11). The cutoff frequency of the rectifier is increased from 10.5 MHz to 85.7 MHz after electrical annealing. As the frequency increases, additional leakage current caused by capacitance of the diode discharges accumulated charge in the load capacitor, decreasing output voltage. If forward bias current of the diode increases after electrical annealing, more charges are accumulated to the load capacitor at the charging period so these additional accumulated charges compensate leakage current, improving frequency performance.

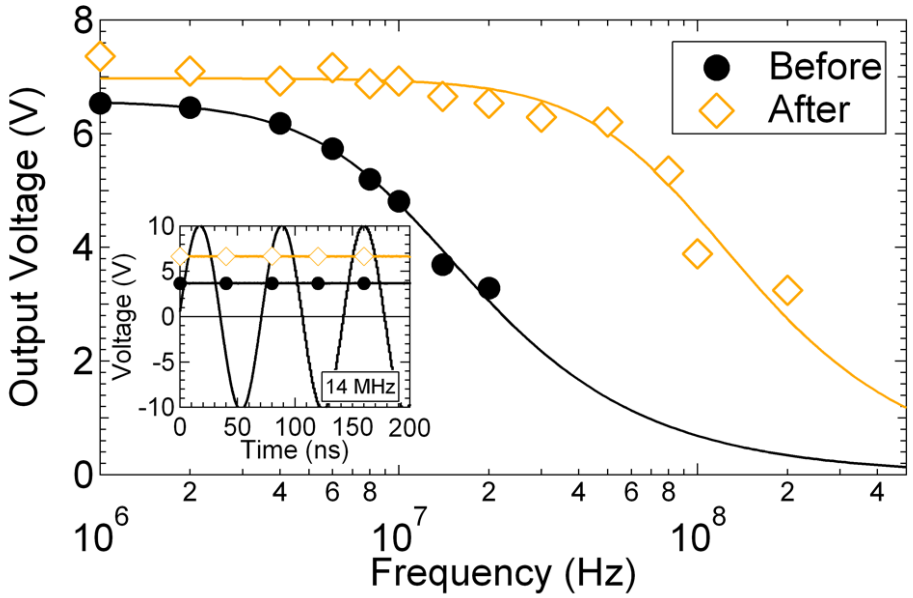

Figure 3.4 Frequency characteristics of the pentacene rectifiers before (open diamond) and after (closed circle) electrical annealing. The solid line is fitting line of single-RC transfer function model.

3.1.5 Thermal Annealing Effect on Pentacene Diodes

To investigate the thermal annealing effect only on pentacene diode, the pentacene diode on glass substrates were placed on the hot plate in the Ar-filled glove box. The *I–V* characteristics of pentacene diode with different annealing temperature are shown in Figure 3.5. Unlike the electrical annealing case, there is no improvement of current or reduction of turn-on voltage by using temperature annealing only, indicating that electric field plays an important role for electrical annealing.

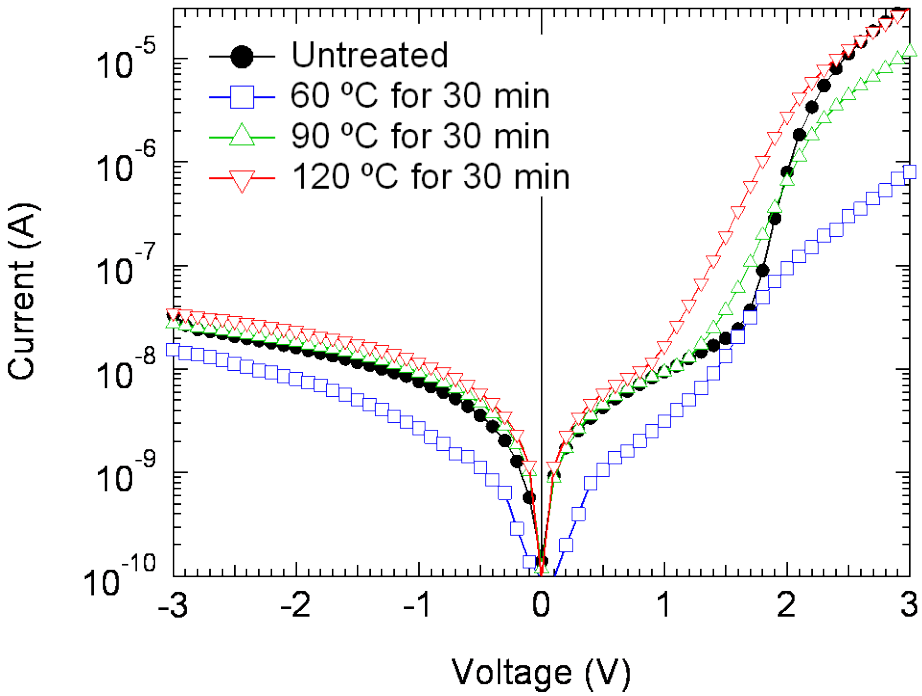

Figure 3.5 Thermal annealing effect on Pentacene diode with different temperature.

3.1.6 Hysteresis of the Pentacene Diodes before and after Electrical Annealing

Figure 3.6 shows hysteresis of pentacene diode before and after electrical annealing. Both before and after electrical annealing, no hysteresis is observed. If there are a lot of interface states at the Au/MoO_3/pentacene interface, some charges injected from gold to pentacene are captured at the interface, resulted in voltage shift toward negative direction. However, the pentacene diodes before and after electrical annealing do not show any voltage shift, implying that there are few of interfacial states at Au/MoO_3/pentacene interfaces.

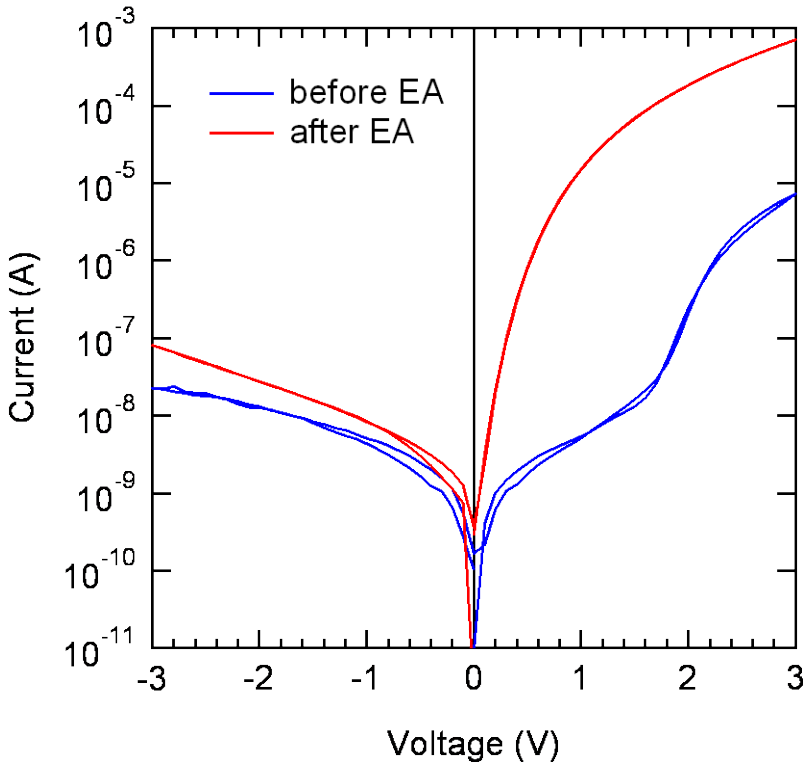

Figure 3.6 Hysteresis of pentacene diodes before and after electrical annealing.

3.2 Investigation into Proper Mechanism of Electrical Annealing

3.2.1 ToF-SIMS Measurements

For the further study, the depth profiling of pentacene diodes before and after electrical annealing was investigated by ToF-SIMS as shown in Fig. 4. The Au, Mo, C, and Al in Fig. 4 are markers of Au, MoO_3, pentacene, and Al, respectively. The vertical distribution of pentacene and Au is similar before and after electrical annealing. However, the distribution of Mo species is broader toward the pentacene region after electrical annealing, indicating that MoO_3 is diffused into the pentacene layer. These results suggest that MoO_3:pentacene mixed layer is provided at Au/MoO_3/pentacene interfaces. As the MoO_3 has widely been used as a p-dopant material,[47, 48] the MoO_3:pentacene mixed layer increases carrier concentration at the interface, providing more efficient charge injection. The Al is also detected at deeper region after electrical annealing, implying that Al is penetrated into the pentacene layer as well. The thermal-deposited pentacene forms a polycrystalline film so the interface at pentacene/top electrode cannot exhibit flat surface. Therefore, the Al, deposited on top of polycrystalline pentacene film, may forms some spikes at the grain boundary of pentacene. These spikes induce higher electric field so Al at this region may be easily penetrated into the pentacene films.

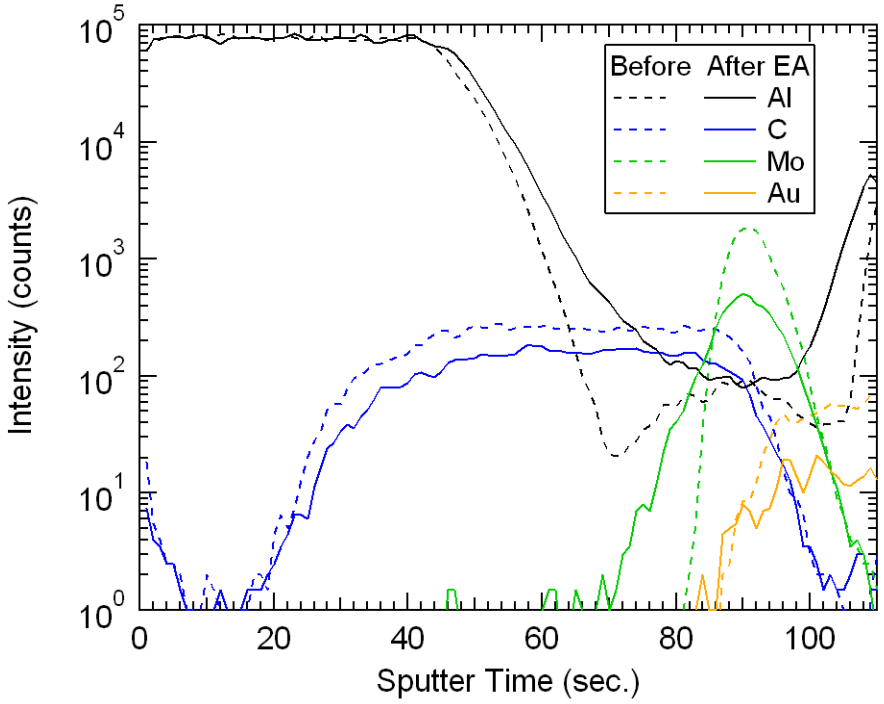

Figure 3.7 ToF-SIMS depth profiles of the pentacene diodes before (dashed line) and after (solid line) electrical annealing.

3.2.2 Pentacene Diodes with MoO_3 Doped Pentacene as a HIL

The ToF-SIMS results show that the pentacene:MoO_3 mixed layer is created. Thus, the pentacene:MoO_3 doped layer is intentionally inserted between MoO_3 and pentacene layer to find the role of pentacene:MoO_3 mixed layer. The concentration of MoO_3 is 25 vol.%. Firstly, the absorption spectra of pentacene, MoO_3, and pentacene:MoO_3 mixed layer is measured by UV/Vis absorption spectrometer. The absorption spectra of pentacene, MoO_3, and pentacene:MoO_3 mixed layer are depicted in Figure 3.8.

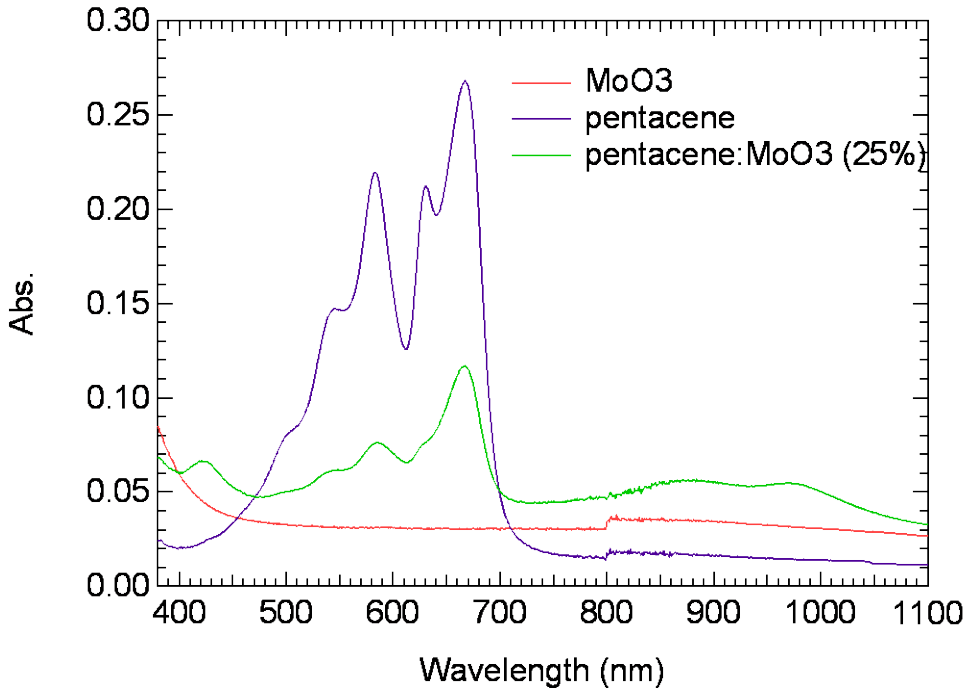

Figure 3.8 Absorption spectra of pentacene (100 nm), MoO3 (50 nm), and pentacene:MoO3 mixed layer (50 nm).

The absorption spectrum of pentacene shows absorption peak from 400 nm to 750 nm with main peak at 670 nm. The absorption spectrum of MoO_3 shows no absorption peak above 500 nm. However, the absorption spectrum of pentacene:MoO_3 mixed layer shows new absorption peak at 850 and 970 nm, which cannot be seen in the absorption spectra of pentacene and MoO_3. It is considered that these new absorption peaks are originated from charge-transfer complex between an organic material and dopant.[49, 50] Therefore, it indicates the formation of charge-transfer complex between pentacene and MoO_3, leading to *p*-doping of the pentacene.

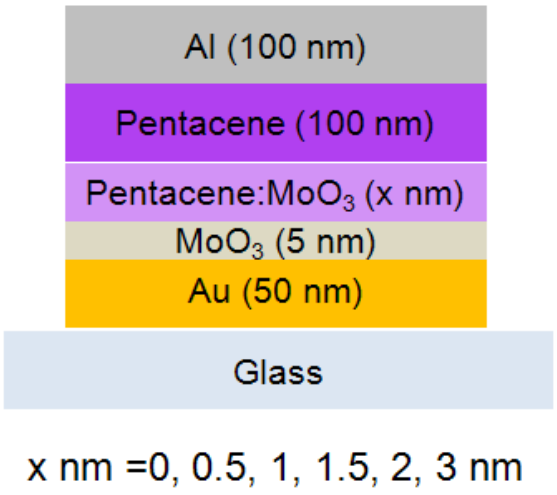

Figure 3.9 Device structure of pentacene diodes with different pentacene:MoO_3 mixed layer thickness.

By inserting the pentacene:MoO_3 mixed layer between MoO_3 and pentacene, pentacene diode with different mixed layer thicknesses were fabricated. The device structure of pentacene diodes is shown in Figure 3.9. The thickness of 0, 0.5, 1, 1.5, 2, and 3 nm was selected for pentacene:MoO_3 mixed layer. *I*–*V* structure of

pentacene diode with different pentacene:MoO_3 mixed layer thickness is shown in Figure 3.10. For the pentacene diodes with the mixed layer thickness of 0.5, 1, and 1.5 nm show shunt, that is, they not show any rectifying characteristics. Unlike our expectation, there is neither reduction of turn-on voltage nor increase of forward-bias current. In addition, by adding the mixed layer the reverse-bias leakage current is extremely increased. To study why this effect occurs, the AFM image of the mixed layer is obtained.

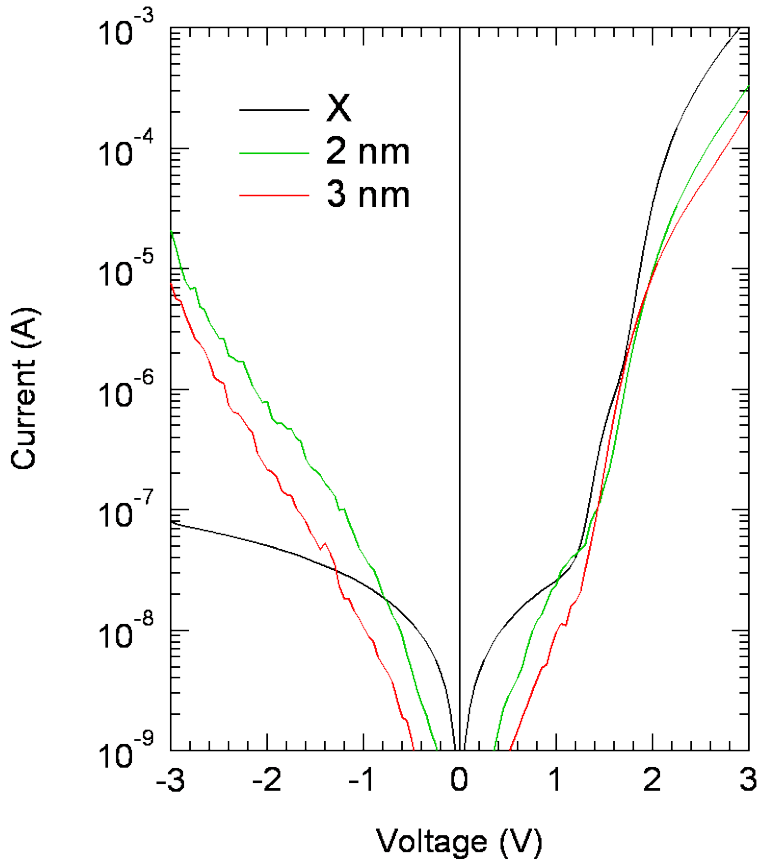

Figure 3.10 *I–V* characteristics of pentacene diodes with pentacene:MoO_3 mixed layer. The thicknesses of the mixed layer are 0 nm (black), 2 nm (green), and 3 nm (red), respectively.

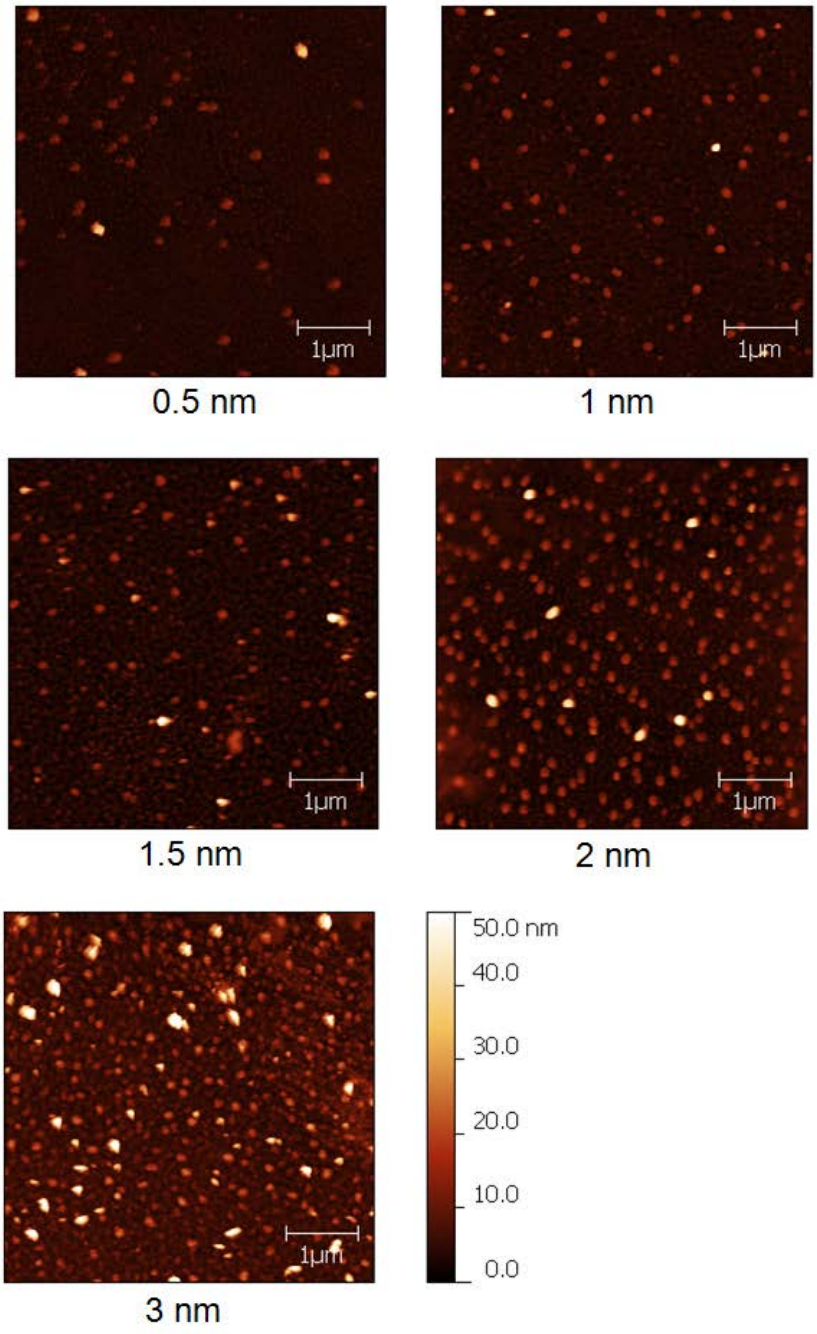

Figure 3.11AFM images of different thickness of pentacene:MoO_3 mixed layer on the MoO_3 layer.

Figure 3.11 shows the AFM images of different thickness of pentacene:MoO_3 mixed layer on the MoO_3 layer. As the thickness of the mixed layer increases, the spikes in the AFM images, indicating that the pentacene:MoO_3 grows island structure rather than layer. In addition, the grain height of pentacene:MoO_3 is greater than 50 nm. This high roughness would affect the grain size of pentacene. Figure 3.12 shows the AFM images of pentacene on MoO_3 and the mixed layer. The root mean square roughness (R_q) of pentacene on MoO3 is 3.1 nm but the R_q of pentacene on the mixed layer is 7.7 nm. Moreover, the peak-to-vally roughness (R_{p2v}) of pentacene on MoO_3 is 26 nm but the R_{p2v} of pentacene on the mixed layer is 62.8 nm. Due to this high R_q and R_{p2v} values, the top and bottom electrode in the pentacene diode on the mixed layer easily contacts through pentacene grain boundary, resulted in shunt. Furthermore, assuming that the mixed layer reduces the turn-on voltage of the pentacene diode, pentacene:MoO_3 islands cannot effectively reduce the turn-on voltage.

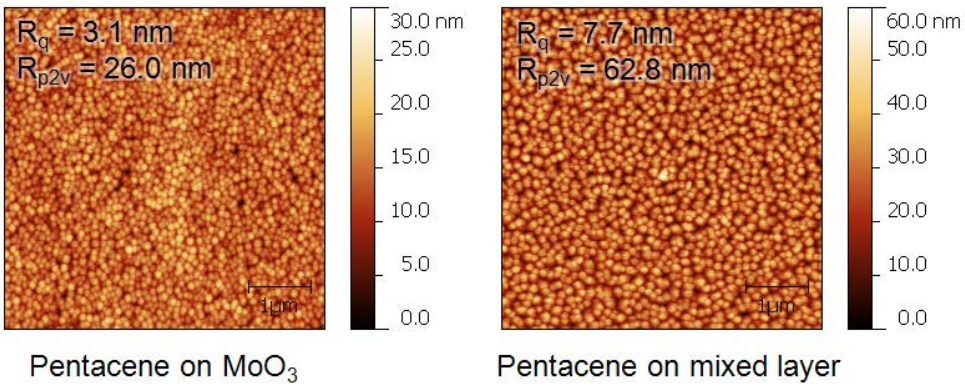

Figure 3.12 The AFM images of pentacene on (a) MoO_3 and (b) pentacene:MoO_3 mixed layer.

3.2.3 Impedance Spectroscopy

The impedance spectra of the pentacene diodes before and after electrical annealing were measured in order to analyze the interface and bulk characteristics of the diodes. Impedances of the pentacene diodes are measured from 20 Hz to 50 MHz. Fig. 5 shows Cole–Cole plots for the pentacene diodes before electrical annealing at the forward bias of 3.0 V and after electrical annealing at the forward bias of 1.4 V. Because the current of the pentacene diode is increased after electrical annealing, the voltages at the similar current region were chosen for comparison. The shape of the Cole-Cole plot for the pentacene diode before electrical annealing appears two distinguished semicircles. However, the shape of the Cole-Cole plot for the pentacene diode after electrical annealing shows the overlapped semicircles with a linear line at the low-frequency region.

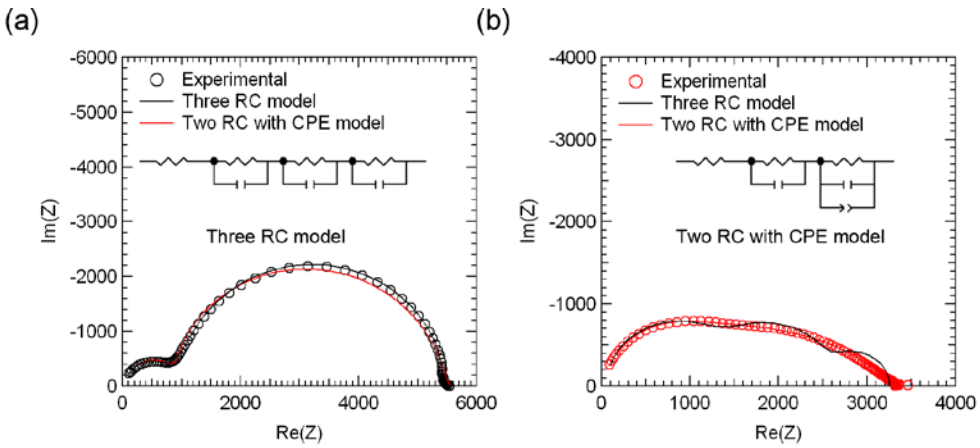

Figure 3.13 The Cole–Cole plots for the pentacene diodes (a) before electrical annealing at the forward bias of 3.0 V and (b) after electrical annealing at the forward bias of 1.4 V. The black solid line is the fitting line by the three-RC model and the red solid line is the fitting line by the two-RC with CPE model as shown in the inset.

The diode before electrical annealing can be modeled with the equivalent circuit consisting of one series resistance and three different RC components as shown in the inset of Figure 3.13(a); (i) the Au/MoO_3/pentacene interface, (ii) the pentacene bulk layer, and (iii) the pentacene/Al Schottky junction. Even though two distinguished circles of the Cole-Cole plot can be assigned as two RC components, the adjacent interface between two circles is not clearly separated, which implies the possibility of a small circle between two circles. Moreover, the fitting line using three RC components shows better accuracy than two RC components, we assigned Au/MoO_3/pentacene interface to one RC component even though that interface has small potential energy barrier.[51] The parameters are extracted using an iteration tool. First of all, the pentacene bulk layer is thicker than the others, resulted in smallest capacitance so the R2-C2 component corresponds to the pentacene bulk layer. Secondly, Schottky junction forms depletion region, leading to a large resistance and highest RC constant so the R3-C3 component corresponds to the pentacene/Al Schottky junction. Finally, the resistance at the Au/MoO_3/pentacene interface is small due to small energy barrier so the R1-C1 component corresponds to the Au/MoO_3/pentacene layer. These assignments are consistent with a previously report.[51] The extracted parameter values are summarized in Table 3.2.

Table 3.2 Extracted parameters of the three-RC model for the pentacene diode before electrical annealing.

Before EA	*Value*	*Error (%)*	*Assignment*
R	47.5	3.5	Contact resistance
R1	2.65×10^{2}	3.32	Au/MoO_3/pentacene
C1	2.96×10^{-10}	7.95	Au/MoO_3/pentacene
R2	8.30×10^{2}	1.04	Bulk
C2	1.43×10^{-11}	0.55	Bulk
R3	8.78×10^{3}	0.16	Pen/Al Schottky junction
C3	2.30×10^{-10}	0.42	Pen/Al Schottky junction

Table 3.3 Extracted parameters of the two-RC with CPE model for the pentacene diode after electrical annealing.

After EA	*Value*	*Error (%)*	*Assignment*
R	30.0	5.91	Contact resistance
R4	8.22×10^{2}	1.69	Bulk
C4	1.94×10^{-11}	2.08	Bulk
R5	2.47×10^{3}	0.64	Pen/Al Schottky junction
C5	1.91×10^{-11}	5.12	Pen/Al Schottky junction
CPE-Q	1.68×10^{-7}	1.04	Pen/Al Schottky junction
CPE-n	0.5 (fixed)	-	Pen/Al Schottky junction

After electrical annealing, the shape of the Col-Cole plot for the pentacene diode is significantly changed. The fitting line of three-RC model, shown in the black line of Fig. 5(b), cannot match well with experimental data. In addition, the linear shape appears at the low frequency region, which cannot be fitted using RC components. To solve this problem, two-RC component with CPE is used as shown in the inset of Fig. 5(b). The CPE can be expressed by

$$Z_{CPE} = \frac{1}{Q(j\omega)^n}. \tag{3.3}$$

Where the j^2 = -1, ω is the angular frequency, and Q and n are the frequency independent parameters.[52] The n value is fixed to be 0.5 that will be discussed later. The fitting line of two-RC with CPE model, shown in the red line of Figure 3.13(b), fitted well with experimental data. In addition, when we fitted three-RC with CPE model, one RC component exhibits large error (> 30 %), indicating that two-RC model is more reliable than three-RC model. The extracted parameters are summarized in Table 3.3. The RC-component of the bulk region originates from the geometrical characteristics of the diode so it is mostly determined by the thickness of active layer. Even though the interfaces at the diode may be changed after electrical annealing, the thickness of the active layer of the diode cannot be significantly changed, indicating that the capacitance in the bulk region of the diode (C1) should be similar. The R4-C4 component of the diode after electrical annealing is similar to R1-C1 so R4-C4 can be assigned to the bulk region of the diode. Moreover, the improved current after electrical annealing indicates the reduced resistance. The R5 is much higher than R2 and smaller than R3 so the R5-C5-CPE component can be assigned to the pentacene/Al junction.

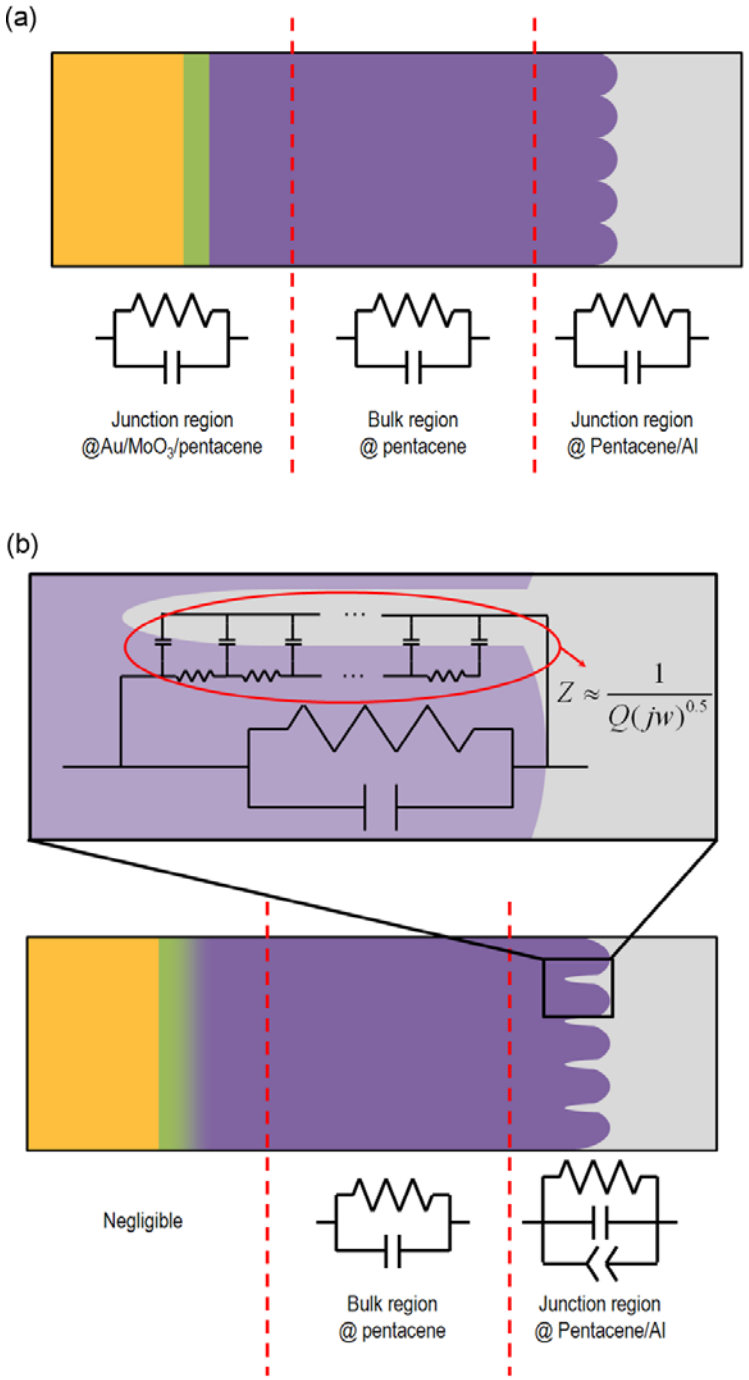

Figure 3.14 Proposed schematics of the pentacene diode (a) before and (b) after electrical annealing.

Figure 3.14(a) and (b) depict the proposed mechanism of electrical annealing based on *I-V* characteristics, ToF-SIMS, and Impedance spectra. After electrical annealing, two major changes are observed in the impedance spectra: The RC-component at the Au/MoO_3/pentacene interface disappears and CPE at the pentacene/Al interface appears. Firstly, the disappeared RC-component at Au/MoO_3/pentacene interface indicates that small energy barrier at this interface is reduced to a negligible level. The reduced turn-on voltage in the *I-V* characteristics also assists a reduced injection barrier at this interface. From the ToF-SIMS data, MoO_3 is diffused into the pentacene layer, creating the pentacene:MoO_3 mixed layer. Therefore, we conclude that this mixed layer effectively increases charge injection by reducing small potential barrier which causes the turn-on voltage of *I-V* characteristics and the RC-component at Au/MoO_3/pentacene interface of impedance spectra. Therefore, we conclude that the device performance of the pentacene diode is improved by electrical annealing due to the creation of the pentacene:MoO_3 mixed layer. Note that this uniform and thin pentacene:MoO_3 mixed layer cannot be formed by thermal evaporation. When the thin mixed layer was intentionally inserted between MoO_3 and pentacene using thermal evaporation, the mixed layer formed islands rather than uniform layer. Moreover, this island structure affects the growth of pentacene, leading to the increase of pentacene roughness, resulting in high reverse-bias leakage current of the diode. Furthermore, the thin mixed layer which has gradual change in pentacene:MoO_3 composition ratio is hard to fabricate by thermal evaporation. Therefore, electrical annealing is the best technique to form the uniform, thin, and gradual pentacene:MoO_3 mixed layer.

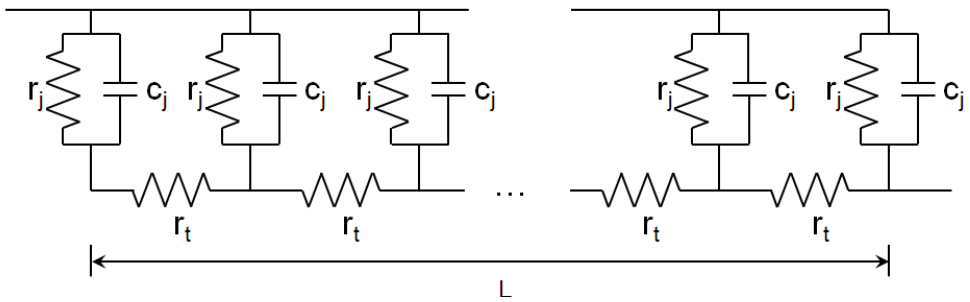

Figure 3.15 The equivalent circuit of finite-length transmission line model. The r_t, r_j, c_j, L is the distributed transport resistance, distributed junction resistance, distributed junction capacitance, and total length, respectively

Secondly, the CPE at pentacene/Al appears after electrical annealing, indicating that something is changed at this interface. The CPE used to explain the diffusion-recombination model of electrochemical systems. However, the Schottky diode exhibit very small minority carrier so diffusion and recombination current is typically negligible.[32] Instead of diffusion-recombination model, the CPE can also be appeared in real system that has non-homogeneity. Porous and rough electrode surfaces can lead to frequency dispersion of the interfacial impedance, which leads to CPE behavior.[53] Various equivalent circuit models of rough electrodes such as a transmission line, V-shape groove, branched transmission line, and fractal shape have been suggested to explain CPE behavior. Among them, the impedance of a finite-length transmission line, shown in Figure 3.15, can be expressed by[54]

$$Z_W = \sqrt{\frac{R_t R_j}{1 + j\omega R_j C_j}} \coth\left(\sqrt{R_t / R_j + j\omega R_t C_j}\right). \quad (3.4)$$

Where the R_t is the total transport resistance (r_t×L), R_j is the total junction resistance (r_j/L), and C_j is the total junction capacitance (c_j×L). If the R_j is close to

infinite and angular frequency is much higher than $1/R_jC_j$, Eq. (3.4) can be reduced to Eq. (3.3). Thus, we suggest that the CPE is attributed to creation of Al rod-like structures which act as finite transmission lines. ToF-SIMS depth profiles shows that some of Al is penetrated into pentacene layer. As mentioned before, the some spikes of Al at the pentacene grain boundary induce higher electric field, enabling the penetration of Al more easily. Therefore, the penetrated Al may create rod-like structures that can be modeled as a finite length transmission line as shown in Fig. Figure 3.14(b). In addition, when the forward-bias is applied to the pentacene diode after electrical annealing, the electric field perpendicular to the Al-rod surface is very small so the depletion region at the Al rod structure is not significantly shrunk even though the other depletion regions is shrunk. As a result, depletion regions which surround the Al-rod structures have high resistance so R_j can be ignored. In addition, due to the high R_j, R_jC_j can also exhibit high values which resulted in small $1/R_jC_j$. Therefore, the Al rod structure which is expressed by Eq. (3.4) can be considered as a CPE. Fortunately, CPE is parallel connection with RC-component so CPE effect will disappear as the frequency increases. Consequently, the frequency performance of the pentacene rectifier at the high frequency is not significantly affected by creation of CPE.

3.3 Summary

In summary, we investigated improved performance of pentacene diodes by electrical annealing. After electrical annealing, turn-on voltage of a pentacene diode in the rectifier is reduced from 1.25 V to 0.44 V and current of that is increased 4.4 times higher at 3 V without increase of reverse-bias leakage current. In addition, cutoff frequency of the pentacene rectifier is increased from 10.5 MHz to 85.7 MHz. The thermal annealing without electric field cannot affect the device performance, indicating that electric field plays an important role in electrical annealing process. Moreover, there is no hysteresis which indicates that interfacial trap states are small to negligible. From the ToF-SIMS and impedance spectra, we conclude that the improvement of electrical annealing is due to the diffusion of MoO_3 into pentacene layer, which increase charge injection. Al penetration into the pentacene layer was also observed but it cannot affect device performance at high frequency. We expected that this method can also be applied to organic photovoltaic devices (OPVs), organic light-emitting diodes (OLEDs), organic thin film transistors (OTFTs), quantum dots (QDs) devices, and so on, as well as the organic rectifier.

Chapter 4

High Performance Pentacene Diodes based on SAM-treated Gold

The SAM is one of the good candidates for tuning the work function of metals. It is very simple, robust, and large-area applicable. In addition, the tuning of work function is very important issue in the device engineering because the energy barrier at the interface is basically determined by the difference between metal and HOMO level of the organic materials. By tuning work function of the metal, charge injection can be controlled. For example, the diode which exhibit both high forward bias current density and small reverse bias leakage current can be fabricated by using SAM treatment on metals with opposite dipole moment molecules. For the p-type semiconductor, hole injection barrier of one interface is reduced and the other is increased by the permanent dipole moment of SAM molecules, leading to high forward current due to reduced barrier and low reverse current due to increased

barrier. For this reason, SAM have been widely used for reducing hole injection barrier in OTFTs,[24, 26, 55-57] OLEDs,[10, 21, 58] an OPVs.[22, 23]

In addition to tuning of work function by treating SAM on metals, the surface characteristic is changed due to the functional group of SAM molecules. Especially, the grain formation of pentacene is much affected by surface energy, which can be controlled by the functional group of SAM molecules. The hydrogen and fluorine group of SAM molecules lowers the surface energy, making the grain size of pentacene larger. In addition, hole traps induced by hydroxyl group in the surface can be effectively reduced by treating SAM. As a result, the mobility of pentacene on SAM-treated surface in OTFTs can be increased compared to that on pristine surface.[59-61]

Studies have shown that the growth and orientation of pentacene which deposited on gold is changed when it deposited on SAM-treated gold.[62, 63] the grain of pentacene on gold has rod-shape structure but that on *p*-terphenylmethanethiol-treated gold has dendritic shape, indicating that pentacene on gold grows horizontally but that on SAM-treated gold grows vertically. Moreover, XRD pattern of pentacene on gold show their peaks at (110), (022), (200) but that on SAM-treated gold show their peaks at (001), (002), and (003), indicating that pentacene molecules on gold exhibits lying-down orientation but that on SAM-treated gold exhibits standing-up orientation. This morphological difference will change electrical characteristics but this structure-property-performance relationship of pentacene along vertical direction still remains as a missing link. In this study, we investigated the structure-property-performance relationship of pentacene along vertical direction.

4.1 Effective Work Function of SAM-treated Gold

4.1.1 Photoelectron Spectrometer Measurement

To study the effect of work function shift due to dipole moment of SAM molecules, the photoelectron spectrometer are measured. Figure 4.1 shows the effective work function of gold, and SAM-treated gold. All emission yields show that two slope so the middle points of first slopes are selected as the work function. The work function of gold is measured to be 4.78 eV. Note that the work function of gold ranges from 4.7 to 5.1 eV depending on surface contamination.[64] The work function measurements are done under ambient condition so gold surface is exposed ambient air, enabling to be contaminated by oxygen and carbon based molecules. However, even though work function is lower than clean gold (5.3 – 5.4 eV), it can be compared relatively because all samples are treated in same conditions. The work function of TP-modified gold and PFBT-modified gold is measured to be 4.67 and 5.02 eV, respectively. PFBT molecules have negative dipole moment, increasing the effective work function of gold. Otherwise, TP molecules have positive dipole moment, decreasing effective work function of gold. The results indicate that PFBT-modified gold/pentacene interface is expected to lowest injection barrier because the HOMO level of pentacene is about 5.0 eV,

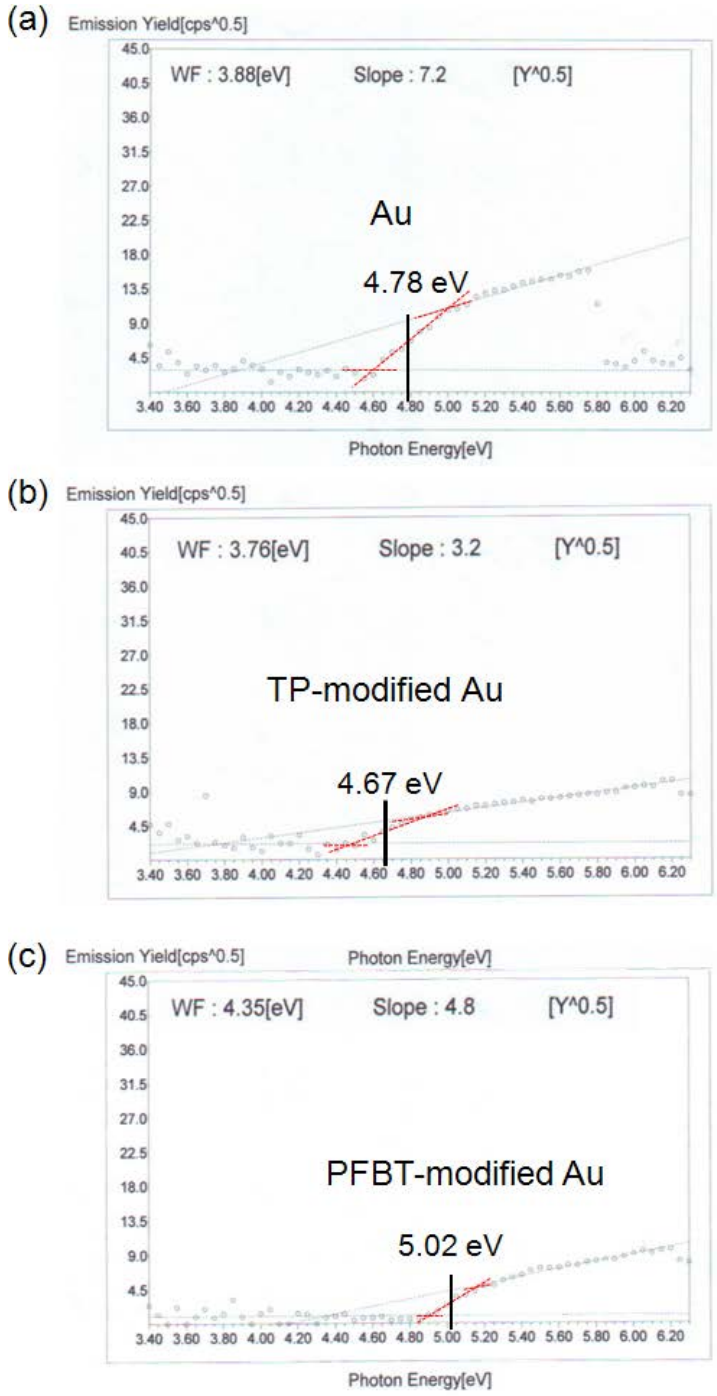

Figure 4.1 Effective work function of (a) gold, (b) TP-treated gold, and (c) PFBT treated gold using photoelectron spectroscopy.

4.2 Structural study of pentacene on SAM-treated gold

4.2.1 Morphological Study Using AFM

Thermally evaporated pentacene forms polycrystalline structure so the growth mode and structure of pentacene is affected by deposition condition, surface energy, and surface roughness. Especially, this structural difference can affect the electrical performance of the devices so it is important to know how the pentacene molecules grow on the surface. To observe the structure of the pentacene, the morphologies of pentacene on gold and surface-modified gold are measured by AFM. Figure 4.2 shows AFM images of pentacene monolayer (1.5 nm) on gold, TP-treated gold, and PFBT-treated gold. It can be observed that gold forms small nanodots. The pentacene on gold shows that pentacene molecules grow horizontaly, forming rod-like structure. In addition, pentacene on aggregates more than that on SAM-treated gold, leading to high roughness. On the other hands, pentacene on TP- and PFBT-treated gold follows roughness of gold and forms small islands-like structure. These structural differences are also observed in bulk pentacene molecules as shown in Figure 4.3. The pentacene films on TP- and PFBT-treated gold show circular patterns but the pentacene film on gold shows rod-like pattern, which corresponds to previously reports.[62, 63, 65] Due to the relatively high deposition rate, the structure of pentacene on gold seems to grains of rice rather than rods. The rms roughness of pentacene on gold, TP-treated gold, and PFBT-treated gold is 11, 7.47, and 5.63 nm, respectively. High roughness of pentacene on gold can attribute critical issues in the device such as high leakage current, high capacitance, and low yield due to shunt.

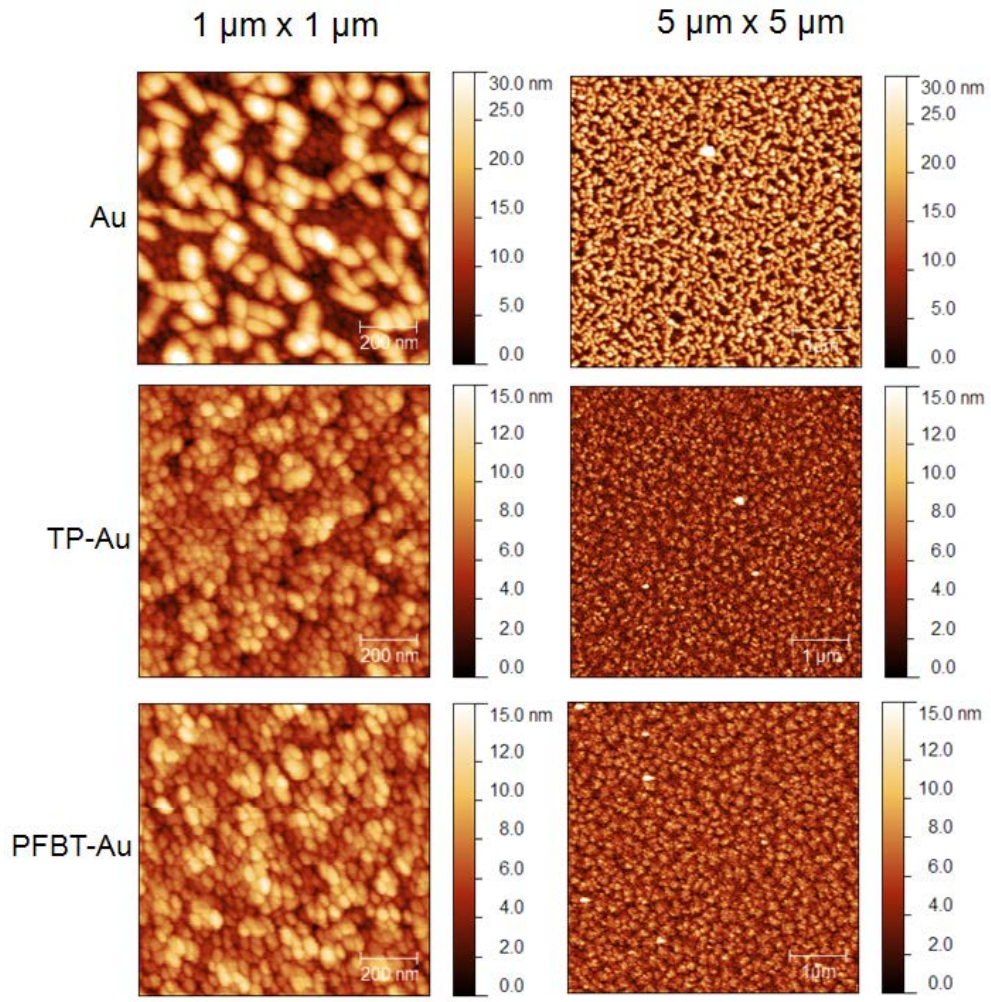

Figure 4.2 AFM images of pentacene monolayer (1.5 nm) on gold, TP-treated gold, and PFBT-treated gold.

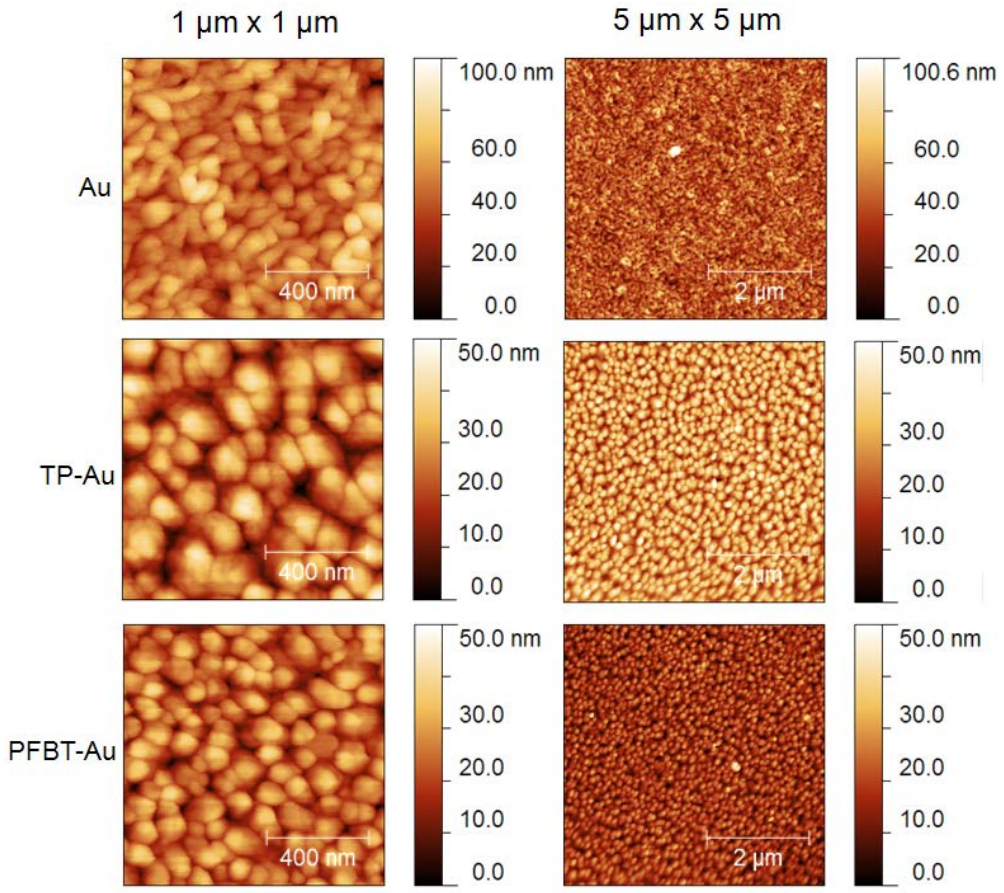

Figure 4.3 AFM images of bulk pentacene (90 nm) on gold, TP-treated gold, and PFBT-treated gold.

4.2.2 XRD Analysis

The pentacene films are analyzed by XRD as shown in Figure 4.4. The XRD patterns of 90-nm thick pentacene films on TP- and PFBT-treated gold show their peaks at 5.73° and 11.55° with corresponding interplanar d spacing of 15.4 Å, which can be assigned to be (001) and (002) plane of thin film phase, implying that pentacene molecules are standing-up on SAM-treated gold. Otherwise, The XRD patterns of the pentacene film on pristine gold show small peaks at 19.25°, 24.03°, 28.21° with corresponding interplanar d spacing of 4.6, 3.65, and 3.15 Å, which can be assigned to be (110), (022) and (-201), implying that pentacene molecules are lying-down on pristine gold.

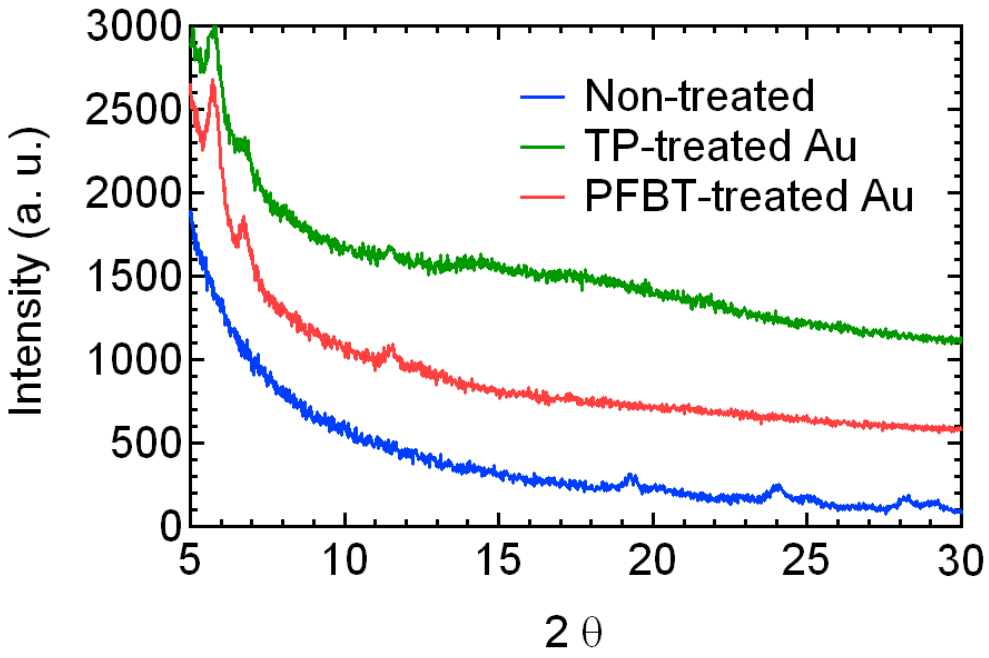

Figure 4.4 X-ray diffraction patterns of pentacene on gold, TP-treated gold, and PFBT-treated gold.

4.2.3 DFT Simulations of Single Pentacene Molecule for Raman Spectroscopy

To investigate the structure properties of the pentacene on SAM-treated gold, Raman spectroscopy is measured. To match the Raman peaks to vibrational states of the pentacene, density function theory (DFT) simulation is performed. Figure 4.5 shows the calculated Raman peaks based on DFT simulation of a pentacene molecule. The major vibrational states occur in the range of 1100–1700 cm^{-1}. From the DFT simulation, vibrational modes of C-H ends, C-H sides, C-C along the short axis, and C-C along the long axis are assigned to be 1150, 1170, 1350–1400, and 1590 cm^{-1}. Calculated Raman peaks based on the DFT simulation and their corresponding vibrational modes are summarized in Table 4.1.

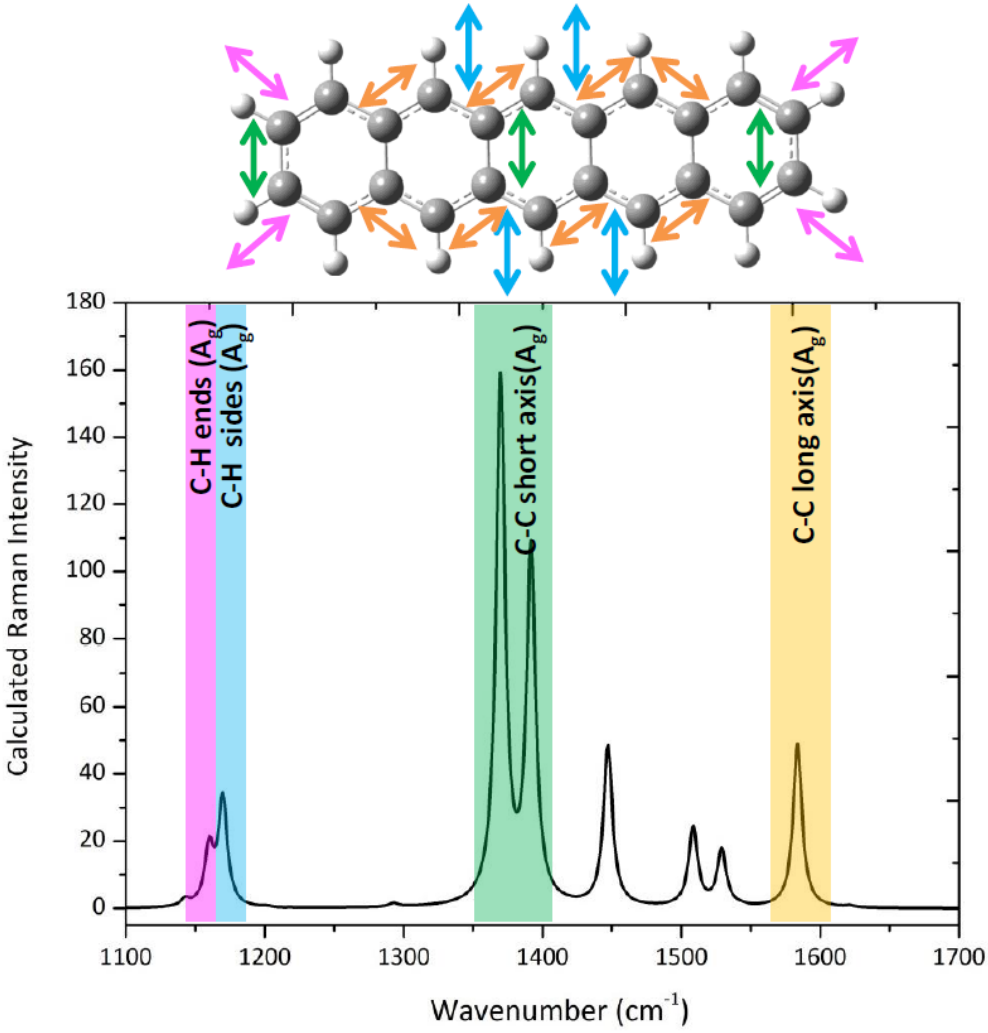

Figure 4.5 Calculated Raman peaks based on DFT simulation of a pentacene molecule.

Table 4.1 Caculated Raman peaks based on the DFT simulation and their corresponding vibrational modes.

B 6-31 G (d,p) DFT	Scaled = * 0.9611	± 0.02	Vibrational Mode
1190	1143.709	23.8	C-H ends (A_g)
1207	1160.048	24.14	C-H sides (A_g)
1217	1169.659	24.34	C-H sides (A_g)
1425	1369.568	28.5	C-C short axis stretch (centre of molecule)
1448	1391.673	28.96	C-C short axis stretch
1506	1447.417	30.12	C-H rocking
1570	1508.927	31.4	C-C short coupled to C-C long
1591	1529.11	31.82	C-C short coupled to C-C long
1648	1583.893	32.96	C-C long (B_{3g})

4.2.4 Raman Spectra of Pentacene on SAM-treated Gold

Five wavelengths of laser are used to measure Raman spectra: 457, 488, 514, 633, and 785 nm. Raman spectra of 75-nm thick pentacene on gold, TP-treated gold, and PFBT-treated gold with various wavelengths are depicted in Figure 4.6. The pentacene absorbs visible light in the range from 400 nm to 700nm and has main peaks at 570, 630, and 670 nm; thus, non-resonance Raman spectra can be observed by using wavelength of 785 nm. All the Raman spectra show similar peaks with DFT simulation and have main peak at 1370 cm^{-1}, the C-C vibration mode along long axis, Using different laser excitations can selectively excite different modes in pentacene molecules. Long-axis stretch modes are probed with high energy excitation under 514 nm. Long-axis stretch is particularly enhanced in pentacene films on pristine gold. For the wavelength of 633 nm, all A_g modes, short axis, increase due to a surface enhanced Raman effects of gold. Whereas, B_{3g} modes, long axis, do not increase. The laser beam is focused on the samples at normal incidence. Because vibrational modes parallel to electric field of the laser are enhanced, C-C long axis vibration is enhanced if the pentacene molecules lie down on gold. On the other hands, C-C short axis vibration is enhanced if the pentacene molecules stand up. Therefore, C-C short axis/C-C long axis ratio can be used as a tool to probe molecular orientation. Figure 4.7(a) shows Raman spectra, excited by 785 nm laser, of the 100-nm thick pentacene films on gold, TP-treated gold, and PFBT-treated gold, respectively. The results show that all peaks except 1600 cm^{-1}, C-C long axis vibration mode, exhibit similar intensity. As mentioned before, C-C long axis vibration mode is enhanced when the pentacene molecules exhibit lying-flat orientation. Therefore, the results show that SAM encourages molecules to stands up perpendicular to the gold surface.

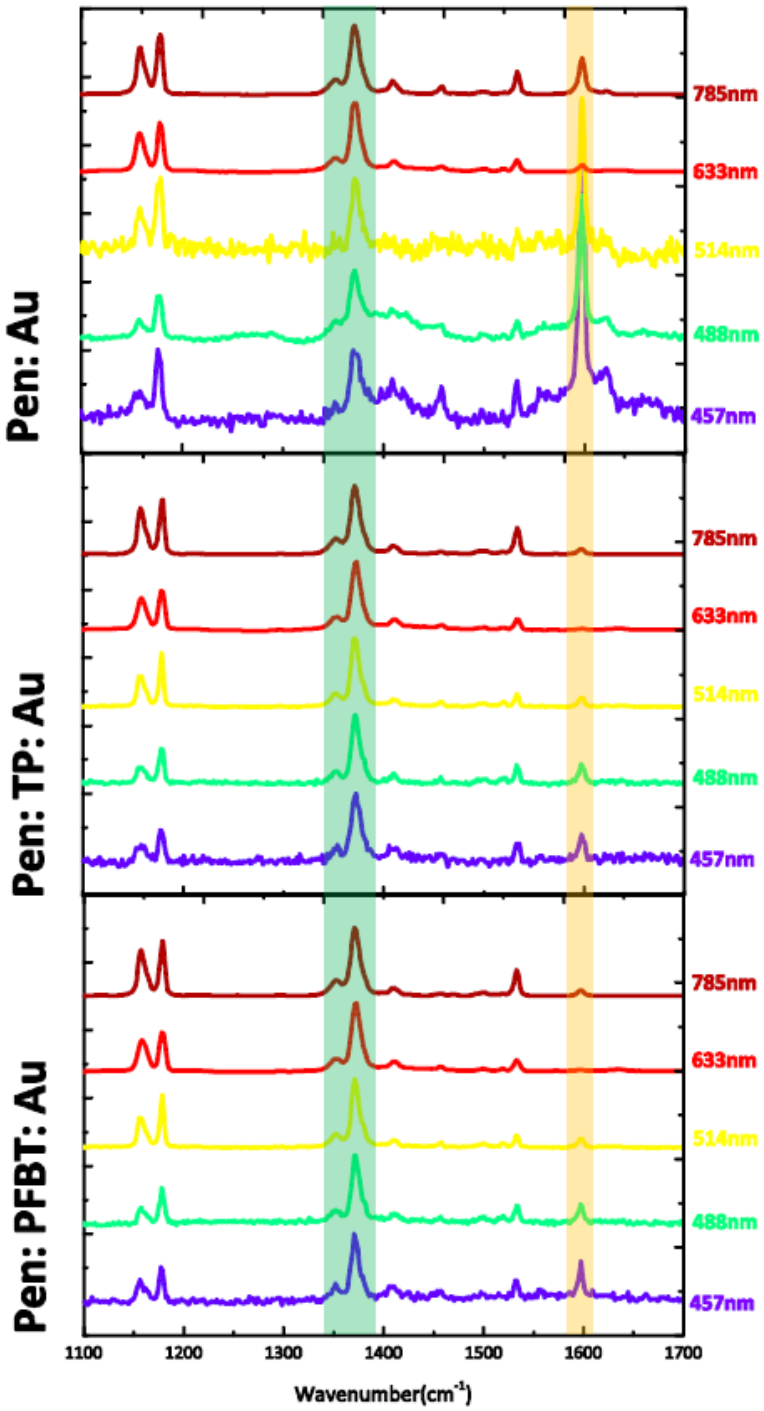

Figure 4.6 Measured Raman spectra of 75-nm thick pentacene on gold, TP-treated gold, and PFBT treated gold with various wavelengths.

For further study, the orientation of pentacene molecules with different thicknesses is probed by resonant Raman analysis. Wavelength of 514 nm is used for Incidence laser beam. Figure 4.7(b) shows the C-C short/long ratio of the pentacene films on gold, TP-treated gold, and PFBT-treated gold as function of pentacene film thicknesses. If the C-C short/long ratio is high, the pentacene molecules are standing-up orientation and the ratio is low, the pentacene molecules are lying-down orientation. The results show that C-C short/long ratio is lowest for the pentacene film on pristine gold and does not vary with film thickness, which means that molecules are predominantly lying flat independent of film thickness. However, for the pentacene film on PFBT-treated gold, C-C short/long ratio is largest at 10 nm films and decreases with increasing film thickness, indicating that molecules are standing up on the gold surface and molecules close to the gold substrate interface are standing more upright than those further away. Moreover, for the pentacene film on TP-treated gold, C-C short/long ratio is smallest at 10 nm films and increases with increasing film thickness, indicating that molecules far from the substrate interface are standing more upright than those at the substrate interface. For the thick films, C-C short/long ratio is similar for both pentacene films on TP- and PFBT-treated gold.

Previous studies already reported that the pentacene forms thin-film phase first tens of layers, and changes to bulk phase as thickness increases. The tilt angle of pentacene molecules which has bulk phase is higher than that which has thin-film phase. Therefore, the Raman signals can be considered that pentacene molecules on PFBT-treated gold firstly forms thin-film phase and changes to bulk phase. Moreover, the pentacene on TP-treated gold becomes similar value as film thickness increases, indicating that pentacene on TP-treated gold forms as film thickness higher than 50 nm. For the thin pentacene film on TP-treated gold, it seems that

SAM is partially treated on gold; thus, some of pentacene molecules on gold lie down and the others on TP-treated gold stand up. The proposed schematics of pentacene molecular orientation depending on SAM treatment on gold are depicted in Figure 4.8.

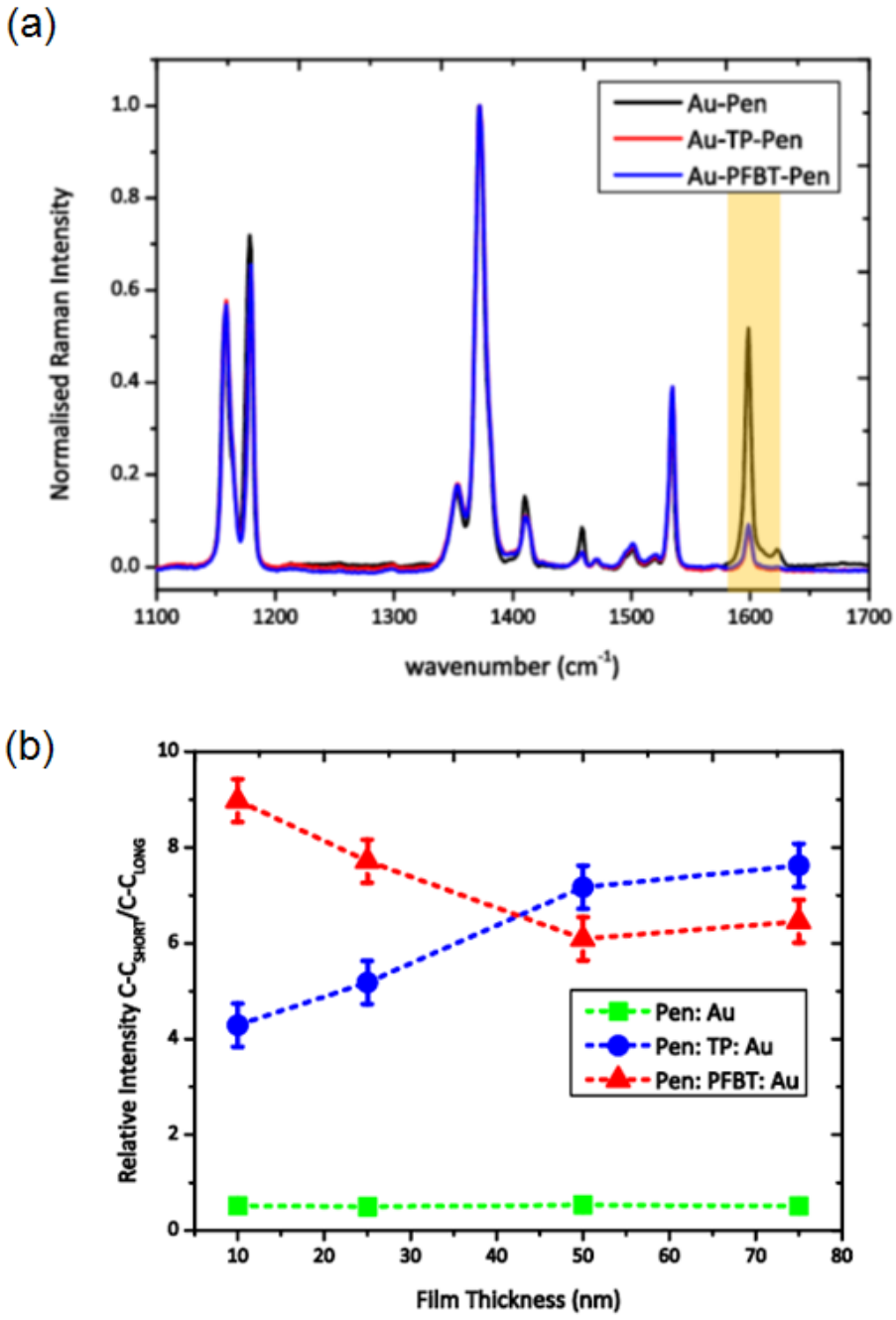

Figure 4.7 (a) Raman spectra, excited by 785 nm, of 100-nm thick pentacene films on gold, TP-treated gold, and PFBT-treated gold, respectively. (b) C-C short/long ratio of pentacene films on gold, TP-treated gold, and PFBT-treated gold as function of film thicknesses.

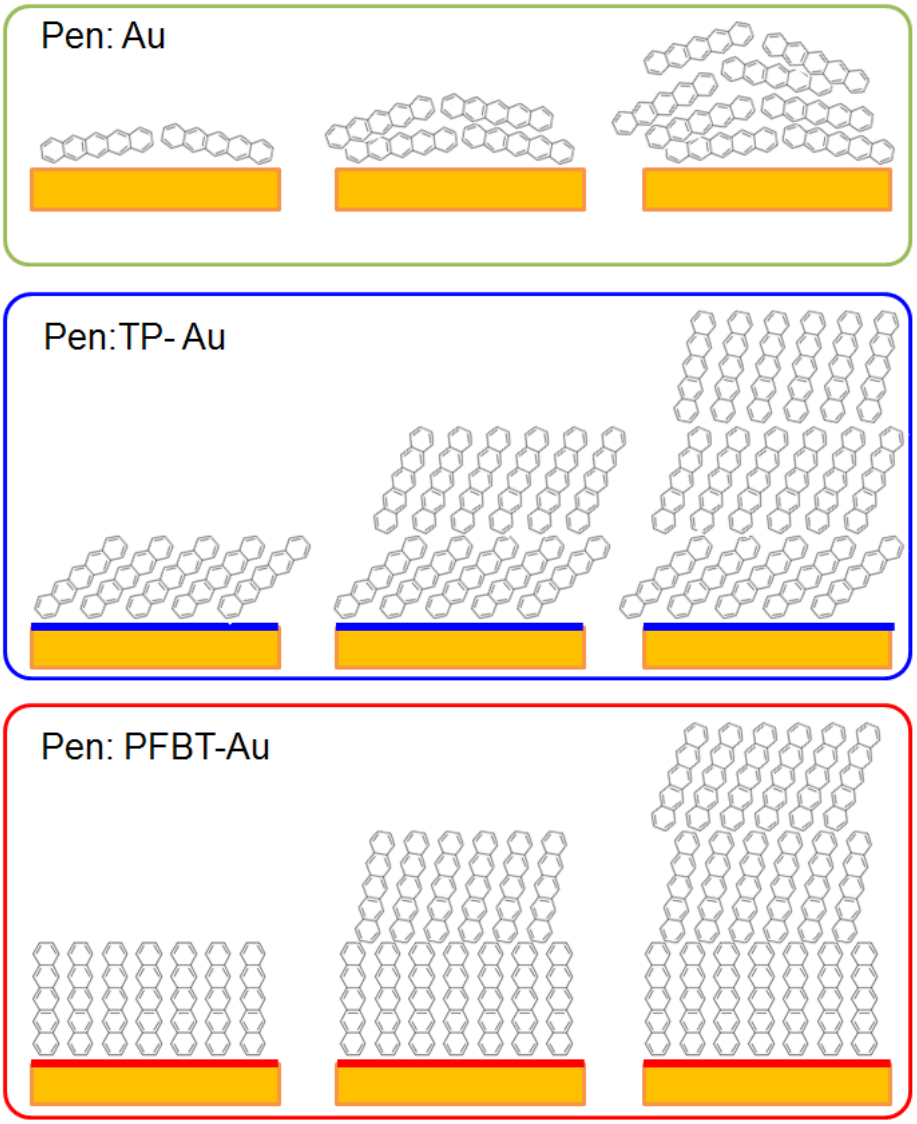

Figure 4.8 The proposed schematics of pentacene molecular orientation depending on SAM treatment on gold.

4.2.5 Mobility of Pentacene on SAM-treated Gold Extracted by SCLC

From the AFM, XRD, and Raman analysis, one can be found that the pentacene on gold forms lying-down orientation and the pentacene on TP- and PFBT-treated gold forms standing-up orientation. Therefore, these structural differences of pentacene on SAM-treated gold could change the electrical property of the diode. To investigate vertical carrier mobility of pentacene depending on molecular orientation, hole-only devices (HODs), which have a structure of Au (50nm) / SAM / pentacene (90nm) / MoO_3 (10nm) / Al (100 nm), were fabricated as shown in Figure 4.9(a). At the high voltage region, current density of HODs follows quadratic function, which is expressed by SCLC equation as shown in Figure 4.9(b). The dielectric constant of pentacene is used to be 3.3, obtained from capacitance of pentacene diode assuming parallel-plate geometry as presented in Figure 4.10, which is a similar value with a previous report.[66] From this equation, mobility of pentacene on gold, TP-modified gold, and PFBT-modified gold are calculated to be 6.82×10^{-4}, 6.46×10^{-3}, and 1.62×10^{-2} $cm^2V^{-1}s^{-1}$, respectively.

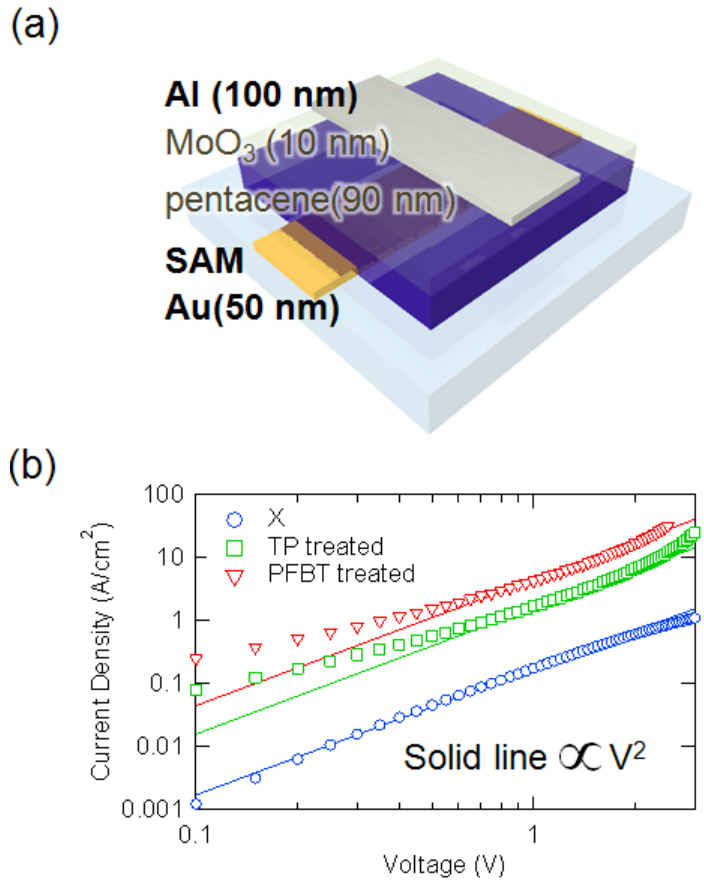

Figure 4.9 (a) The structure of pentacene holy-only devices with surface-modified gold. (b) *J–V* characteristics of pentacene hole-only devices with surface-modified gold. Hole is injected from aluminum to pentacene. At the high voltage region, three devices follow quadratic function, which is shown in solid lines. Assuming the pentacene/MoO_3/Al contact is ohmic, the mobility can be calculated using space-charge-limited current equation.

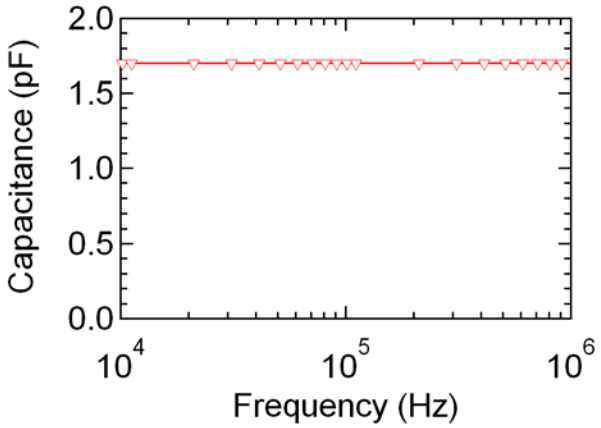

Figure 4.10 Capacitance of a pentacene diode with PFBT-modified gold measured by HP4192A with oscillator level of 50 mV at 0 V.

4.2.6 Mobility of Pentacene on SAM-treated Gold Extracted by Photo-CELIV

The mobility extracted by SCLC can be underestimated due to limited injection. To confirm hole mobility extracted by SCLC, photo-CELIV was measured. Figure 4.11 presents the photo-CELIV signals of the pentacene diodes with SAM-treated gold. The structure of the samples are Au (50 nm) / SAM / pentacene (400 nm) / Al (15 nm). 580-nm wavelength Nd:YAG laser pulse is irradiated toward a thin Al cathode for generating free carriers. For the pentacene on pristine gold shows clear CELIV peaks and the peak position shift toward left side as electric field increases, indicating that mobility could increase as electric field increases. From the photo-CELIV signal, the extracted mobility of pentacene on gold as function of electric field is shown in Figure 4.11(d). The mobility of pentacene on gold increases as electric field increases and it is extracted to be 7.11×10^{-4} $cm^2V^{-1}s^{-1}$ at 2.95×10^4 V/cm, which is the similar value with the mobility extracted by SCLC. Note that the mobility in the pentacene diode can be higher than measured values because this electric field is lower than operation electric field of the pentacene rectifier. There are no photo-CELIV peaks for the pentacene on SAM-treated gold, implying that the mobility of pentacene on SAM-treated gold is too fast to detect.

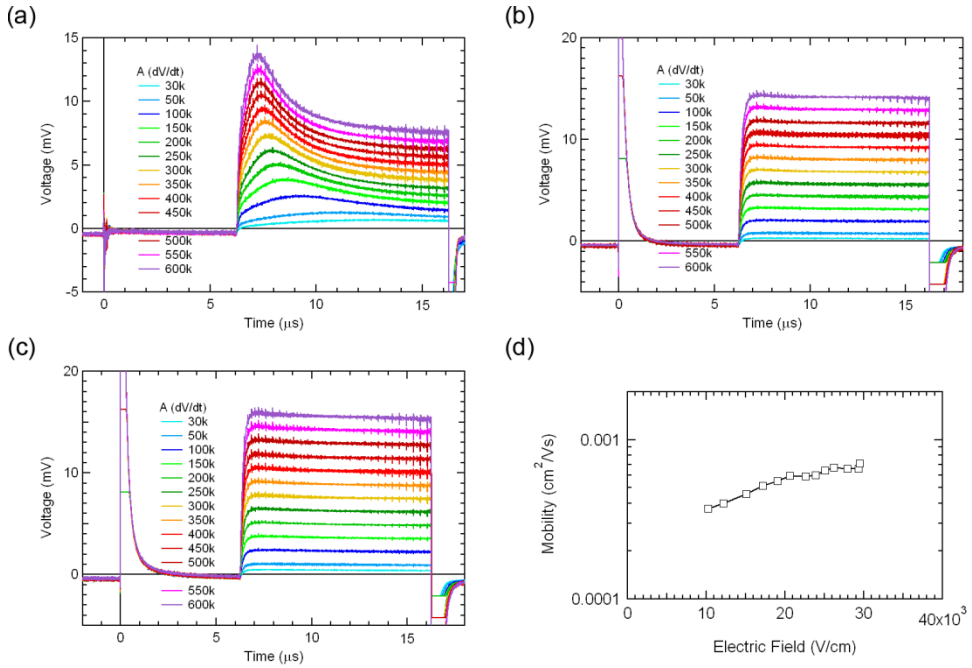

Figure 4.11 Photo-CELIV signals of the pentacene diodes with surface modified gold. The structure of the samples are Au(50 nm)/SAM/pentacene(400nm)/Al(15nm). 580-nm wavelength Nd:YAG laser pulse is irradiated toward a thin Al cathode for generating free carriers. (a) The photo-CELIV signal of the pentacene diode with pristine gold. (b) The photo-CELIV signal of the pentacene diode with PFBT-treated gold. (c) The photo-CELIV signal of the pentacene diode with TP-treated gold. (d) The mobility of pentacene on pristine gold as function of electric filed extracted by photo-CELIV signals.

4.2.7 SEM Images of Pentacene on SAM-treated Gold

To investigate the plain and vertical morphology of the pentacene molecules on SAM-treated gold, the SEM images are measured. Figure 4.12 shows the plain SEM images of 100-nm thick pentacene on gold, TP-treated gold, and PFBT-treated gold. The morphology of pentacene is completely different between pentacene on gold and that on SAM-treated gold. In addition, the morphology of pentacene on TP-treated gold is similar with that on PFBT-treated gold. The pentacene on gold grows laterally and forms interwoven structure which seems to be entangled, less dense, and disordered. Whereas, pentacene on gold grows vertically and forms circular structure which seems to be dense and ordered. This tendency can also be seen in the vertical direction. Figure 4.13 presents the vertical SEM images of 100-nm thick pentacene on pristine gold, TP-treated gold, and PFBT-treated gold. Pentacene on gold exhibits the entangled and disordered structure whereas pentacene on SAM-treated gold exhibits dense and ordered structure.

The previous chapters show that vertical mobility of pentacene on gold and SAM-treated gold shows that the pentacene forming standing-up orientation exhibit higher vertical mobility than that forming lying-down orientation. Although the mobility of single crystalline pentacene along the *ab* axis is known to have a higher value than *c* axis, thermally evaporated pentacene forms a polycrystalline thin film, indicating that the carrier transport can be limited by transport between grain boundaries. The pentacene film on gold exhibits small XRD peaks, indicating that pentacene is almost randomly oriented. In addition, the pentacene on gold not exhibit perfect flat-lying orientation, but has tilt angle of about 30–45°, resulting in randomly oriented pentacene grains.[63, 67] This poor molecular ordering in case of

pentacene on gold can limit charge transport property, resulting that the mobility of the pentacene film on gold is smaller than that of on SAM-treated gold.

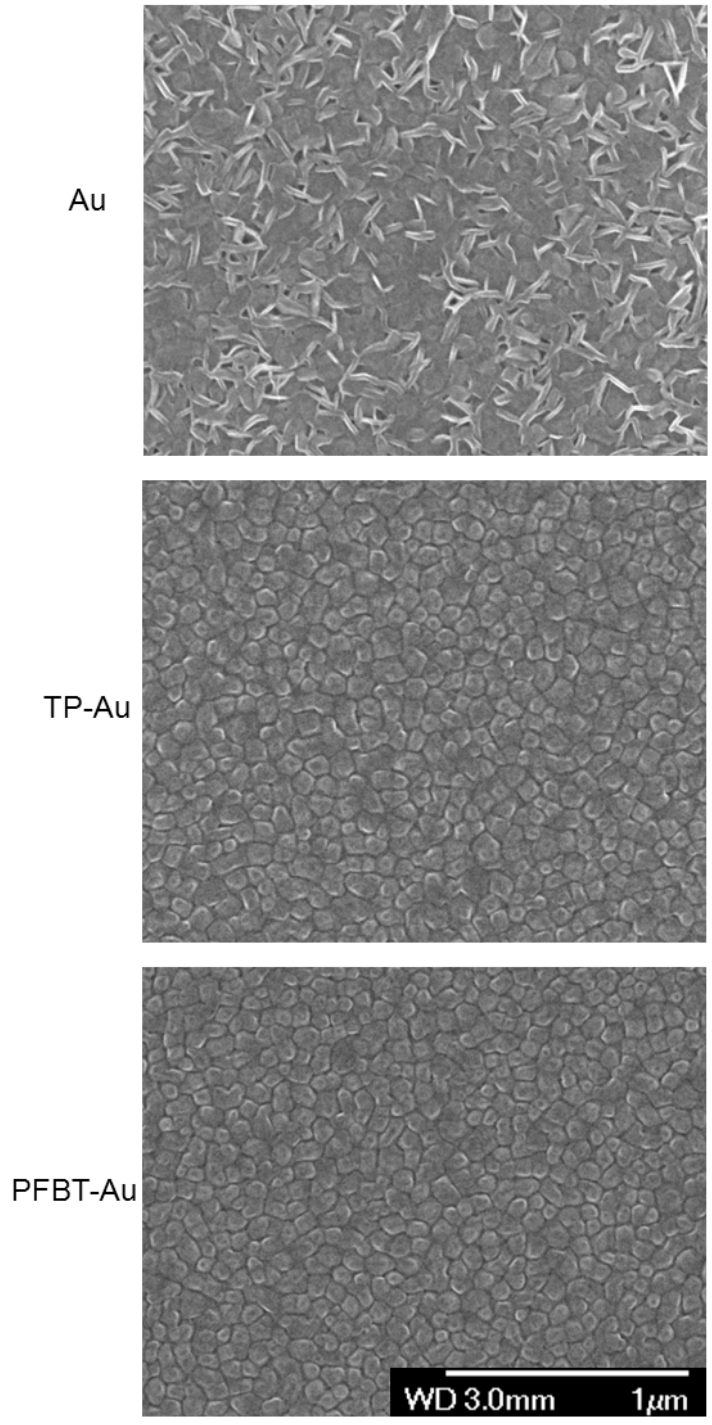

Figure 4.12 Plain SEM images of 100-nm thick pentacene on Au, TP-Au, and PFBT-Au. The scale bar indicates 1 μm.

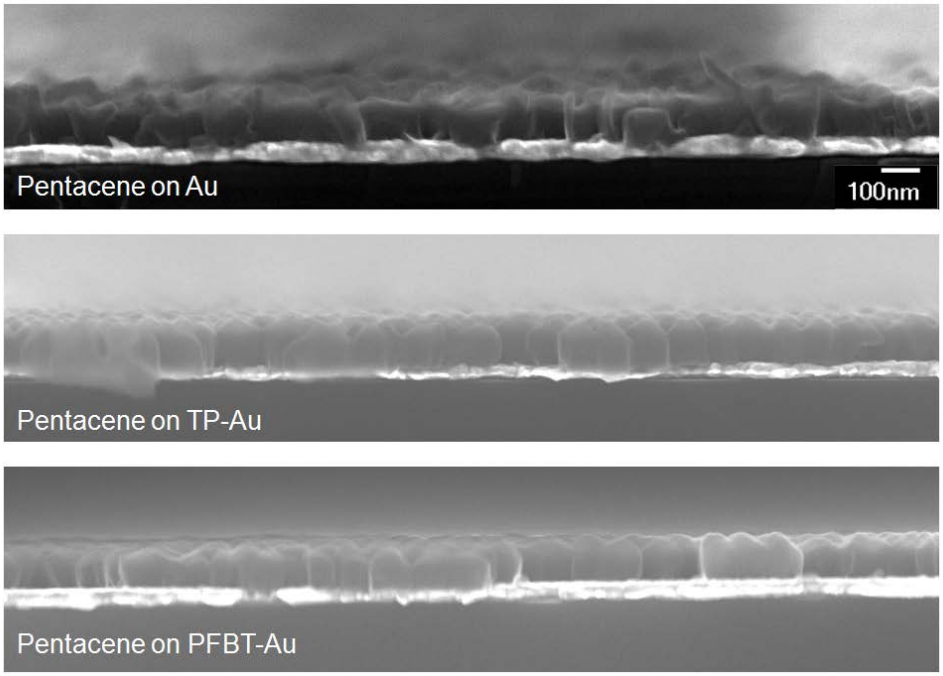

Figure 4.13 Vertical SEM images of 100-nm thick pentacene on pristine gold, TP-treated gold, and PFBT-treated gold. The scale bar indicates 100 nm.

4.3 Electrical Performance of Pentacene Diodes with SAM-treated Gold

4.3.1 *J–V* Characteristics of Pentacene Diodes with SAM-treated Gold

The $J-V$ characteristics of pentacene diodes with surface-modified gold are presented in Figure 4.13. The graph shows that onset voltages of diodes with PFBT-treated, TP-treated, and non-treated gold electrode are 0.1, 1.1, 1.1 V, respectively. The diode with PFBT-treated gold show much lower onset voltage than the others, indicating that that the injection barrier located at gold/SAM/pentacene is effectively reduced. Previous reports show that the dipole moment of PFBT is -1–2 D,[68, 69] enabling to reduce the injection barrier by 0.1 eV.[70] As a result, The forward-bias current density of the diode with PFBT-treated gold is much higher than that with non-treated gold and finally current density of 100 A/cm^2 is obtained at 3 V. In addition, the rectification ratio of the diode shown in inset of Figure 2 is founded to be 7.47 × 10^5 at 1 V, and 1.05 × 10^7 at 2.8 V, which are1–3 orders of magnitude higher than previously reported rectifying diodes.[71-73] Such higher rectification ratio is attributed to the small reverse-bias leakage current, which results in a large reverse-bias breakdown voltage (V_R). In this study, the V_R of the diode is measured to be 18 V as shown in Figure 4.14. In an ideal rectifier, maximum reverse-bias voltage applied to the diode is twice of maximum input voltage. Because a rectifier should supply sufficient power to circuits, high V_R of a rectifier can endure high input voltage, enabling to supply high power to the circuits. Moreover, high input voltage improves the frequency performance of a rectifier.[29]

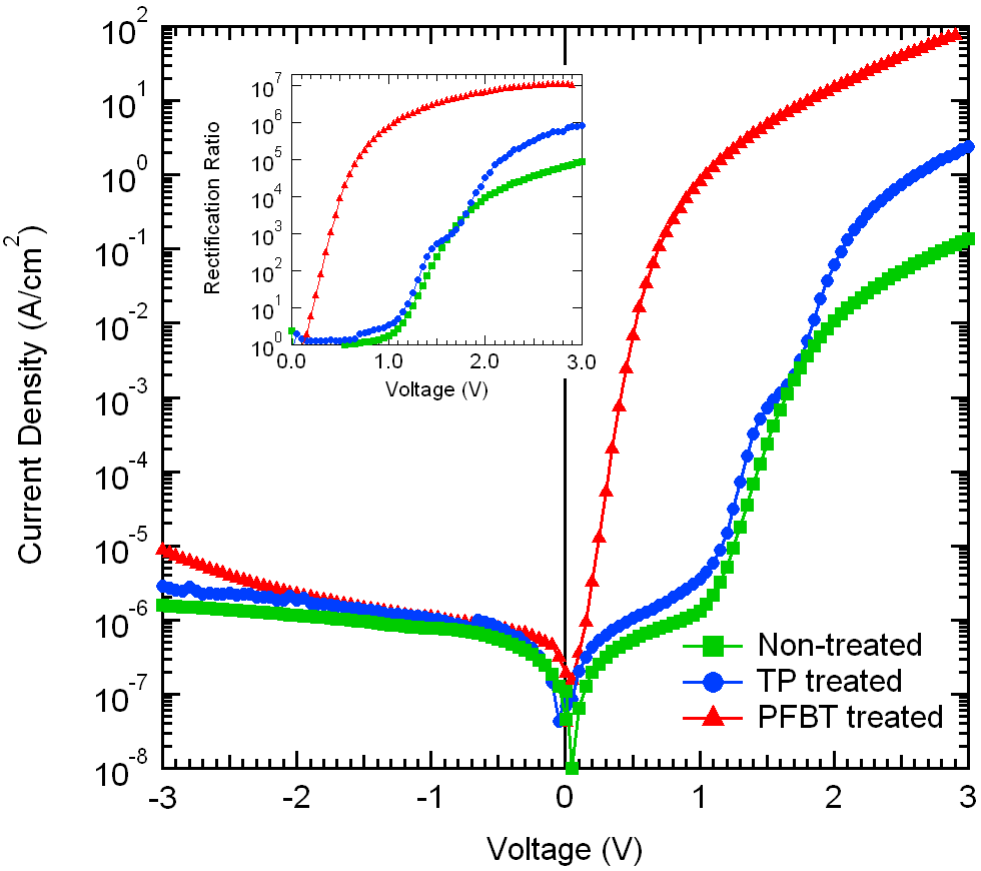

Figure 4.14 Current density–voltage characteristics of pentacene diodes with surface-modified gold. Inset shows the rectification ratio of the diodes.

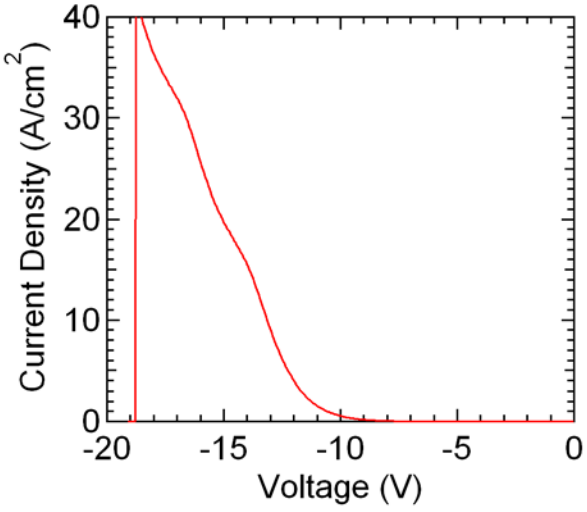

Figure 4.15 Reverse-bias breakdown voltage of a pentacene diode with PFBT-modified gold.

4.3.2 Frequency Performances of Pentacene Rectifiers with SAM-treated Gold

Figure 4.15(a) shows a frequency setup of the pentacene rectifier, which is composed of the diode, 10 nF of a load capacitor and 1 MΩ of load resistor. To reduce ripple voltage in a rectifier, the period of an input voltage should be much smaller than a load capacitor times a load resistor and capacitance of the load capacitor should be much larger than capacitance of the diode.[29] The former condition can be negligible as the frequency increases but the latter condition, related to the diode area, should be carefully considered. The capacitance of the pentacene diode is measured to be 1.7 pF, satisfying above conditions. The size of a diode is one of the important design factors in the RFID tags. Small area of the diode increases breakdown voltage, enduring higher rf power.[74] Moreover, for the all-printed RFID tags, most of the area is occupied by a load capacitor; thus, due to the latter condition, small area of the diode facilitates to fabricate small size of RFID tags, which is advantageous for low-cost production. However, small size of a diode decreases power capability of a rectifier so size of a diode is carefully designed considering input voltage, cost-efficiency, and power consumption of the circuit. The area of the diode in this study is designed to be $80 \times 80\ \mu m^2$.

When 10-V sinusoidal voltage is applied to the rectifier, the frequency characteristics of the rectifier with a pentacene diode on PFBT-treated Au are shown in Figure 4.15(b). At the low frequency, 1 MHz, 6.2 V of output voltage is measured. Four volts drop of output voltage compared to input voltage is due to power consumption of the load resistor and reverse-bias leakage current of the diode. As the frequency increases, additional leakage current flows via the capacitor of the diode, decreasing output voltage of the rectifier. If the diode is considered as a single

RC model, frequency dependency of the output voltage can be described by Eq. 2.11. By fitting the measured data from this equation, which is shown in solid line of Figure 4.15(b), V_0 and f_c are obtained to be 6.02 V and 716 MHz, respectively. Also, 3-dB frequency, in terms of voltage, which is usually used for measuring frequency performance of the organic rectifier, are obtained to be 1.24 GHz from fitting line, which is a highest value ever reported. Finally, output voltage of 3.8 V at 1 GHz is obtained when input voltage of 10 V is applied.

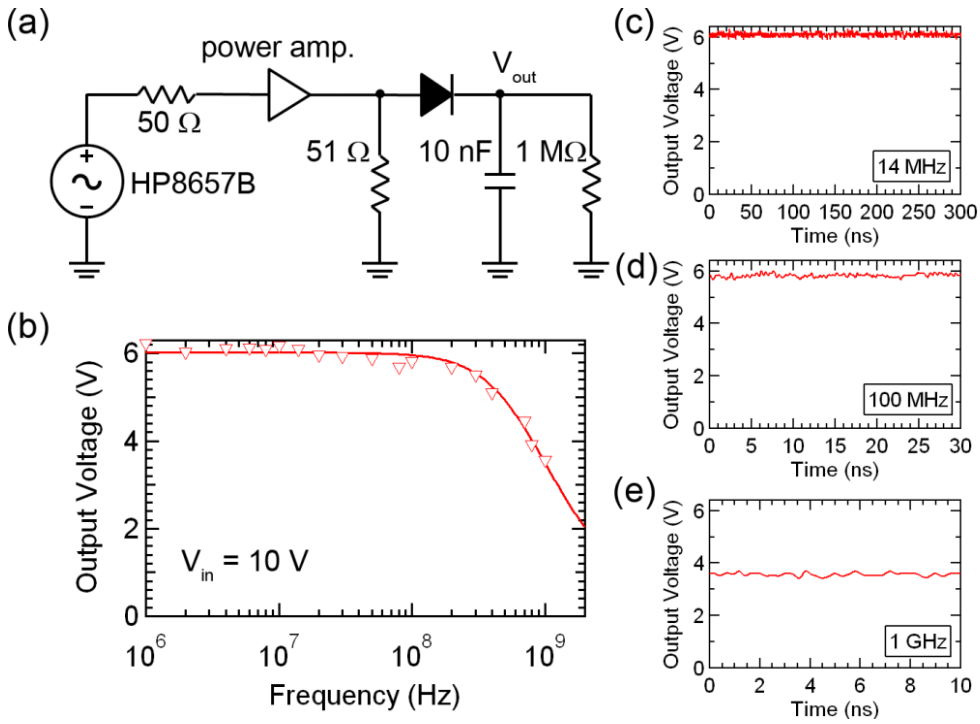

Figure 4.16 (a) The equivalent circuit of a pentacene rectifier measurement setup. (b) Frequency characteristics of a rectifier based on the pentacene diode with PFBT-modified gold when input voltage of 10 V is applied. The output voltage of the pentacene rectifier at (c) 14 MHz, (d) 100 MHz, and (e) 1 GHz.

4.4 Demonstration of UHF Operating Pentacene Rectifiers

4.4.1 Design of Antennas for UHF RFID tags

To demonstrate the pentacene rectifier operable at UHF region, we firstly design the antenna for UHF RFID tag. For 500 MHz, the size of T-matched antenna is simulated to be 20 cm × 7.1 cm, which is too large to use for real applications; thus, loop antenna is used. The resonant length of loop antenna is 60 cm for 500 MHz so loop antenna size is to be 15 cm × 15 cm, which is still too large to use. Therefore, meander pattern is applied for antenna miniaturization and the size of the antenna with meander pattern is to be 10 cm × 10 cm, which is suitable to use for real applications. The meander pattern-designed antenna exhibits omni-directional radiation pattern as shown in Figure 4.17(a). The electric field which radiates perpendicular to *xy*-plane exhibits strongest emission, and the field along *x*-axis exhibits weakest emission, indicating that plane electromagnetic (EM) wave through the antenna loop resonant more than that parallel to the loop. The meander-patterned loop antenna resonant well at 500 MHz with return loss of about -15 dB and bandwidth at -10 dB is about 12 MHz as shown in Figure 4.17(c).

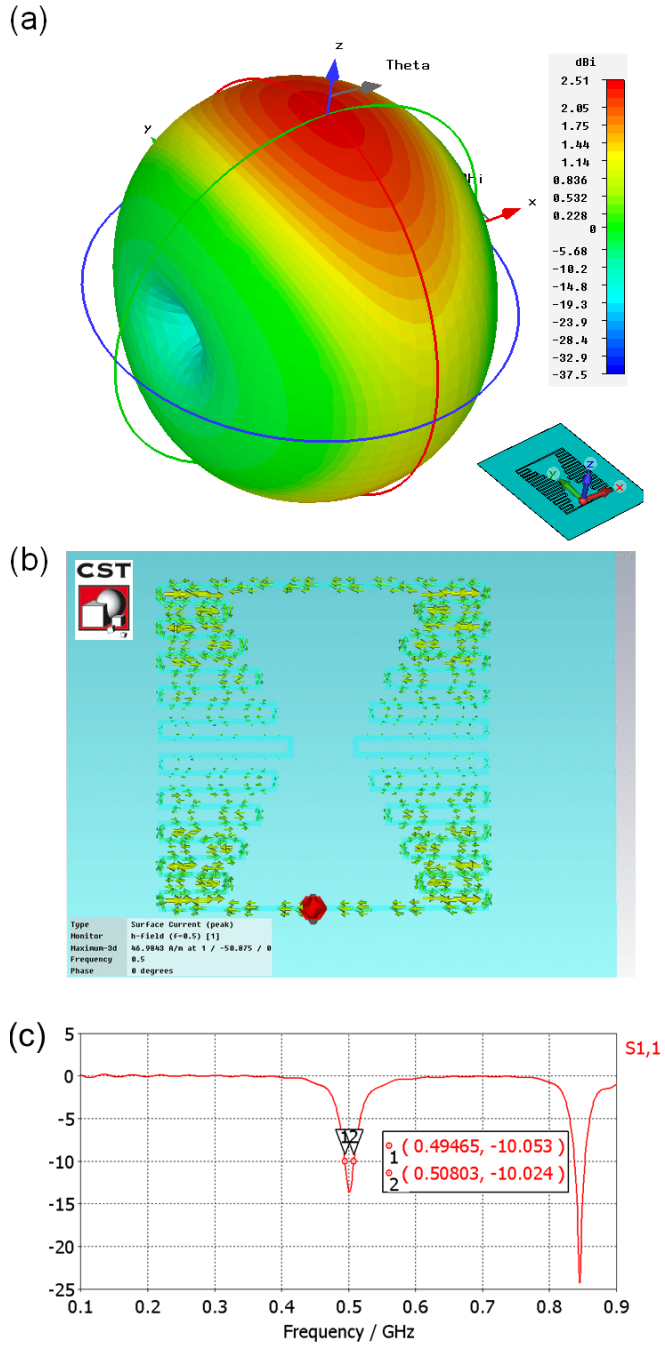

Figure 4.17 (a) Radiation pattern of meander type loop antenna for 500 MHz. (b) Current distribution of the loop antenna. (c) Simulated return loss of the designed antenna.

4.4.2 Loop Antenna Fabrication Using Screen Printing

The screen printing method is used to fabricate flexible printed UHF antenna. Screen printing is a simple, low-cost, fast method which is widely used for patterning. The Ag ink is placed on top of patterned woven mesh and blade squeeze the Ag ink then the Ag is transferred from stencil to the substrate. The Ag ink is purchased by EMS corp (CI-1001). For the good resolution, the Ag ink should have sufficient viscosity. Viscosity of Ag ink in this study is used to be 12,000 cps at 30 °C. Total solid content in the Ag ink is 61 % and electrical sheet resistance is about 0.015 Ω/sq. The thickness of screen printed Ag forms a range of 1–2 μm and surface roughness in RMS value is about 340 nm. 200-nm thick poly arylate (PAR) is used for the flexible substrates.

Figure 4.18(a) shows the photo image of the loop antenna for 500 MHz fabricated by screen printing on PAR substrate The 500 MHz loop antenna is successfully fabricated using screen printing. The return loss of 500 MHz loop antenna using screen printing is shown in Figure 4.18(b). The loop antenna fabricated by PCB exhibits the resonant peak at 500.6 MHz, bandwidth at -10 dB of 26.9 MHz, and return loss at 500 MHz of -27.8 dB. Whereas, the loop antenna fabricated by screen printing on flexible substrate exhibits the resonant peak at 490.6 MHz, bandwidth at -10 dB of 29.1 MHz, and return loss at 500 MHz of -12.9 dB. Due to the relative high resistivity of screen printed antenna, the wider bandwidth and smaller resonant peak can be obtained. However, return loss of -10 dB indicates that only 10 % of the voltage is reflected so it is enough to use for antenna.

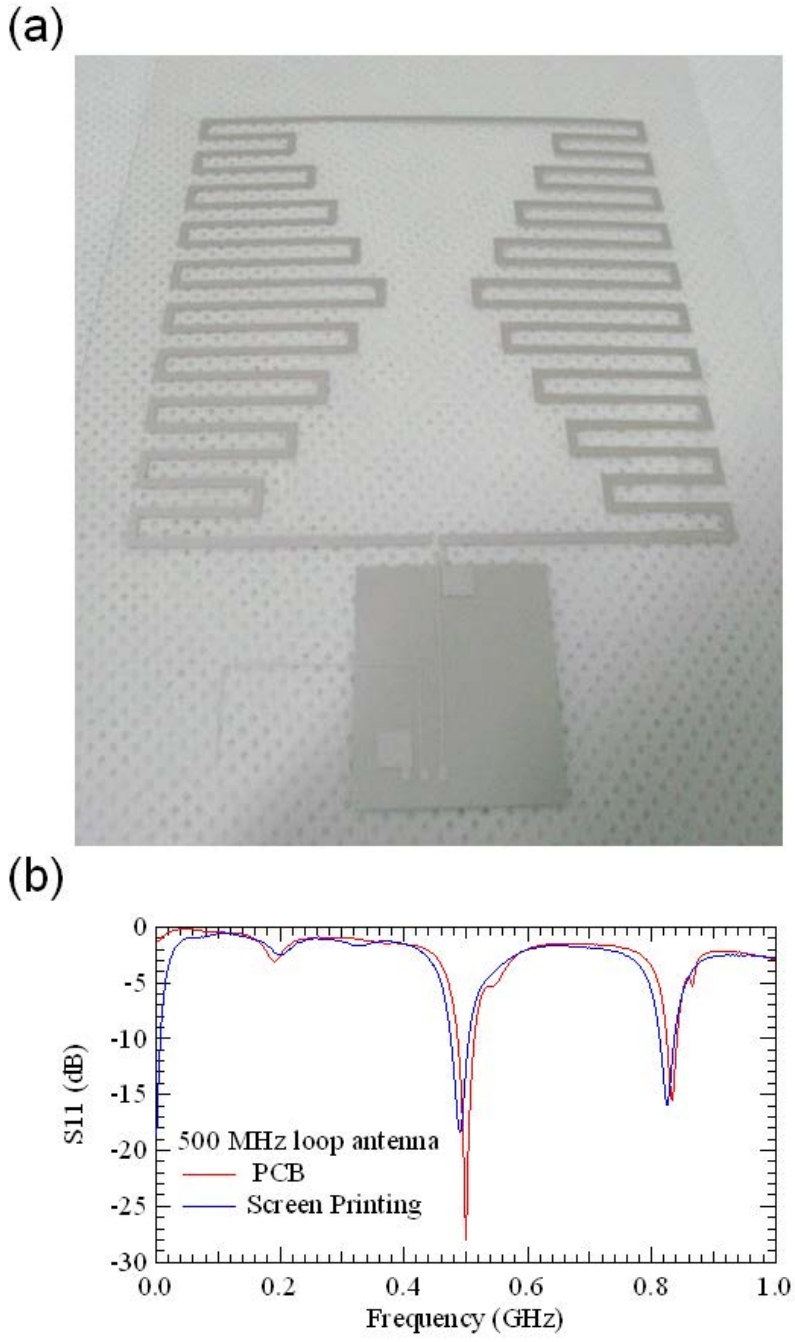

Figure 4.18 (a) The photo image of the loop antenna for 500 MHz fabricated by screen printing on flexible substrate. (b) return loss of 500-MHz loop antenna using screen printing (blue solid) and PCB (red solid)

4.4.3 Demonstration of Pentacene Rectifiers Operating at 500 MHz

Finally, we demonstrated the pentacene rectifier with surface-modified gold operating at 500 MHz. Figure 4.19 shows the measurement setup of the pentacene rectifier operating at 500 MHz. the carrier frequency of 500 MHz is generated by signal generator and amplified through power amplifier. Then, electric power is transformed to radio wave by the 500-MHz designed transmitting antenna. The radio wave generated by transmitting antenna re-transformed to electric power by receiving antenna. The rotation between antennas is very important to maximize power transfer because the direction of electric field should be matched. 0° and 180° of rotational angle between antennas is allowed to receiving maximum electric power. Figure 4.20 shows the rectifying signal of 500 MHz operating rectenna (rectifier + antenna). The 2.9 V of dc signal can be obtained. There is some ripple current of about 0.9 V, which possibly due to the unbalanced antenna signal between right and left side, inductance of the line, and leakage current of the diode. However, it can be easily diminish by employing high pass filter because the frequency of the ripple current is 500 MHz. Although the performance of pentacene rectifier is enough to use at the 1 GHz region, demonstration of pentacene rectenna operating at 1 GHz is very hard because of impedance matching. The rectifier is active device which means that impedance is varied by the applied voltage and it deals with large signal, it is hard to match impedance between antenna and the rectifier. However, because active UHF RFID tags is about 450 MHz, our work shows bright future of low-cost flexible RFID tags based on organic materials.

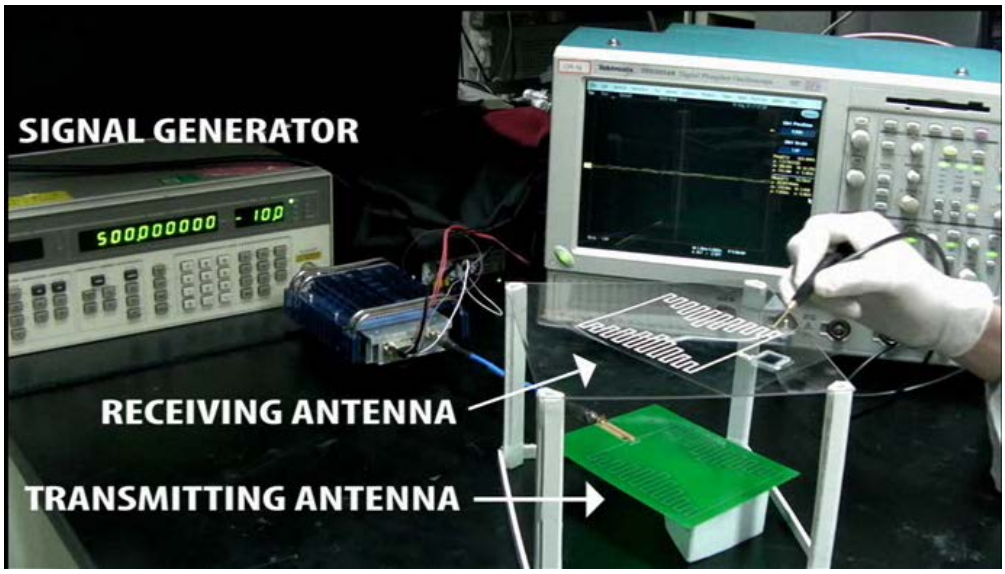

Figure 4.19 Measurement setup of the pentacene rectifier operating at 500 MHz

Figure 4.20 Rectifying signal of 500 MHz operable rectifier with antenna.

4.5 Summary

In summary, we investigated the structure–property relationship of pentacene on gold and SAM-treated gold along the vertical direction. From the photoelectron spectrometer, the work function of gold, TP-modified gold and PFBT-modified gold is measured to be 4.78, 4.67, and 5.02 eV, respectively. PFBT-treated gold effectively lower the injection barrier between the anode and the active layer, the forward-bias current density of the diode with PFBT-treated gold is much higher than that with pristine gold and finally current density of 100 A/cm^2 is obtained at 3 V. In addition, the rectification ratio of the diode is founded to be 7.47×10^5 at 1 V, and 1.05×10^7 at 2.8 V. The 3-dB frequency, in terms of voltage, of the rectifier which is composed of the diode and a capacitor is obtained to be 1.24 GHz. Finally, V_{out} of 3.8 V at 1 GHz is obtained when input voltage of 10 V is applied. From the XRD, AFM, and Raman analysis, pentacene molecules on gold exhibit lying-down orientation and those on PFBT-treated gold exhibit standing-up orientation. These structure differences change the electrical property. The mobility, calculated by SCLC, of the pentacene film on gold and PFBT-treated gold is measured to be 6.82×10^{-4} and 0.114 $cm^2V^{-1}s^{-1}$, respectively. From the XRD and vertical SEM images, it can be considered that pentacene on gold exhibits the entangled and disordered structure whereas pentacene on PFBT-treated gold exhibits dense and ordered structure. This poor molecular ordering for pentacene on gold can limit charge transport property, resulting that the mobility of the pentacene film on gold is smaller than that of on PFBT-treated gold. Although the performance of pentacene rectifier is enough to use at the UHF region, pentacene thin films easily react with oxygen and moisture so it easily degraded under ambient condition, which indicates that it is hard to apply low-cost plastic RFID tags. However, because SAM can be

applied to any p-type organic semiconductors which have rapidly developed for high mobility and stability in recent years, we believe that low-cost flexible RFID tags based on organic materials will be developed in the near future.

Chapter 5

Conclusion

In this thesis, we investigate organic/metal interface of the diode to enhance charge injection efficiency and demonstrate high performance organic diodes. Two major methods are used to improve device performance: improved charge injection by electrical annealing and reduced hole injection barrier by using permanent dipole moment of SAM.

First, we investigate the effect of electrical annealing on pentacene diode to which electrical annealing has not been applied because it cannot have ionic species. By using MoO_3 instead of ionic species, electrical annealing can be applied to thermally deposited device which is advantageous for fabricating high performance devices. After electrical annealing, the turn-on voltage is reduced from approximately 1.3 V to 0.2 V and current at 3 V is increased from approximately 0.2 mA to 1 mA without increase of the reverse-bias current. In addition to MoO_3 as a hole injection layer, HAT-CN and $F_{16}CuPc$, which have deep HOMO levels, show

electrical annealing effect but PEDOT:PSS, m-MTDATA, and CuPc do not affect electrical annealing. the cutoff frequency was increased from 10.5 MHz to 85.7 MHz. There is no improvement of current or reduction of turn-on voltage by using temperature annealing only, indicating that electric field plays an important role for electrical annealing. From the ToF-SIMS and impedance spectra, we conclude that the device performance of the pentacene diode is improved by electrical annealing due to the creation of the pentacene:MoO_3 mixed layer. The mixed layer effectively increases charge injection by reducing small potential barrier which causes the turn-on voltage of *I–V* characteristics and the RC-component at Au/MoO_3/pentacene interface of impedance spectra. Note that because this uniform and thin pentacene:MoO_3 mixed layer cannot be formed by thermal evaporation, electrical annealing is the best technique to form the uniform, thin, and gradual pentacene:MoO_3 mixed layer for improving device performance. After electrical annealing, Al penetration into the pentacene layer was also observed. Because Al was deposited on the polycrystalline pentacene, Al spikes are formed at the pentacene grain boundary. These Al spikes can induce a higher electric field, facilitating the penetration of Al. Therefore, the penetrated Al may create rod-like structures that can be modeled as CPE.

Second, we investigated the structure–property relationship of pentacene on gold and SAM-treated gold along the vertical direction. From the photoelectron spectrometer, the work function of gold, TP-modified gold and PFBT-modified gold is measured to be 4.78, 4.67, and 5.02 eV, respectively. PFBT-treated gold effectively lower the injection barrier between the anode and the active layer, the forward-bias current density of the diode with PFBT-treated gold is much higher than that with pristine gold and finally current density of 100 A/cm^2 is obtained at 3 V. In addition, the rectification ratio of the diode is founded to be 7.47×10^5 at 1 V,

and 1.05×10^7 at 2.8 V. The 3-dB frequency, in terms of voltage, of the rectifier which is composed of the diode and a capacitor is obtained to be 1.24 GHz. Finally, V_{out} of 3.8 V at 1 GHz is obtained when input voltage of 10 V is applied. From the XRD, AFM, and Raman analysis, pentacene molecules on gold exhibit lying-down orientation and those on PFBT-treated gold exhibit standing-up orientation. These structure differences change the electrical property. The mobility, calculated by SCLC, of the pentacene film on gold and PFBT-treated gold is measured to be 6.82×10^{-4} and 0.114 $cm^2V^{-1}s^{-1}$, respectively. From the XRD and vertical SEM images, it can be considered that pentacene on gold exhibits the entangled and disordered structure whereas pentacene on PFBT-treated gold exhibits dense and ordered structure. This poor molecular ordering for pentacene on gold can limit charge transport property, resulting that the mobility of the pentacene film on gold is smaller than that of on PFBT-treated gold.

These two methods can also be applied to other materials and devices such as OPVs, OLEDs, OTFTs, and QD devices as well as pentacene and the rectifier. Moreover, the p-type organic semiconductors have rapidly developed for high mobility and stability in recent years, we believe that low-cost flexible electronics based on organic materials will be developed in the near future.

Bibilography

[1] R. Tinivella, V. Camarchia, M. Pirola, *et al.*, "Simulation and design of OFET RFIDs through an analog/digital physics-based library," *Organic Electronics,* vol. 12, no. 8, pp.1328-1335, 2011.

[2] K. Ishida, H. Tsung-Ching, K. Honda, *et al.*, "Insole Pedometer With Piezoelectric Energy Harvester and 2 V Organic Circuits," *Solid-State Circuits, IEEE Journal of,* vol. 48, no. 1, pp.255-264, 2013.

[3] T. Sekitani, U. Zschieschang, H. Klauk, *et al.*, "Flexible organic transistors and circuits with extreme bending stability," *Nat Mater,* vol. 9, no. 12, pp.1015-1022, 2010.

[4] F. Amy, C. Chan and A. Kahn, "Polarization at the gold/pentacene interface," *Organic Electronics,* vol. 6, no. 2, pp.85-91, 2005.

[5] L. Diao, C. D. Frisbie, D. D. Schroepfer, *et al.*, "Electrical characterization of metal/pentacene contacts," *Journal of applied physics,* vol. 101, no. 1, pp.014510-014518, 2007.

[6] H. Ishii, K. Sugiyama, E. Ito, *et al.*, "Energy Level Alignment and Interfacial Electronic Structures at Organic/Metal and Organic/Organic Interfaces," *Advanced Materials,* vol. 11, no. 8, pp.605-625, 1999.

[7] G. Heywang and F. Jonas, "Poly(alkylenedioxythiophene)s—new, very stable conducting polymers," *Advanced Materials,* vol. 4, no. 2, pp.116-118, 1992.

[8] X. Zhou, M. Pfeiffer, J. Blochwitz, *et al.*, "Very-low-operating-voltage organic light-emitting diodes using a p-doped amorphous hole injection layer," *Applied physics letters,* vol. 78, no. 4, pp.410-412, 2001.

[9] S. Tokito, K. Noda and Y. Taga, "Metal oxides as a hole-injecting layer for an organic electroluminescent device," *Journal of Physics D: Applied Physics,* vol. 29, no. 11, pp.2750, 1996.

[10] T.-W. Lee and O. O. Park, "Effect of electrical annealing on the luminous efficiency of thermally annealed polymer light-emitting diodes," *Applied physics letters,* vol. 77, no. 21, pp.3334-3336, 2000.

[11] I. H. Campbell, J. D. Kress, R. L. Martin, *et al.*, "Controlling charge injection in organic electronic devices using self-assembled monolayers," *Applied physics letters,* vol. 71, no. 24, pp.3528-3530, 1997.

[12] I. H. Campbell, S. Rubin, T. A. Zawodzinski, *et al.*, "Controlling Schottky energy barriers in organic electronic devices using self-assembled monolayers," *Physical Review B,* vol. 54, no. 20, pp.R14321-R14324, 1996.

[13] M. Dongge, J. M. Lupton, R. Beavington, *et al.*, "Improvement of luminescence efficiency by electrical annealing in single-layer organic light-emitting diodes based on a conjugated dendrimer," *Journal of Physics D: Applied Physics,* vol. 35, no. 6, pp.520, 2002.

[14] F. Padinger, R. S. Rittberger and N. S. Sariciftci, "Effects of Postproduction Treatment on Plastic Solar Cells," *Advanced Functional Materials,* vol. 13, no. 1, pp.85-88, 2003.

[15] Y. C. Yim, J. H. Park, S. W. Kim, *et al.*, "Enhanced light emission from one-layered organic light-emitting devices doped with organic salt by simultaneous thermal and electrical annealing," *Applied physics letters,* vol. 89, no. 10, pp.103507-103503, 2006.

[16] Y. Li, Y. Hou, Y. Wang, *et al.*, "Thermal treatment under reverse bias: Effective tool for polymer/fullerene bulk heterojunction solar cells," *Synthetic Metals,* vol. 158, no. 5, pp.190-193, 2008.

[17] B. Park, C. H. Park, Y. Yim, *et al.*, "Electrical annealing for flexible organic light-emitting diodes having poly(3,4-ethylenedioxythiophene):poly(styrene sulfonate) anodes," *Journal of applied physics,* vol. 108, no. 8, pp.084508-084506, 2010.

[18] L. Zuppiroli, L. Si-Ahmed, K. Kamaras, *et al.*, "Self-assembled monolayers as interfaces for organic opto-electronic devices," *Eur. Phys. J. B,* vol. 11, no. 3, pp.505-512, 1999.

[19] B. de Boer, A. Hadipour, M. M. Mandoc, *et al.*, "Tuning of Metal Work Functions with Self-Assembled Monolayers," *Advanced Materials,* vol. 17, no. 5, pp.621-625, 2005.

[20] L.-W. Chong, Y.-L. Lee and T.-C. Wen, "Surface modification of indium tin oxide anodes by self-assembly monolayers: Effects on interfacial morphology and charge injection in organic light-emitting diodes," *Thin Solid Films,* vol. 515, no. 5, pp.2833-2841, 2007.

[21] H.-L. Yip, S. K. Hau, N. S. Baek, *et al.*, "Self-assembled monolayer modified ZnO/metal bilayer cathodes for polymer/fullerene bulk-heterojunction solar cells," *Applied physics letters,* vol. 92, no. 19, pp.193313-193313, 2008.

[22] J. S. Kim, J. H. Park, J. H. Lee, *et al.*, "Control of the electrode work function and active layer morphology via surface modification of indium tin oxide for high efficiency organic photovoltaics," *Applied physics letters*, vol. 91, no. 11, pp.112111-112113, 2007.

[23] B. H. Hamadani, D. A. Corley, J. W. Ciszek, *et al.*, "Controlling Charge Injection in Organic Field-Effect Transistors Using Self-Assembled Monolayers," *Nano Letters*, vol. 6, no. 6, pp.1303-1306, 2006.

[24] D. J. Gundlach, J. Li Li and T. N. Jackson, "Pentacene TFT with improved linear region characteristics using chemically modified source and drain electrodes," *Electron Device Letters, IEEE*, vol. 22, no. 12, pp.571-573, 2001.

[25] J.-P. Hong, A.-Y. Park, S. Lee, *et al.*, "Tuning of Ag work functions by self-assembled monolayers of aromatic thiols for an efficient hole injection for solution processed triisopropylsilylethynyl pentacene organic thin film transistors," *Applied physics letters*, vol. 92, no. 14, pp.143311-143313, 2008.

[26] R. H. Fowler and L. Nordheim, "Electron Emission in Intense Electric Fields," *Proceedings of the Royal Society of London. Series A*, vol. 119, no. 781, pp.173-181, 1928.

[27] M. A. Lampert and P. Mark 1970 *Current injection in solids*: Academic Press New York)

[28] S. Steudel, K. Myny, V. Arkhipov, *et al.*, "50 MHz rectifier based on an organic diode," *Nature materials*, vol. 4, no. 8, pp.597-600, 2005.

[29] W. D. Gill, "Drift mobilities in amorphous charge-transfer complexes of trinitrofluorenone and poly-n-vinylcarbazole," *Journal of applied physics*, vol. 43, no. 12, pp.5033-5040, 1972.

[30] L. J. van der Pauw, "A method of measuring specific resistivity and Hall effect of discs of arbitrary shape," *Philips Res.Rep,* vol. 13, no. 1, 1958.

[31] R. F. Pierret 1996 *Semiconductor device fundamentals*: Addison-Wesley)

[32] A. Many, S. Z. Weisz and M. Simhony, "Space-Charge-Limited Currents in Iodine Single Crystals," *Physical Review,* vol. 126, no. 6, pp.1989-1995, 1962.

[33] A. Rose, "Space-Charge-Limited Currents in Solids," *Physical Review,* vol. 97, no. 6, pp.1538-1544, 1955.

[34] G. Juška, K. Arlauskas, M. Viliūnas, *et al.*, "Extraction Current Transients: New Method of Study of Charge Transport in Microcrystalline Silicon," *Physical Review Letters,* vol. 84, no. 21, pp.4946-4949, 2000.

[35] G. Juška, K. Arlauskas, M. Viliūnas, *et al.*, "Charge transport in π-conjugated polymers from extraction current transients," *Physical Review B,* vol. 62, no. 24, pp.R16235-R16238, 2000.

[36] A. J. Mozer, N. S. Sariciftci, L. Lutsen, *et al.*, "Charge transport and recombination in bulk heterojunction solar cells studied by the photoinduced charge extraction in linearly increasing voltage technique," *Applied physics letters,* vol. 86, no. 11, pp.112104-112103, 2005.

[37] X. Zhou, J. He, L. S. Liao, *et al.*, "Real-Time Observation of Temperature Rise and Thermal Breakdown Processes in Organic LEDs Using an IR Imaging and Analysis System," *Advanced Materials,* vol. 12, no. 4, pp.265-269, 2000.

[38] S. Chung, J.-H. Lee, J. Jeong, *et al.*, "Substrate thermal conductivity effect on heat dissipation and lifetime improvement of organic light-emitting diodes," *Applied physics letters,* vol. 94, no. 25, pp.253302-253303, 2009.

[39] M. Kroger, S. Hamwi, J. Meyer, *et al.*, "Role of the deep-lying electronic states of MoO[sub 3] in the enhancement of hole-injection in organic thin films," *Applied physics letters*, vol. 95, no. 12, pp.123301-123303, 2009.

[40] M. Kröger, S. Hamwi, J. Meyer, *et al.*, "P-type doping of organic wide band gap materials by transition metal oxides: A case-study on Molybdenum trioxide," *Organic Electronics*, vol. 10, no. 5, pp.932-938, 2009.

[41] K. Kanai, K. Koizumi, S. Ouchi, *et al.*, "Electronic structure of anode interface with molybdenum oxide buffer layer," *Organic Electronics*, vol. 11, no. 2, pp.188-194, 2010.

[42] Q. Y. Bao, J. P. Yang, Y. Q. Li, *et al.*, "Electronic structures of MoO[sub 3]-based charge generation layer for tandem organic light-emitting diodes," *Applied physics letters*, vol. 97, no. 6, pp.063303-063303, 2010.

[43] Y.-K. Kim, J. W. Kim and Y. Park, "Energy level alignment at a charge generation interface between 4,4[sup [prime]]-bis(N-phenyl-1-naphthylamino)biphenyl and 1,4,5,8,9,11-hexaazatriphenylene-hexacarbonitrile," *Applied physics letters*, vol. 94, no. 6, pp.063305-063303, 2009.

[44] Y. Gao, H. Ding, H. Wang, *et al.*, "Electronic structure of interfaces between copper-hexadecafluoro-phthalocyanine and 2,5-bis(4-biphenylyl) bithiophene," *Applied physics letters*, vol. 91, no. 14, pp.142112-142113, 2007.

[45] A. S. Sedra and K. C. Smith 1998 *Microelectronic Circuits*: Oxford University Press)

[46] S. D. Ha, J. Meyer and A. Kahn, "Molecular-scale properties of MoO_3 doped pentacene," *Physical Review B*, vol. 82, no. 15, pp.155434, 2010.

[47] Z. Wang, M. W. Alam, Y. Lou, *et al.*, "Enhanced carrier injection in pentacene thin-film transistors by inserting a MoO[sub 3]-doped pentacene layer," *Applied physics letters*, vol. 100, no. 4, pp.043302-043304, 2012.

[48] J. Endo, T. Matsumoto and J. Kido, "Organic Electroluminescent Devices
 with a Vacuum-Deposited Lewis-Acid-Doped Hole-Injecting Layer," *Japanese Journal of Applied Physics*, vol. 41, no. Copyright (C) 2002 The Japan Society of Applied Physics, pp.L358, 2002.

[49] W.-J. Shin, J.-Y. Lee, J. C. Kim, *et al.*, "Bulk and interface properties of molybdenum trioxide-doped hole transporting layer in organic light-emitting diodes," *Organic Electronics*, vol. 9, no. 3, pp.333-338, 2008.

[50] C.-m. Kang, S. Kim, Y. Hong, *et al.*, "Frequency analysis on poly(3-hexylthiopene) rectifier using impedance spectroscopy," *Thin Solid Films*, vol. 518, no. 2, pp.889-892, 2009.

[51] S. Kochowski and K. Nitsch, "Description of the frequency behaviour of metal–SiO2–GaAs structure characteristics by electrical equivalent circuit with constant phase element," *Thin Solid Films*, vol. 415, no. 1–2, pp.133-137, 2002.

[52] E. Barsoukov and J. R. Macdonald 2005 *Impedance spectroscopy: theory, experiment, and applications*: Wiley. com)

[53] J. Bisquert, G. Garcia-Belmonte, F. Fabregat-Santiago, *et al.*, "Doubling Exponent Models for the Analysis of Porous Film Electrodes by Impedance. Relaxation of TiO2 Nanoporous in Aqueous Solution," *The Journal of Physical Chemistry B*, vol. 104, no. 10, pp.2287-2298, 2000.

[54] K. Asadi, F. Gholamrezaie, E. C. P. Smits, *et al.*, "Manipulation of charge carrier injection into organic field-effect transistors by self-assembled

monolayers of alkanethiols," *Journal of Materials Chemistry,* vol. 17, no. 19, pp.1947-1953, 2007.

[55] J. Park, W. H. Lee, S. Huh, *et al.*, "Work-Function Engineering of Graphene Electrodes by Self-Assembled Monolayers for High-Performance Organic Field-Effect Transistors," *The Journal of Physical Chemistry Letters,* vol. 2, no. 8, pp.841-845, 2011.

[56] P. Marmont, N. Battaglini, P. Lang, *et al.*, "Improving charge injection in organic thin-film transistors with thiol-based self-assembled monolayers," *Organic Electronics,* vol. 9, no. 4, pp.419-424, 2008.

[57] R. A. Hatton, S. R. Day, M. A. Chesters, *et al.*, "Organic electroluminescent devices: enhanced carrier injection using an organosilane self assembled monolayer (SAM) derivatized ITO electrode," *Thin Solid Films,* vol. 394, no. 1–2, pp.291-296, 2001.

[58] B. O. Acton, G. G. Ting, P. J. Shamberger, *et al.*, "Dielectric Surface-Controlled Low-Voltage Organic Transistors via n-Alkyl Phosphonic Acid Self-Assembled Monolayers on High-k Metal Oxide," *ACS Applied Materials & Interfaces,* vol. 2, no. 2, pp.511-520, 2010.

[59] D. H. Kim, H. S. Lee, H. Yang, *et al.*, "Tunable Crystal Nanostructures of Pentacene Thin Films on Gate Dielectrics Possessing Surface-Order Control," *Advanced Functional Materials,* vol. 18, no. 9, pp.1363-1370, 2008.

[60] K. Fukuda, T. Hamamoto, T. Yokota, *et al.*, "Effects of the alkyl chain length in phosphonic acid self-assembled monolayer gate dielectrics on the performance and stability of low-voltage organic thin-film transistors," *Applied physics letters,* vol. 95, no. 20, pp.203301-203303, 2009.

[61] W. S. Hu, Y. T. Tao, Y. J. Hsu, *et al.*, "Molecular Orientation of Evaporated Pentacene Films on Gold: Alignment Effect of Self-Assembled Monolayer," *Langmuir,* vol. 21, no. 6, pp.2260-2266, 2005.

[62] D. Käfer, L. Ruppel and G. Witte, "Growth of pentacene on clean and modified gold surfaces," *Physical Review B,* vol. 75, no. 8, pp.085309, 2007.

[63] A. Wan, J. Hwang, F. Amy, *et al.*, "Impact of electrode contamination on the α-NPD/Au hole injection barrier," *Organic Electronics,* vol. 6, no. 1, pp.47-54, 2005.

[64] N. Koch, A. Elschner, J. Schwartz, *et al.*, "Organic molecular films on gold versus conducting polymer: Influence of injection barrier height and morphology on current--voltage characteristics," *Applied physics letters,* vol. 82, no. 14, pp.2281-2283, 2003.

[65] C. H. Kim, O. Yaghmazadeh, D. Tondelier, *et al.*, "Capacitive behavior of pentacene-based diodes: Quasistatic dielectric constant and dielectric strength," *Journal of applied physics,* vol. 109, no. 8, pp.083710-083719, 2011.

[66] Y. Zheng, D. Qi, N. Chandrasekhar, *et al.*, "Effect of Molecule−Substrate Interaction on Thin-Film Structures and Molecular Orientation of Pentacene on Silver and Gold," *Langmuir,* vol. 23, no. 16, pp.8336-8342, 2007.

[67] C. Schmidt, A. Witt and G. Witte, "Tailoring the Cu (100) Work Function by Substituted Benzenethiolate Self-Assembled Monolayers," *The Journal of Physical Chemistry A,* vol. 115, no. pp.7234-7241, 2011.

[68] K. A. Singh, T. L. Nelson, J. A. Belot, *et al.*, "Effect of Self-Assembled Monolayers on Charge Injection and Transport in Poly(3-hexylthiophene)-Based Field-Effect Transistors at Different Channel Length Scales," *ACS Applied Materials & Interfaces,* vol. 3, no. 8, pp.2973-2978, 2011.

[69] Z. Jia, V. W. Lee, I. Kymissis, *et al.*, "In situ study of pentacene interaction with archetypal hybrid contacts: Fluorinated versus alkane thiols on gold," *Physical Review B*, vol. 82, no. 12, pp.125457, 2010.

[70] D. Im, H. Moon, M. Shin, *et al.*, "Towards Gigahertz Operation: Ultrafast Low Turn-on Organic Diodes and Rectifiers Based on C60 and Tungsten Oxide," *Advanced Materials*, vol. 23, no. 5, pp.644-648, 2011.

[71] B. N. Pal, J. Sun, B. J. Jung, *et al.*, "Pentacene Zinc Oxide Vertical Diode with Compatible Grains and 15 MHz Rectification," *Advanced Materials*, vol. 20, no. 5, pp.1023-1028, 2008.

[72] K. Myny, S. Steudel, P. Vicca, *et al.*, "An integrated double half-wave organic Schottky diode rectifier on foil operating at 13.56 MHz," *Applied physics letters*, vol. 93, no. 9, pp.093305-093305-093303, 2008.

[73] S. Kim, H. Cho, Y. Hong, *et al.*, "Effect of electrode area on high speed characteristics over 1 MHz of poly (3-hexylthiophene-2, 5-diyl) diode with inkjet-printed Ag electrode," *Molecular Crystals and Liquid Crystals*, vol. 513, no. 1, pp.256-261, 2009.

Publication

[1] SCI Journal Papers

1. **Chan-mo Kang**, Seohee Kim, Yongtaek Hong, and Changhee Lee, “Frequency analysis on poly(3-hexylthiopene) rectifier using impedance spectroscopy”, *Thin Solid Films* **518**, 889 (2009).
2. **Chan-mo Kang**, Yongtaek Hong, and Changhee Lee, “Frequency Performance Optimization of Flexible Pentacene Rectifier by Varying the Thickness of Active Layer”, *Japanese Journal of Applied Physics* **49**, 05EB07 (2010).
3. **Chan-mo Kang**, Hyunduck Cho, Hyunkoo Lee, and Changhee Lee, “Organic Rectifier with Transfer-printed Metal as a Top Electrode”, *Journal of the Korean Physical Society* **59**, 470 (2011).
4. Hyunkoo Lee, **Chan-Mo Kang**, Myeongjin Park, Jeonghun Kwak, and Changhee Lee, “Improved Efficiency of Inverted Organic Light-Emitting Diodes Using Tin Dioxide Nanoparticles as an Electron Injection Layer”, *ACS Applied Materials & Interfaces* **5**, 1977 (2013).
5. Yuntae Kim, Jeongkyun Roh, Ji-Hoon Kim, **Chan-Mo Kang**, In-Nam Kang, Byung Jun Jung, Changhee Lee, and Do-Hoon Hwang, “Photocurable propyl-

cinnamate-functionalized polyhedral oligomeric silsesquioxane as a gate dielectric for organic thin film transistors", *Organic Electronics* **14**, 2315 (2013).

6. Jeongkyun Roh, Jaemin Lee, **Chan-mo Kang**, Changhee Lee, and Byung Jun Jung, "Air stability of PTCDI-C13 based n-OFETs on polymer interfacial layers", *physica status solidi (RRL) - Rapid Research Letters* **7**, 469 (2013).

[2] KCI Journal Papers

1. Mingyu Kim, Hyunduck Cho, Jeonghun Kwak, **Chan-mo Kang**, Myeongjin Park, and Changhee Lee, "Organic complementary inverter and ring oscillator on a flexible substrate", *Journal of Information Display* **12**, 1 (2011).

[3] International Conferences

1. **Chan-mo Kang**, Seohee Kim, Yongtaek Hong, and Changhee Lee, “Frequency Analysis on P3HT Rectifier Using Impedance Spectroscopy”, *The 8th International Conference on Nano-Molecular Electronics*, p. 362, December 2008.
2. **Chan-mo Kang**, Yongtaek Hong, and Changhee Lee, “Frequency Performance Optimization of Flexible Pentacene Rectifier by Varying the Thickness of Active Layer”, *International Conference on Flexible and Printed Electronics*, November 2009.
3. Changhee Lee, **Chan-mo Kang**, and Hyunduck Cho, “High-frequency rectifier based on printed organic diodes”, *International Workshop on Flexible & Printable Electronics*, November 2009.
4. **Chan-mo Kang**, Hyunduck Cho, Mingyu Kim, Myoung-jin Park, Yongtaek Hong, Ki-Woong Whang, Bo Hyung Cho, and Changhee Lee, “High Frequency Operating Pentacene Rectifying Diode with Inkjet Printed Electrode”, *3rd International Symposium on Flexible Organic Electronics (IS-FOE10)*, p. 114, July 2010.
5. Hyunduck Cho, Mingyu Kim, Myoung-jin Park, **Chan-mo Kang**, Yongtaek Hong, Ki-Woong Whang, Bo Hyung Cho, and Changhee Lee, “Organic Thin Film Transistors Using Transfer-Printed Ag Electrodes”, *3rd International Symposium on Flexible Organic Electronics (IS-FOE10)*, p. 102, July 2010.
6. Myoung-jin Park, Hyunduck Cho, Mingyu Kim, **Chan-mo Kang**, and Changhee Lee, “The Effects of Alkyl SAM Chain Length on Pentacene Thin-Film Transistors”, *International Meeting on Information Display 2010*, p.490, October 2010.

7. Hyunduck Cho, Jeonghun Kwak, Seunguk Noh, **Chan-mo Kang**, Yongtaek Hong, and Changhee Lee, “High-efficiency organic light-emitting transistors with double light-emitting layers”, *The 7th International Thin-Film Transistor Conference, Cambridge*, March 2011.
8. **Chan-mo Kang**, Hyunduck Cho, Myeongjin Park, Jeongkyun Roh, and Changhee Lee, “Effect of Hole Injection Layers in Pentacene Rectifiers”, *The 22nd International Conference on Molecular Electronics and Devices*, **Best Poster Award**, May 2011.
9. Jeongkyun Roh, Myeongjin Park, **Chan-mo Kang**, Hyunduck Cho, and Changhee Lee, “Enhanced Performance of All-Solution-Processed n-type Organic Thin Film Transistor by Employing Self-Assembled Monolayer.”, *International Meeting on Information Display*, October 2011.
10. **Chan-mo Kang**, Hyunduck Cho, Myeongjin Park, Jeongkyun Roh, Jeonghun Kwak, and Changhee Lee, “Improvement of Current Characteristics by Electrical Annealing in Organic Rectifying Diodes”, *International Conference on Science and Technology of Synthetic Metals 2012*, July 2012.
11. Jeongkyun Roh, **Chan-mo Kang**, Jeonghun Kwak, Byung Jun Jung, Changhee Lee, “Pentacene Thin Film Transistors on Fluorinated Self-Assembled Monolayer-Treated Gate Insulator and Their Gate Bias Stress Effect”, *International workshop on flexible and printable electronics*, November 2012.
12. Jeongkyun Roh, **Chan-mo Kang**, Jeonghun Kwak, Byung Jun Jung, Changhee Lee, “Improved Electrical Performance and Operational Stability of Organic Thin Film Transistors by Modifying Insulator Surface using Low-k Polymers”, *MRS Fall meeting*, November 2012.

13. **Chan-mo Kang**, Jeongkyun Roh, Hyeonwoo Shin, Changhee Lee, "Electrical and Morphological Properties of Pentacene Films on Surface-modified Gold", *2013 MRS Spring Meeting & Exhibit*, April 2013.
14. Jeongkyun Roh, **Chan-mo Kang**, Hyeonwoo Shin, Jeonghun Kwak, Byung Jun Jung, and Changhee Lee, "The Effect of Surface Polarity of Gate Dielectric Buffer Layer on Operational Stability in Organic Thin Film Transistors", *51st SID International Symposium, Seminar & Exhibition*, May 2013.
15. Jeongkyun Roh, Jaemin Lee, **Chan-mo Kang**, Byung Jun Jung, and Changhee Lee, "Improved Electrical Performance and Operational Stability through Interface Engineering for Organic Thin Film Transistors", *8th German-Korean Polymer Symposium*, **invited talk**, August 2013.

[2] Domestic Conferences

1. **강찬모**, 김서희, 홍용택, 이창희, "잉크젯 프린팅 전극을 이용한 고속 동작 TIPS-pentacene 정류기", *제 16 회 반도체 학술대회*, 2009 년 2 월.
2. 조현덕, **강찬모**, 홍용택, 이창희, "Organic Thin Film Transistor Using Solution-Processed Ag Electrodes", *제 16 회 한국반도체학술대회*, 2009 년 2 월.
3. 김민규, **강찬모**, 이창희, "잉크젯 프린팅을 이용한 OTFT 인버터", *제 17 회 한국 반도체 학술대회*, 2010 년 2 월.

4. **강찬모**, 조현덕, 김민규, 박명진, 이창희, “전사 인쇄법을 이용한 유기 정류기”, *제 18 회 한국반도체학술대회*, 2011 년 2 월.
5. 조현덕, 김민규, **강찬모**, 이창희, “Transfer Printing of TIPS-pentacene for Organic Thin-film Transistor”, *제 18 회 한국반도체학술대회*, 2011 년 2 월.
6. **강찬모**, 정승준, 홍용택, 이창희, “기판에 따른 유기 다이오드의 전력 전달 능력 연구”, *제 19 회 한국반도체학술대회*, 2012 년 2 월.
7. Myeongjin Park, Donggu Lee, Jaehoon Lim, Heeyoung Jung, **Chan-mo Kang**, Jung Hwa Seo, Jeonghun Kwak, Kookheon Char, Seonghun Lee, and Changhee Lee, “Enhancement in Charge Injection and Quantum Efficiency of Inverted Quantum Dot Light Emitting Diodes by Employing Different Metal Oxide Electron Transport Layers”, *제 20 회반도체학술대회*, 2013 년 2 월.

한글 초록

유기전자소자는 패터닝이 쉽고 유연하며 가볍고 대면적 공정에 적용할 수 있는 장점 때문에 차세대 전자소자로 많은 각광을 받고 있다. 하지만 이러한 많은 장점에도 불구하고 많은 전자주입, 이동도, 수명, 동작 안정성, 신뢰성, 균일성과 같은 많은 문제점이 있다. 고성능 유기다이오드를 제작하기 위한 중요한 쟁점 중 하나는 전하주입효율을 향상시키는 것이다. 본 논문에서는 다이오드의 유기물/금속 계면을 연구하여 전하효율을 향상시키고 고성능의 다이오드를 제작하는 연구를 진행하였다. 고성능의 다이오드를 제작하기 위해 전기적어닐링을 이용한 전하효율 향상 방법과 자기조립단분자막을 이용한 전하주입장벽 감소방법에 대한 연구를 진행하였다.

첫째로 이온함량이 없기 때문에 이때까지 적용되지 못했던 전기적어닐링 방법을 펜타센 다이오드에 연구하였다. 이온함량을 대신하여 고성능 다이오드 제작에 유리한 삼산화몰리브덴을 열증착하였다. 전기적어닐링 이후에 펜타센 다이오드의 문턱전압은 1.3 V 에서 0.2 V 로 감소하였고 역방향누설전류의 증가 없이 3 V 에서 순방향 전류가 0.2 mA 에서 1 mA 로 증가하였다. 삼산화몰리브덴 대신 HAT-CN, F_{16}CuPc 와 같이 깊은 최고준위분자궤도를 가지는 물질을 사용하였을 때는 전기적어닐링 효과가 나타났으나 PEDOT:PSS, m-MTDATA, CuPc 와 같은 전하주입층을 사용하였을 때는 전기적어닐링

효과가 나타나지 않았다. 전기적어닐링을 통하여 성능을 향상시킨 다이오드로 제작한 정류기는 차단주파수가 10.5 MHz 에서 85.7 MHz 로 증가하였다. 전기적어닐링이 아닌 어닐링만 소자에 가해주었을 때는 문턱전압 감소나 순방향 전류증가가 일어나지 않았고 이로부터 가해준 전압에 의한 전기장이 전기적어닐링 효과를 주는데 주요한 역할을 하는 것으로 볼 수 있다. 비행시간형이차이온질량분석기 측정과 임피던스 분석을 통해 우리는 전기적어닐링에 의해 소자가 향상되는 원인은 금/삼산화몰리브덴/펜타센 계면에 생성된 삼산화몰리브덴:펜타센 혼합층이 전하주입장벽을 효과적으로 낮춤으로써 전자주입효율을 증가시키기 때문으로 결론지었다. 특히 이러한 균일하고 얇은 삼산화몰리브덴:펜타센 혼합층의 생성은 열증착과 같은 방법으로는 만들 수 없기 때문에 전기적 어닐링은 소자성능을 향상시키는 균일하고 얇은 삼산화몰리브덴:펜타센 혼합층을 만들기 위한 최적의 방법이다. 전기적 어닐링 이후에 알루미늄 또한 펜타센 층으로 들어간 것을 확인할 수 있었다. 알루미늄은 다결정질의 펜타센 표면 위에 증착되기 때문에 펜타센의 결정경계에 뾰족하게 형성된다. 이러한 뾰족한 알루미늄들은 더 높은 전기장을 유도시키고 이 때문에 이 부분에서 알루미늄이 더 쉽게 펜타센 층으로 침투될 수 있다. 따라서 침투된 알루미늄은 알루미늄 막대와 같은 모양을 형성하며 이것이 임피던스에서 CPE 를 형성한 것으로 생각된다.

두번째로 금 및 자기조립단분자막 처리된 금 표면 위에 증착시킨 펜타센의 수직방향 구조-특성 관계를 연구하였다. 광전자분광기로부터 금, TP 처리된 금, 그리고 PFBT 처리된 금의 일함수는 각각 4.78, 4.67,

그리고 5.02 eV 로 측정되었다. PFBT 처리된 금은 양극과 활성층 사이의 전하주입장벽을 효과적으로 낮추어주기 때문에 PFBT 처리된 금 위에 만든 펜타센 다이오드는 처리되지 않은 금 위에 만든 펜타센 다이오드보다 높은 성능을 나타내며 3 V 에서 100 A/cm^2 의 전류밀도를 나타내었다. 또한 정류비는 1 V 에서 7.47×10^5, 2.8 V 에서는 1.05×10^7 으로 매우 높은 값을 얻을 수 있었다. 이 다이오드와 커패시터, 저항으로 만든 정류기는 10 V 의 전압을 인가하였을 때 3dB 주파수가 1.24 GHz 로 측정되었다. X-선 회절분석, 원자현미경, 그리고 라만 분석을 통해 금 표면 위에 증착시킨 펜타센은 누워있는 경향을 보였고, PFBT 처리된 금 표면 위에 증착시킨 펜타센은 서있는 경향을 보여주었다. 이러한 구조적 차이는 전기적 특성 또한 변화시켰다. 공간전하제한전류로 계산한 펜타센의 이동도는 금 및 PFBT 처리된 금 위에 올린 것이 각각 6.82×10^{-4}, 0.114 cm^{2}V^{-1}s^{-1} 로 측정되었다. X-선 회절분석과 수직 주사현미경 이미지로부터 금 위에 증착시킨 펜타센은 정렬적되지 않고 얽혀있는 구조를 보여주었고 PFBT 처리된 금 위에 증착시킨 펜타센은 정렬되고 빽빽한 구조를 보여주었다. 따라서 금 위에 증착시킨 펜타센은 좋지 못한 정렬구조 때문에 전하이동특성을 방해 받고 이 때문에 금 위에 증착된 펜타센은 PFBT 처리된 금 위에 증착된 펜타센보다 이동도가 낮게 나온 것으로 결론 지을 수 있다.

주요어: 유기다이오드, 유기정류기, 전기적어닐링, 자기조립단분자막, 펜타센, 전파식별, 유연성 전자소자.

학번: 2008-20815